Transformation of crystal structure and change of magnetism in spinel ferrite thin films via ion irradiation

Liu Yang

April 2021

Transformation of crystal structure and change of magnetism in spinel ferrite thin films via ion irradiation

Liu Yang
Doctoral Program in Applied Physics

Submitted to the Graduate School of
Pure and Applied Sciences
in Partial Fulfillment of the requirements
for the Degree of Doctor of Philosophy in
Science Engineering

at the
University of Tsukuba

ABSTRACT

This thesis concerned a study of ion irradiation effect on both crystal structure and magnetic properties of spinel ferrite. The saturation magnetization of $CoFe_2O_4$ and Fe_3O_4 thin films grown on MgO $(0\,0\,1)$ substrates decrease with the increase of Kr ion dose, finally the saturation magnetization of $CoFe_2O_4$ and Fe_3O_4 thin films totally disappeared when Kr ion dose reach a certain degree. The spinel structure ($Fd\bar{3}m$) of $CoFe_2O_4$ and Fe_3O_4 was found to be destroyed by the ion irradiation and transformed into another structure without loss of the epitaxial relationship with the MgO substrate. For understanding the mechanism of the structural change of spinel ferrite, we focused on Fe_3O_4 thin film as it only contains Fe and O distribution. Both total film thickness of Fe_3O_4 thin film and ion-irradiated thin film, and therefore, the composition ratio between Fe and O remained the same even after the ion irradiation process, as confirmed by both cross-section transmission electron microscopy images and Rutherford backscattering analysis. X-ray diffraction experiment revealed that the irradiated crystal becomes rocksalt structure ($Fm\bar{3}m$) with lattice constant approximately half of that for Fe_3O_4. The ion irradiation gives rise to topotactic crystal transforms to wüstite with a composition of $Fe_{0.75}O$ which does not exist as a non-equilibrium state.

Content

1. Introduction

1.1 Magnetic recording devices

For the past few years, the demand for high-density recording devices increased rapidly[1]. With the increasing of recording density, the perpendicular magnetic recording system became the predominant method in recent years. The figure 1.1 shows the perpendicular magnetic recording system. In the future, the recording density will keep increasing in the same way to satisfy the further demand. In order to realize the high recording density, the size crystalline grain of magnetic recording unit should be as small as possible, usually the size is a few nanometers. In such small size of crystalline grain, the thermal vibration effect of magnetic particles, in other words, the thermal stability becomes more and more important. To the general magnetic particles, we used to judge the thermal stability by Eq. 1-1[2].

$$\frac{K_u V}{k_B T} > 60 \qquad \text{Eq. 1-1}$$

Here, K_u is the coefficient of magnetic anisotropy, V is the volume of the magnetic particle, k_B is the Boltzmann coefficient, and T is the absolute temperature. Also, the value of 60 represents the fact of thermal stability. When the value is larger than 60, it can guarantee the thermal stability for 15 years[3,4]. As a result, if the size of particle is small, it's obviously that the coefficient of magnetic anisotropy of magnetic material is needed very high to satisfy the thermal stability.

At present, the magnetic recording material is CoCr alloy thin films[5]. However, coefficient of magnetic anisotropy of CoCr is not high enough to satisfy the requirement of the high-density recording media. For example, CoCrPt has the anisotropy about 2×10^6 erg/cm^3 [6,7]. Owing to development CoCr alloy has come to the bottleneck, it has to change to other kinds of materials. FePt[8,9] alloy is now under research, because it has the high anisotropy at about 7×10^7 erg/cm^3 [10,11]. Therefore, FePt alloy probably will become a new kind of material to be used as high-density recording media. Nevertheless, there are some problems which we have to consider, that is the price of Pt is not only very expensive but also the place of origins are mainly South Africa and Russia. The supply must be very instability. As a result, out lab choose $CoFe_2O_4$ which without Pt as the magnetic material. The advantage of $CoFe_2O_4$ is that the cost is low, Curie temperature is much higher than the room temperature, as well as high anisotropy[12,13]. It's worth to do some research about it.

Besides, new technique for recording devices is needed. The bit pattern media (BPM) ameliorates the recording media[14,15], however, the energy assist recording media[16] improves the recording head. The energy assist recording media is short for EAMR. The EAMR is the volume of one bit is reduced to increase the recording density, while the recording media with large anisotropy constant is used. As a result, the requirement of magnetic field for the magnetization reversal becomes large. Though applying some energy from the outside, compared to the prior, the requirement of magnetic field for the magnetization reversal reduces. As a candidate of the energy supplied from the outside to the recording media, Thermal energy or Microwave energy has been considered, the thermal energy or the microwave energy is the so-called heat assist magnetic recording (HAMR) or thermal assisted magnetic recording (TAMR)[17,18,19], microwave assisted magnetic recording (MAMR). The figure 1.2 is the sketch of HAMR[20]. The figure 1.3 is the profile of MAMR[20].

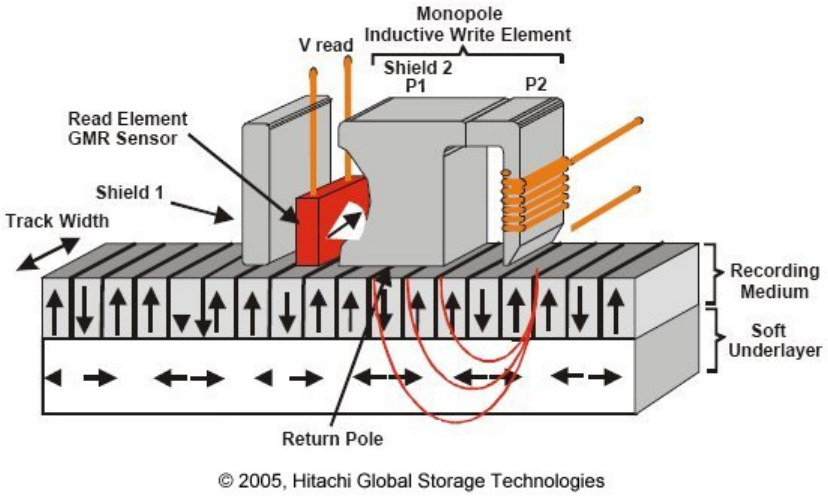

Fig. 1.1 The schematic of perpendicular magnetic system[21].

HAMR is based on the energy of laser to heat the recording media. Generally, when the temperature is below the Curie temperature, the ferromagnet will become the paramagnet. Furthermore, the magnetic anisotropy of magnetic recording material decreases, during the process of the temperature close to the Curie temperature. A small laser is used to heat the part of the magnetic recording material that is being written to. The heat changes the coercivity of the magnetic recording material for a short time, reducing or removing the super paramagnetic effect while writing takes place. This magnetic effect sets a limit on the areal density of magnetic recording. The effect of heat assist magnetic recording is to allow writing on a much smaller scale than before, greatly increasing the amount of data that can be held on a standard disk platter.

For the purpose of facilitating the writing of magnetic information, a magnetic field with high-frequency, in microwave-assisted magnetic recording, is applied to the microscopic region of recording media. With the aid of a high-frequency magnetic field, the magnetization of recording media can be reversed by a weak magnetic field. The magnetization inversion of the recording media occurred just below the oscillator is confirmed due to a combination of the developed spin torque oscillator and perpendicular recording media is used. Using the spin torque oscillation device near to the recording media at the same time that a weak magnetic field is applied to the recording media without magnetization inversion is also confirmed.

The research results show that microwave-assisted recording is a feasible technology both in principle as well as experimentally. In addition, by using microwave-assisted recording, it was confirmed through computer simulation that a recording density of 3 Tbits/inch^2 is feasible.

In this study, we paid attention to the BPM technique, as the fabricating process of BPM should use the ion irradiation technique, which nowadays is widely used in the industry, agriculture, and various scientific fields. First of all, we will make some introduction of bit pattern media.

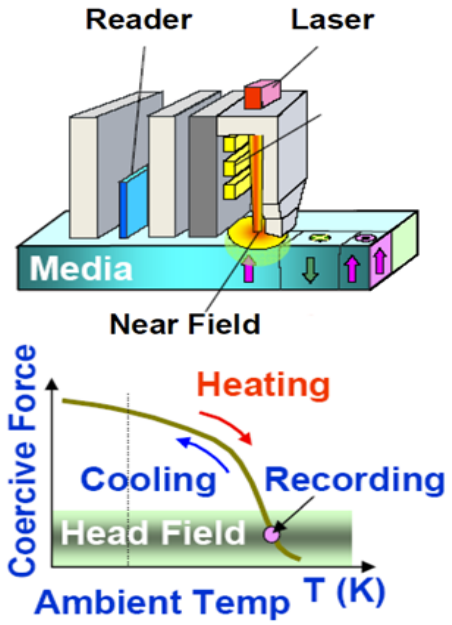

Fig 1.2 Heat assist magnetic recording[7].

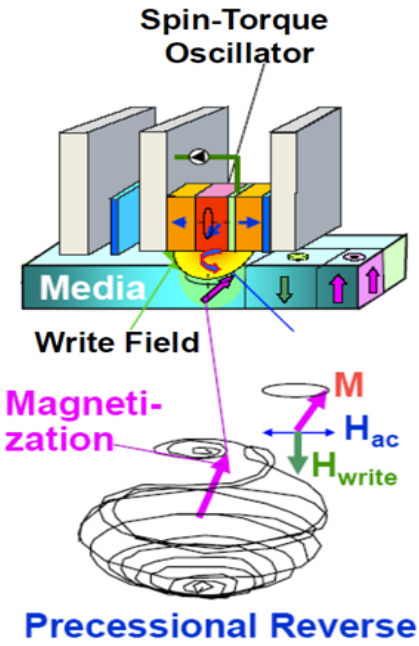

Fig 1.3 Microwave assisted magnetic recording[7].

1.2 Bit Pattern Media

It's realized that nowadays the recording media, one bit (one magnetic dot and space) which the red or the yellow part shows in figure 1.4 is made up by lots of particles. In the past, due to increasing the recording density, there are plenty of attempts have been done.

First of all, the number of the particles are attempted to reduce of 1 bit to increase the recording density. However, it cased the signal to noise radio which is short for SNR to reduce. We always need the SNR of magnetic recording material as large as possible, as the larger of the SNR, the weaker of noise radio. The reason why SNR reduced is that SNR is proportional to the number of the particles of 1 bit[22].

Then it turns to reduce the volume of the particle, however, from the thermal stability factor, if the volume (V) becomes smaller, it should have a high coefficient of anisotropy (K_u) to keep the factor is larger than 60 to prevent the thermal stability to become poor. But coercivity (H_c) is proportional to K_u, if K_u increase the H_c will increase, as a result, it's hard to write in.

According to the two kinds of attempts above to increase the recording density of recording media, it's apparent that the recording capability is decided by Media SNR, Thermal stability and Write ability at the same. The three elements have great effect on each other; there is no doubt that if we want to increase the recording density of recording media, we must look at these three elements simultaneously. Ignoring any one of them, the recording ability of recording media will become poor. This is called the magnetic recording trilemma, which describes the relationship among the three elements extraordinary iconically, showed in the figure 1.5[23]. In order to keep the balance of the triangle, the three sides of the triangle describe the contact among the three vertexes of the triangle which represent the three elements of the recording media. It is convinced that due to increase the recording capability, it's significant to deal with the connection of these three elements.

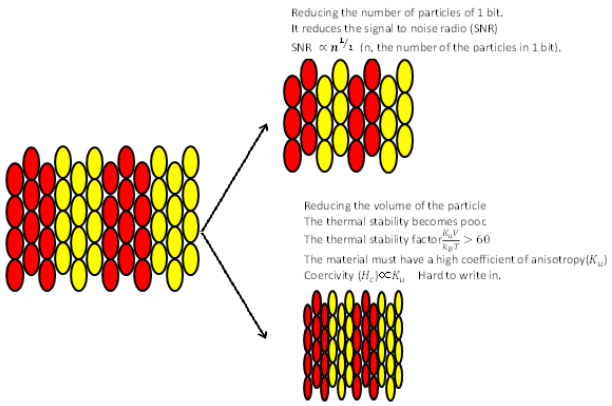

Fig 1.4 Particles in one bit.

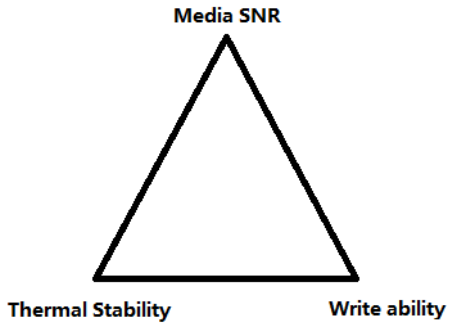

Fig. 1.5 Magnetic recording trilemma.

According to the magnetic recording trilemma, for the high density of recording media, it's significant to attempt to obtain the applicable condition to fit the magnetic recording trilemma. It turns to make kind of media which 1 bit is made up by 1 particle. And it can solve the two problems ahead if the volume is enough. At the same time, recording density increases, also SNR increase because the particles are in order. And this kind of recording media is called bit pattern media (BPM). One of features of BPM is that the size of magnetic layer is reduced to one bit. As high-density magnetic recording media for hard disk drives, BPM is being followed. If the recording density exceeding 2.5 Tbits/in^2 for BPM, the size of the magnetic dot must reduce to less than 10 nm, which is a huge challenge for cutting-edge semiconductor processing technology to fabricate BPM in this size. One of solution is using an etching mask made of a self-assembled, however, for complicated structures such as servo pattern, it is too hard to form an ordered dot array into this kind of structure which is necessary for read and write operations.

The method to fabricate the BPM is that

(1) Fabricating the thin films on the pattern substrate.

(2) Etching the thin films to make pattern.

(3) Ion irradiation to thin films.

Specifically, concerning the method (1), depends on the nano imprint lithography technology, on the surface of aluminum, nanometer-sized hollow pattern is formatted. This is a way to fabricate the bit pattern media on the order of nano hold disk. Concerning the method (2), in this method, the nano imprint technology is used to prepare the guide groove which containing the servo pattern for sequence controlling, and then filling the self-assembly material. Along the grooves with the heat treatment, the dot pattern is arranged. This pattern is worked as a mask, with the effect of ion beam, the magnetic materials is eliminated, with this method to fabricate the bit pattern media. Ion irradiation technique has been adapted to metallic substances, Co/Pd multilayers and CoCrPt where irradiation with N_2 ions at 1×10^{16} ions/cm^2 was effective[24]. Kr ions are also effective in controlling magnetism of metallic CoPt3 and MnGe[25,26]. Now, Toshiba Corporation is using this method to do research and development[27]. Concerning the method (3), the ion irradiation is used on a mask

with pattern, with this method the recording media become to magnetic parts (without ion irradiation) and nonmagnetic parts (with ion irradiation). The method is reported by C. T. Rettner[28] and D. Ravelosona[29]. The figure 1.6 shows a BPM fabrication process with ion irradiation technique. The figure 1.7 denotes the profile of bit pattern media[7].

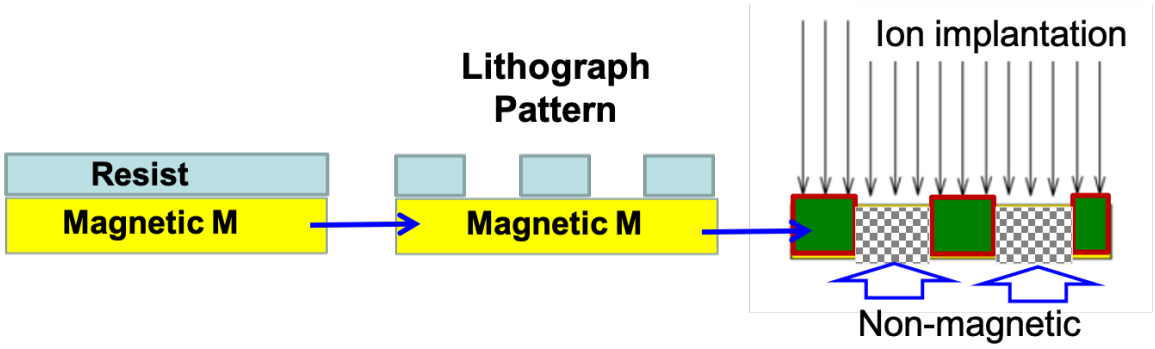

Fig. 1.6 BPM fabrication process with ion irradiation technique.

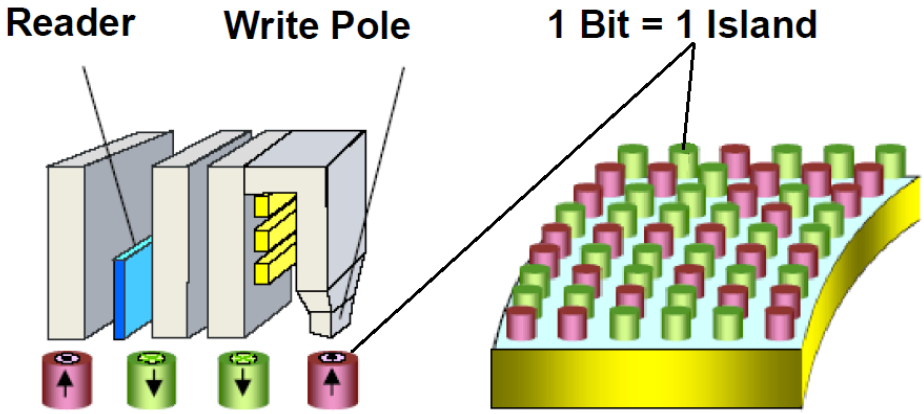

Fig 1.7 Profile of bit pattern media[20].

1.3 Ion Irradiation

Ion irradiation is a unique materials engineering process for locally modifying or forming a nonequilibrium structure in which accelerated ions are impacted into a solid. Ion irradiation can also be called as Ion implantation. Over past decades, ion irradiation has been investigated on various fields, great efforts have been expended in studying the effects of ion irradiation of materials[30,31,32,33,34,35,36]. For human beings, nowadays understanding and predicting radiation damage is significant, because a world-wide demand for nuclear energy as the increasing energy continues[37]. Ion irradiation experiment can enhance the capability of both current and next-generation nuclear reactors. Ion irradiation also can cause chemical reactions to modify a material[38,39,40]. In general, some changes induced by these reactions, such as chemical ordering[11,41], interface of multilayers[38] and structure[41,42] and consequently affects their physical properties[43,44,45,46].

It is known that at the microscopic scale, magnetic properties are sensitive to the material environment. In this sense, ion irradiation is a powerful tool for modifying the magnetic properties of the materials. In fact, many reports show magnetization decrease associated with crystal structure change as a result of ion irradiation[41]. The magnetic properties of materials can also be altered, either from ferromagnetic to nonmagnetic[24,47,48] or from nonmagnetic to ferromagnetic[49]. Metallic magnetic materials, MnGa and MnAl 15 nm thin films with large perpendicular anisotropy and $L1_0$ ordered structure were investigated by D. Oshima e*t. al*[41]. They reported the magnetization of MnGa thin film and MnAl thin film decreased to 0 after ion irradiation. which is confirmed by the hysteresis loops of MnGa thin film before and after ion irradiation given in the figure 1.7. The structure change from $L1_0$-ordered structure to A1-disordered structure was reported through XRD results, which is shown in the figure 1.8.

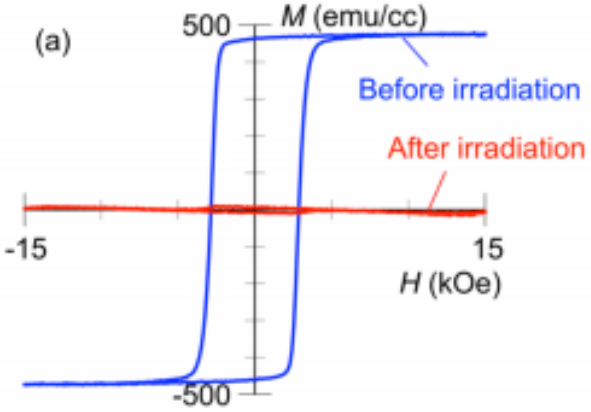

Fig. 1.7 The hysteresis loops of MnGa thin film before and after ion irradiation.

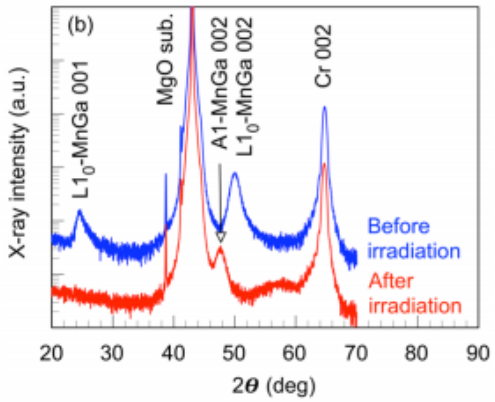

Fig. 1.8 XRD results of MnGa thin film and ion-irradiated MnGa thin film.

According to the phase diagram of Mn-Ga, which is indicated in the figure 1.9, $L1_0$-ordered structure is belong to γ_3, on the other hand, A1-disordered structure is belong to γ_2. The structural change of MnGa thin film via ion irradiation is from low temperature phase to high temperature phase, with the same composition.

Ion irradiation has also been investigated for spinel materials such as $MgAl_2O_4$ $MgGa_2O_4$ and $MgIn_2O_4$ [42,] polycrystalline spinel materials were reported that transform to rocksalt structure via ion irradiation, the XRD results are shown in the figure 1.10. The reflections of spinel structure disappeared after ion irradiation, instead, the reflections belong to rocksalt structure appeared. This conclusion gives us some revelation. The effect of ion irradiation has been investigated for metal materials and polycrystalline spinel materials. The magnetic disappeared with the structural change from ordered to disorder and structure totally change to another type. However, there is no study for the effect of ion irradiation for single crystal spinel ferrite oxide.

In pervious study, we have nitrogen ion irradiation have been done on Fe_3O_4 epitaxial grown thin film[50]. The magnetization decreased and finally disappeared with the increasing ion dose was understood. The figure 1.11 reveals a set of hysteresis loops of Fe_3O_4 thin film and after several dose of ion irradiation. The effect of

nitrogen ion irradiation on magnetization of Fe_3O_4 thin film was investigated, however, details of structure change after ion irradiation has not been understood. Such as, thickness and composition of ion-irradiated thin film.

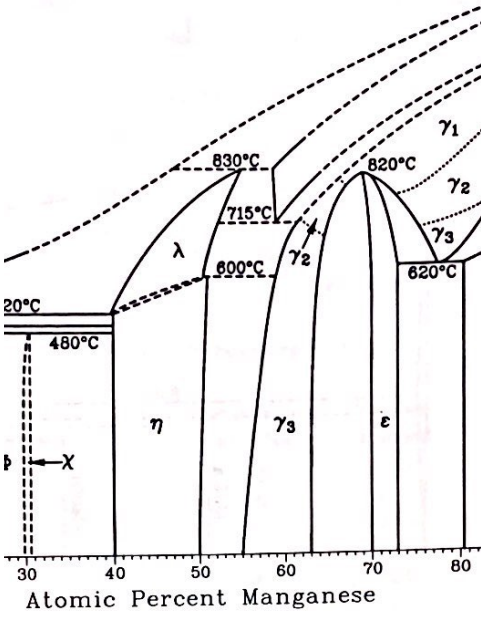

Fig. 1.9 The phase diagram of Mn-Ga[51].

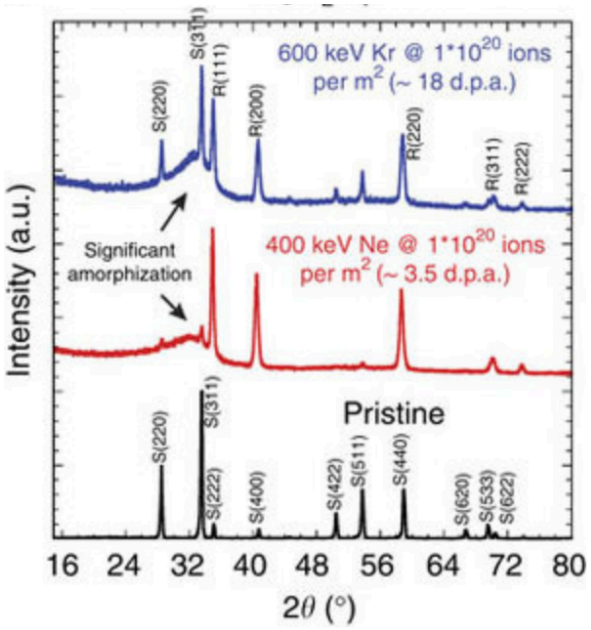

Fig. 1.10 The XRD results of polycrystalline spinel material before and after ion irradiation [42].

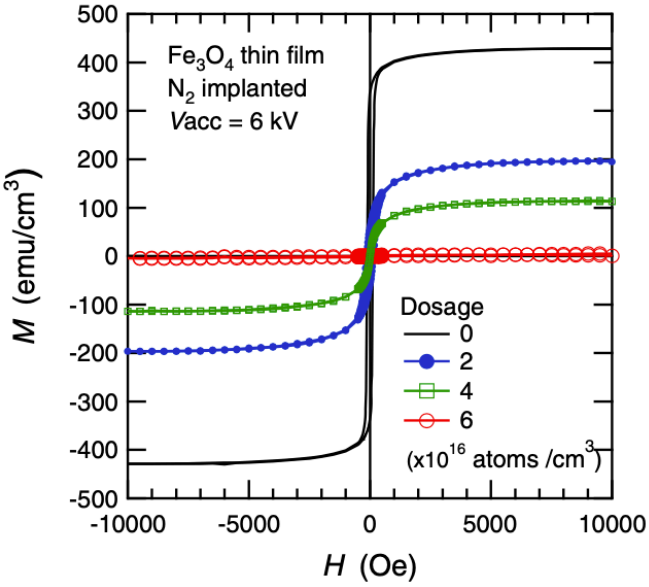

Fig. 1.11 hysteresis loops of Fe_3O_4 thin film and after 2×10^{16} ions/cm^2, 4×10^{16} ions/cm^2 and 6×10^{16} ions/cm^2 N_2 ion irradiation, respectively.

1.4 Spinel Ferrite

1.4.1 The structure and magnetism of Spinel Ferrite

Ion irradiation as a powerful tool to modify magnetism of spinel ferrite oxide, it's significant to understand mechanism of it. In this study, we paid attention to spinel ferrite oxide, $CoFe_2O_4$ and Fe_3O_4. As the typical spinel oxide, we consider it can give us a comprehensive understand for the effect of ion irradiation on the spinel ferrite oxide.

$CoFe_2O_4$ is one of the spinel ferrite materials. Spinel ferrites are spinel crystal structure, and represented by the chemical formula

$$M^{2+}Fe_2^{3+}O_4 \text{ or } MO \cdot Fe_2O_3,$$

Here, M represent the metals. The figure 1.11 indicates a quarter of unit cell of the spinel crystal structure[52].

In the spinel structure, each unit cell occupies 32 oxygen ions, 8 metal cations occupy in tetrahedral site (A site) and 16 metal cations occupy in octahedral site (B site). The 32 oxygen constitute face-centered cubic lattice, in A site 4 oxygen ions occupy the vertex of the tetrahedron, in B site 6 oxygen ions occupy the vertex of the octahedron. When the metal ions M^{2+} occupy the A site, this type is called Normal spinel ferrite. When the metal ions M^{2+} occupy the B site, this type is called Inverse spinel ferrite. Depends on the position, the chemical formula contains A site and B site that write with the form (A)[B], like below:

Normal spinel ferrite: $(M^{2+})[Fe_2{}^{3+}]O_4$

Inverse spinel ferrite: $(Fe^{3+})[Fe^{3+}M^{2+}]O_4$

In the form the M^{2+} represents kinds of metal such as Fe, Co, Ni, Cu, Cd, Zn, Mn, as well as the compound of these metals. When Cd or Zn constitutes the spinel ferrite, it's the normal spinel ferrite. On the other hand, the others are the inverse spinel ferrite. The magnetic moment of spinel ferrite n_B make up by the magnetic moment of $Fe_2{}^{3+}$ and M^{2+}, μ_B、$m\mu_B$ respectively. There is a factor that

$n_B = [m(1-\delta)+5(1+\delta)]_B \text{ site}\mu_B - [m\delta+5(1-\delta)]_A \text{ site}\mu_B = [m(1-2\delta)+10\delta]\mu_B$

can get the magnetic moment of spinel ferrite. In this factor, when $\delta = 1$, it's the normal spinel ferrite. When $\delta = 0$, it's the inverse spinel ferrite[52].

The table 1.1 gives the physical properties of primary spinel ferrite[53].

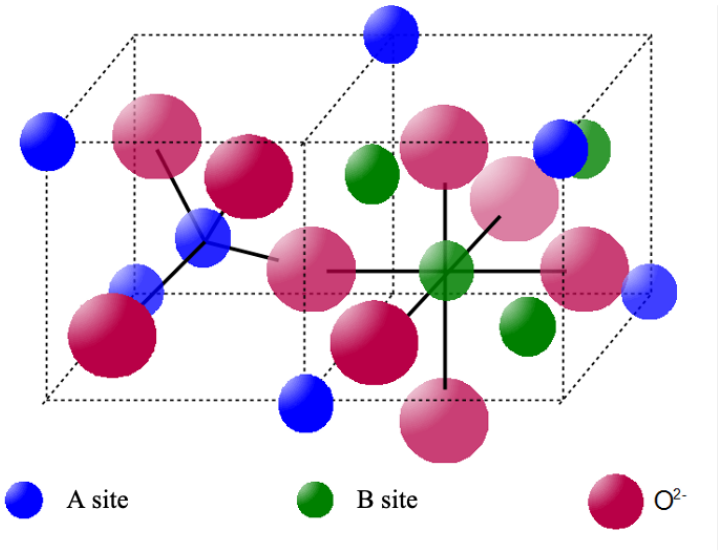

Fig 1.11 a quarter of unit cell of the spinel crystal structure[52].

The table 1.1 Physical properties of primary spinel ferrite[53].

	a (Å)	ρ (Ωcm)	M_s (emu/cm^3)	T_c (°C)	K_1 (Merg/cm^3)
$ZnFe_2O_4$	8.44	10^2	AF	$T_N = 9.5$[K]	
$MnFe_2O_4$	8.51	10^4	400	300	-0.040
$FeFe_2O_4$	8.39	4×10^{-3}	480	585	-0.130
ɤ-Fe_2O_3	8.34		415	575	-0.046
$CoFe_2O_4$	8.38	10^7	420	520	$+2.000$
$NiFe_2O_4$	8.34	$10^3 - 10^4$	270	585	-0.069
$CuFe_2O_4$ Quenching	8.37	10^5		455	-0.063
$CuFe_2O_4$ Slow cooling	8.22		135	30	-0.060
$MgFe_2O_4$	8.36	10^7	120	440	-0.040

1.4.2 Fe_3O_4 Magnetite

The Fe_3O_4 is the inverse spinel ferrite. A site is occupied with Fe^{3+} ions only, and B site is occupied with 8 Fe^{2+} ions and 8 Fe^{3+} ions. And below is the chemical formula.

$$(Fe^{3+})[Fe^{3+}, Fe^{2+}]O_4$$

It's clearly that the B site in magnetite is made up by Fe^{3+} and Fe^{2+} ions, in Crystallographic, the Fe^{3+} and Fe^{2+} ions are in the presence of equal valence. The change of position of equal valence ions doesn't

change the energy in the Crystallographic. If Fe^{3+} and Fe^{2+} ions would interchange their positions, the electrons would also move their positions. This kind of electron move is called Hopping conduction - only the electron moves, but the nucleus does not move. For this reason, the resistivity of magnetite is weaker than for other spinel ferrites. Fe_3O_4 is ferrimagnetic with a Curie temperature of 858 K. There is a phase transition at 120K, the effect is called Verwey transition. The table 1.2 below shows the properties of magnetite[52,53].

The table 1.2 The properties of magnetite[52,53].

Crystal structure	Inverse spinel structure
Lattice constant	8.39 Å
Molar mass	231.533 g/mol
Saturation magnetization	477 emu/cm^3
Anisotropy constant	-1.3×10^5 erg/cm^3
Curie temperature	858 K
Resistance	4×10^{-3} Ω·cm

1.4.3 $CoFe_2O_4$ Cobalt Ferrite

The $CoFe_2O_4$ is the inverse spinel ferrite. A site is occupied with Fe^{3+} ions only, and B site is occupied with 8 Fe^{2+} ions and 8 Co^{2+} ions. And below is the chemical formula.

$$(Fe^{3+})[Fe^{3+}, Co^{2+}]O_4$$

The theoretical value of magnetic moment of cobalt ferrite is $3\mu_B$, the measured value in bulk is $3.9\mu_B$. It's considered that orbital magnetic moment is not completely disappeared. Not only the coercivity of cobalt ferrite is strong, but also the anisotropy constant is large. As a consequence, cobalt ferrite is suitable for fabricating the magnetic recording media.

There are different kinds of fabricating method of $CoFe_2O_4$ thin films. The Molecular Beam Epitaxy, short for MBE[54,55,56]. Pulsed-Laser Deposition, short for PLD[57,58]. And the method of sputtering[59].

The table 1.3 below shows the properties of cobalt ferrite in bulk[52,53].

The table 1.3 The properties of cobalt ferrite in bulk[52,53]

Crystal structure	Inverse spinel structure
Lattice constant	8.38 Å
Molar mass	234.6 g/mol
Saturation magnetization	421 emu/cm^3
Anisotropy constant	2.0×10^{16} erg/cm^3
Curie temperature	793 K
Resistance	1×10^{7} Ω·cm

1.5 The purpose of this study

In this study, we attempt to use technology of ion irradiation to control the magnetization of spinel ferrite materials, $CoFe_2O_4$ and Fe_3O_4 epitaxial thin films grown on MgO (0 0 1) substrates. In order to understand the reason why the magnetization disappeared after ion irradiation, the structure analysis was carried out. For further study of mechanism of effect of ion irradiation, a typical inverse spinel ferromagnetic oxide Fe_3O_4 is focused, as it only contains Fe and O distribution and could help us much clearly understand the structural change during Kr ion irradiation process. This study can help us understand the effect of ion irradiation influenced on spinel ferrite thin film much better.

2. Sample preparation and characterization techniques

This chapter reviews the experimental process and analysis methods of this study. First, we introduce the basics of the fabricating techniques and apparatus used in this study for the sample preparation. Then we illustrate the condition of fabricating sample in detail, i.e. the recipe and preparation of the thin film. The ion irradiation process is described in following include the experimental device and irradiation condition. For the characterizations, we will briefly explain the principles of the main techniques employed in this study. Vibrating sample magnetometer (VSM) were used to measure the magnetization of thin film. Scanning Transmission Electron Microscope (STEM) were carried out to confirm single crystalline and compare the thickness before and after ion irradiation. Structural analysis was realized through Electron diffraction (ED) and X-ray diffraction (XRD) study. Fe component were confirmed by Rutherford Backscattering analysis (RBS), and Mössbauer spectroscopy gave more details for Fe distribution.

2.1 Sample preparation

2.1.1 Reactive Sputtering

With the method of sputtering, the reactive sputtering in an RF planar magnetron sputtering system (MPS-6000-HC4/6, ULVAC) was used for fabricating the Fe_3O_4 and $CoFe_2O_4$ thin film in this study.

Sputtering is a process whereby atoms are ejected from a solid target material due to bombardment of the target by energetic particles. In other words, sputtering is a technique which used to deposit thin films of a material onto a substrate. During the process of sputtering, first of all it's the creating of gaseous plasma and then, from this plasma, there are plenty of the accelerating the ions, the accelerating ions go into some source material target, the source material is eroded by the arriving ions via energy transfer and is ejected in the form of neutral particles either or individual atoms, clusters of atoms or molecules. Specifically, to the facility of our lab, Argon inert gases are introduced into the vacuum chamber, the cathode is applied on the target, while the anode is applied on the substrate, so that Glow Discharge occurs. The atoms of Argon inert gases become to ions, and then the accelerated ions strike to the target and the material of target is ejected and fabricate the thin film on the substrate. The figure 2.1 indicates the simple process of sputtering [].

Benefits of sputtering[60]:

(1) Any kinds of substance can be used for sputtering, especially the element or chemical compound with high-melting-point and low vapor pressure.

(2) The adhesive property between the thin film and substrate is very well.

(3) The density of thin film is high.

(4) It's easy to control.

(5) If the reactive gas, such as O_2 and N_2, is introduced, it is simple to fabricate the chemical compound thin films[61,62].

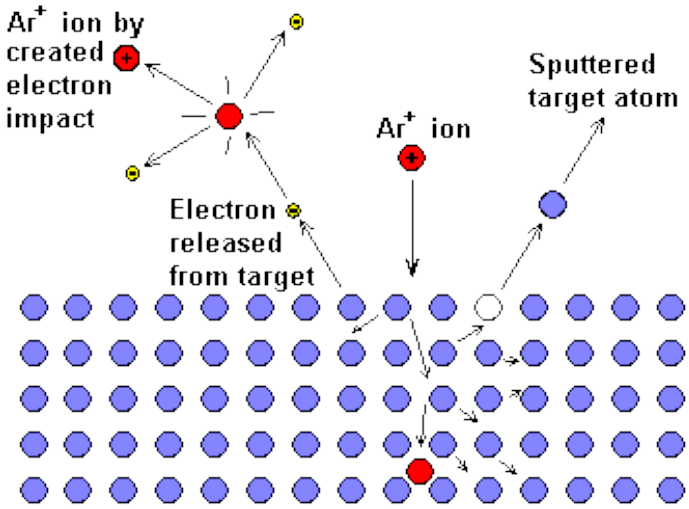

Fig. 2.1 The simple process of sputtering

Depends on the different kinds of power supplies, the sputtering system has variety types. The most common type of sputtering system is that the DC power which the direct voltage is applied and RF power which the high frequency power is applied. According to the type of power of sputtering, obviously, the discharge property should be different. As a result, property of thin films, size of substrate, description of target and the velocity of fabrication is changed while the power is changed. When the DC power is used, only the metal can be fabricated. Because of other kinds of insulated target can't discharge with DC power. When the RF power is used, it is self-evident that metal can discharge with RF power, oxide, metallic oxide and nitride can discharge too. In this study, I use the method of RF sputtering.

The method of magnetron sputtering is that, on the reverse side of the target a permanent magnet is arranged, the magnetic field is in accordance with the electrical field which perpendicular to the target. During the ions collide with the target, the secondary electron is produced which is locked in the vicinity of target. Due to the more efficient secondary electron cyclotron motion, not only promote the inert gases ionization, but also make the sputtering more efficient. Our lab's sputtering system is according to this method. The Figure 2.2 shows the profile of the reactive sputtering in an RF planar magnetron sputtering system and Figure gives the actual picture of sputtering system which our lab is used.

The sputtering system is made up by sputtering chamber, load-lock chamber, exhaust and control device. The exhaust device is turbo molecular pump (TMP) and rotary pump (RP), used for sputtering chamber (main chamber) and load-lock chamber respectively. Because of the valve, it is possible to control the exhaust independently. In the sputtering chamber, there are substrate stage, substrate heating device, 5 different targets, kinds of shutters, baratron vacuum gauge, ionization vacuum gauge, pirani vacuum gauge, quadrupole mass spectrometer and reflection high energy electron diffraction (RHEED). The control device is used to control the introducing gases, controlling the valve, changing the substrate position, controlling the power and adjusting the flow of the gases.

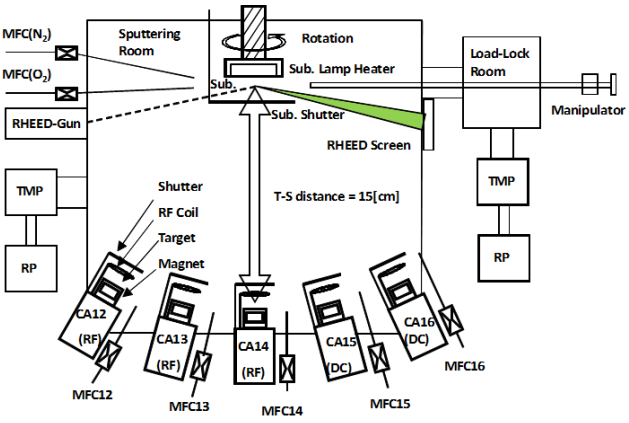

Fig. 2.2 Profile of the reactive sputtering in an RF planar magnetron sputtering system.

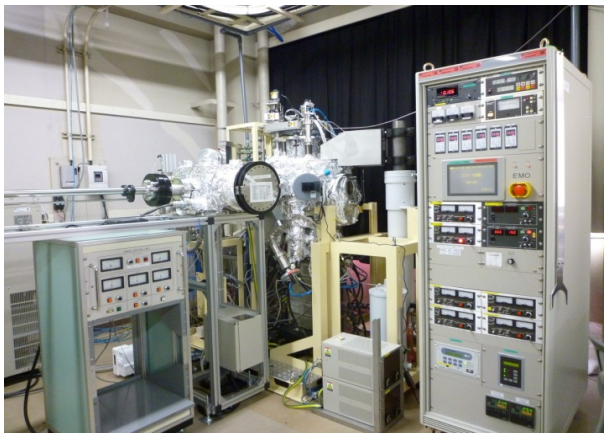

Fig 2.3 Sputtering system.

2.1.2 Fabrication process

In this part, the specific process of fabrication will be introduced.

(1) In this study, cleavage MgO (0 0 1) substrate was prepared as flat as possible.

(2) Cleavage side was upward placed in substrate holder, then inserted into the load-lock chamber and after vacuum the load-lock chamber, the substrate imported into sputtering chamber.

(3) Substrate temperature for $CoFe_2O_4$ was $600℃$ and for Fe_3O_4 was $300℃$.

(4) Confirm RHEED image for MgO (0 0 1) substrate.

(5) Ar gas was introduced into sputtering chamber at $30\ sccm$ for both $CoFe_2O_4$ and Fe_3O_4[63], and plasma was generated by RF power.

(6) For fabricating $CoFe_2O_4$ thin film, CoFe (1:3 atm ratio) alloy target, ^{57}Fe target and Co target two targets sputtered at the same time were used. For fabricating Fe_3O_4 thin film, ^{57}Fe target were used. We custom-made a thin annular tablet with a thickness of $1\ mm$ out of 25% enriched ^{57}Fe and placed it over the erosion region of a natural Fe sputter target for Mössbauer study.

(7) For cleaning the surface of target, pre-sputtering was continued for $5\ min$.

(8) O2 was introduced at $6\ sccm$ for $CoFe_2O_4$ and $1\ sccm$ for Fe_3O_4. Then open the shutter on target side and hold this state for another $5\ min$ pre-sputtering.

(9) Open the shutter on substrate side while rotating the substrate at about $10\ rpm$.

(10) After finished the sputter process, RHEED was carried to confirm.

(11) Move the sample to load-lock chamber and increase the chamber pressure to atmospheric pressure by introducing nitrogen gas before.

2.2 Ion irradiation process

As an effect method to modify the properties of material, ion implantation has been investigated on varieties of materials for decades. Physical, chemical and electrical properties of materials can be changed after ion beams effect on materials after acceleration, ion beams go into matters and collide to atoms in matters. After

ion implantation, there are 4 possible results between ion beams and atoms in matter, which are interstitial, scatter, vacancy and replacement by ion beam. The figure 2.4 shows the mechanism of 4 possible results.

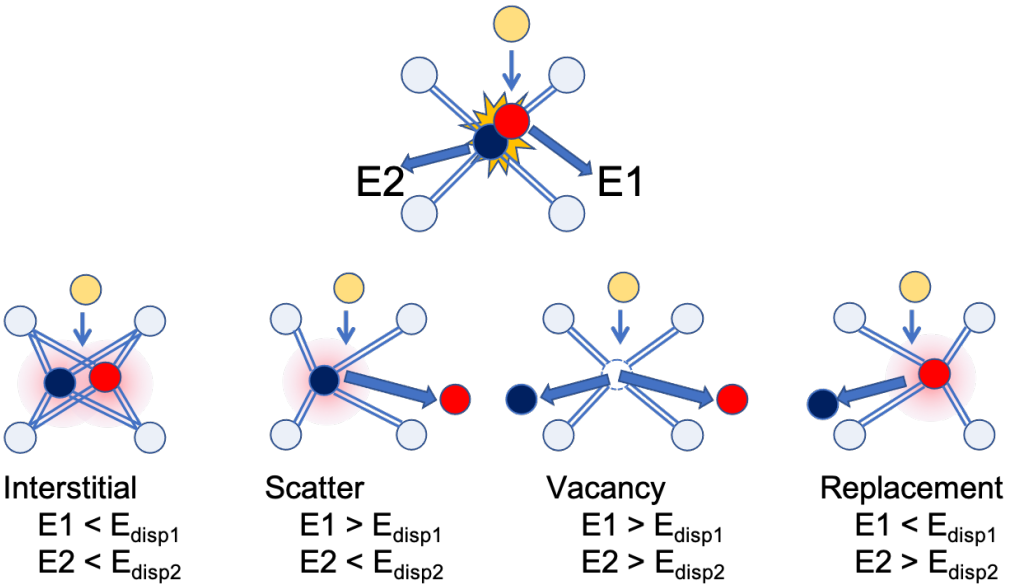

Fig. 2.4 The schematic of 4 possible results after ion irradiation.

In this study, the thin films samples are needed to test for the effect of ion implantation. Therefore, the carbon protect layer is necessary to prevent a decrease in thickness due to the sputtering by ion beam irradiation. The SC-701CT QUICK CARBON COATER which is manufactured by SANYU ELECTRON was used. After the sample was fabricated, samples were covered with carbon layer about 15 nm before the ion irradiation. The QUICK CARBON COATER is using the adoption of flashing evaporation system to coat the carbon on the sample. A pair of electrodes is set on the cartridge holder inside of the chamber, both electrodes link to the carbon stick respectively. The thin films samples are set on the just below the joint of two carbon sticks. The facility is link to rotary pump (100 L/min), in order to remove the air from the inside of chamber to make sure the coated carbon layer is pure. The degree of vacuum is 4 Pa. Coating Times of the facility is from 1 time to 19 times, both auto mode and manual mode, the coating time is 0.3 sec/one time, each time of coating the thickness of 3 nm carbon will be coated on the thin film samples. The deposition power is 12V / Max. 70A. The figure 2.5 is the profile of facility. A pair of carbon sticks is set inside of the chamber, one of them is polished to an inclined smooth surface and touch the edge of the other carbon stick. The thin films samples are set on the just below the joint of two carbon sticks.

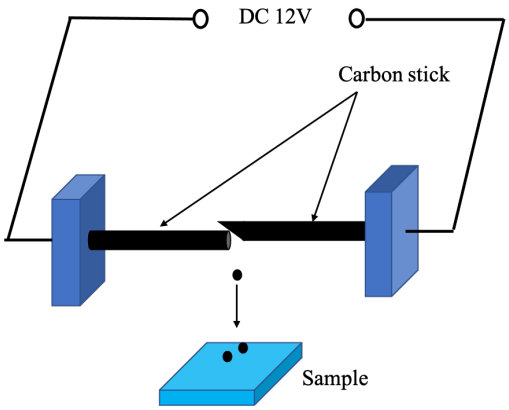

Fig. 2.5 The profile of carbon coating facility.

After the carbon protect layer was coated on the thin film sample, ion irradiation was performed at Nagoya University with an ion implantation system (Nissin electric, NH-20SR-WHM). A schematic diagram of the ion implantation system is shown in the figure 2.6, which consists of an ion source, mass spectrometry magnet, beam accelerator, and target chamber. The gas introduced into the ion source is ionized by thermionic electrons emitted from the filament to generate ions. The various generated ions are extracted by the extraction voltage, however only the target ion is extracted by the mass spectrometer. The extracted ion beams are accelerated to the desired energy by the accelerator, it is converged to focus on the target with the Q lens electrode and the V, H (vertical, horizontal) sweep electrodes are scanned to make sure that ions injected onto the target uniformly. Here, the neutral beam is removed by deflecting the ion beam by $7°$ with the H sweep electrode. The incident angle of ions is determined by the sample holder and is usually $7°$, however in some cases, the ions are incident perpendicularly to the film surface (incident angle $0°$) by changing the sample holder[64].

In this study, Kr gas was used and irradiated with Kr^+ ions. The pressure of the ion source during gas introduction was about $2 \times 10^{-5}\ Torr$, and the acceleration voltage was 30 keV with dose of Kr^+ ions from $1 \times 10^{14}\ \text{ions/cm}^2$ to $1 \times 10^{16}\ \text{ions/cm}^2$.

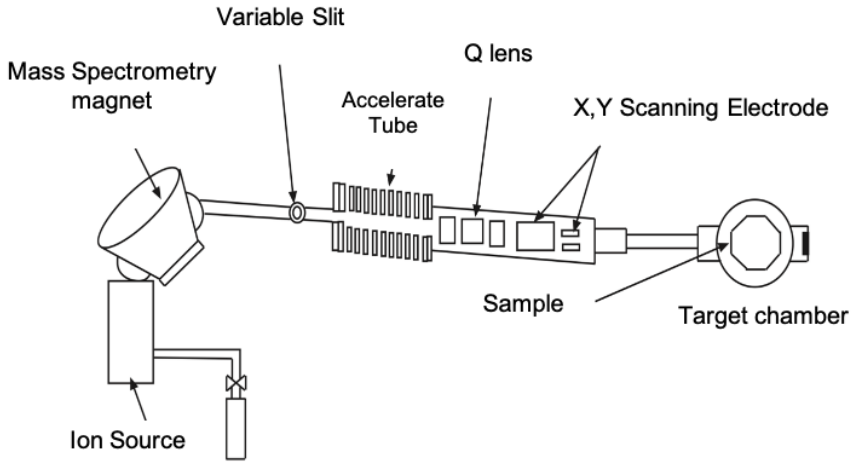

Fig. 2.6 The schematic diagram of ion implantation system[64].

Ion irradiation is a materials engineering process by which ions of a material are accelerated in an electrical field and impacted into a solid. Using this technique, one can change a magnetic state of materials from ferromagnetic to nonmagnetic, which may render the fill-back process in other lithography techniques unnecessary. In previous study of my lab, we already tested the influence of ion irradiation to a typical spinel ferromagnetic oxide Fe_3O_4 by N_2 ions and Kr ions. The result indicated that the magnetization of spinel ferromagnetic oxide can be controlled by the ion implantation[47]. Also the Kr ion is more effective than N_2 ions to change the magnetization of Fe_3O_4 thin films[47,50] as magnetization of Fe_3O_4 thin films disappeared with 4 x 10^{15} ions/cm^2 of Kr ion irradiation. It's more effective than N_2 ion which needs the dosage about 6 x 10^{16} ions/cm^2. Hence, in this study, the Kr ion was chosen to do the ion implantation. The table 2-1 indicates the specific condition of ion irradiation.

Table 2.1 The specific condition of ion irradiation.

Target	$CoFe_2O_4$ and Fe_3O_4 thin film
Carbon protect layer	15nm
Accelerate voltage	30kV
Source	Krypton
Dosage	1×10^{14} ions/cm^2~ 1×10^{16} ions/cm^2

2.3 Characterization

In this section, we will briefly explain the basic principles of the main techniques used.

2.3.1 Reflect high energy electron diffraction (RHEED)

Reflect high energy electron diffraction (RHEED) is widely used for observing the substrate or the surface of a thin film in a deposition process[65]. A RHEED system requires an electron source (gun), detector, display screen and a sample with a clean surface. The figure 2.7 shows the basic set-up for a RHEED device, with the sample viewed edge-on. The electron gun generates a beam of electrons which strike the sample at a very small angle (2-6 degree) relative to the sample surface. Incident electrons diffract from atoms at the surface of the sample, the reflected and diffracted beams are observed on a phosphor screen with a camera. The electron beam energy is 10 keV to 30 keV, it is high enough to avoid the effect of electric field and magnetic field. When the acceleration voltage becomes to 20 kV, the wavelength of electron beam is smaller than 0.0087 nm, the surface state is reflected at atomic unit.

The diffraction pattern is expressed by the reciprocal lattice space, the crystal structure can be analyzed from that pattern, the information of the flatness of the surface can be observed by the shape of the diffraction spots. When the thin film by epitaxial growth is single crystal and the lattice orientation on the surface is aligned, the pattern of RHEED is changed. If the surface is flat, the streak pattern

appears. If the surface is rough, in order to produce the diffraction in the perpendicular direction, dot pattern appears. On the other hand, In the case of polycrystalline, the image of RHEED is the pattern of ring. If in amorphous, the intensity of the diffracted beam is extremely weak, at that time, the pattern doesn't appear. In this study, the sputtering method was used to fabricate the thin film, during the sputtering; the pressure in the chamber is small, so that the image of RHEED was observed before and after fabricating the thin film.

In the layer growth system, it's possible to see the intensity of the vibration of specular spot and the diffraction spot. In the RHEED vibration, if the atomic level on the surface is flat, the intensity of reflection electron beam will become strong. In the opposite site, if the atomic level on the surface is roughness, the intensity of reflection electron beam will become weak. The figure 2.8 provides the principle of RHEED vibration[66].

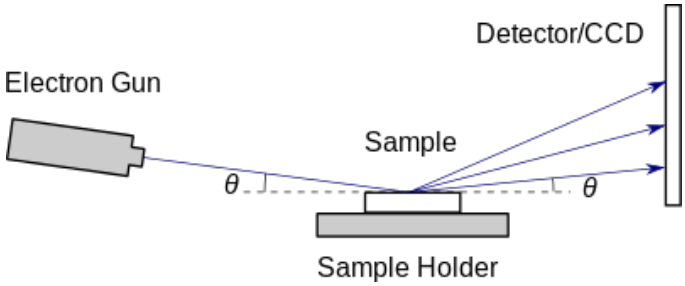

Fig. 2.7 The basic set-up for a RHEED device

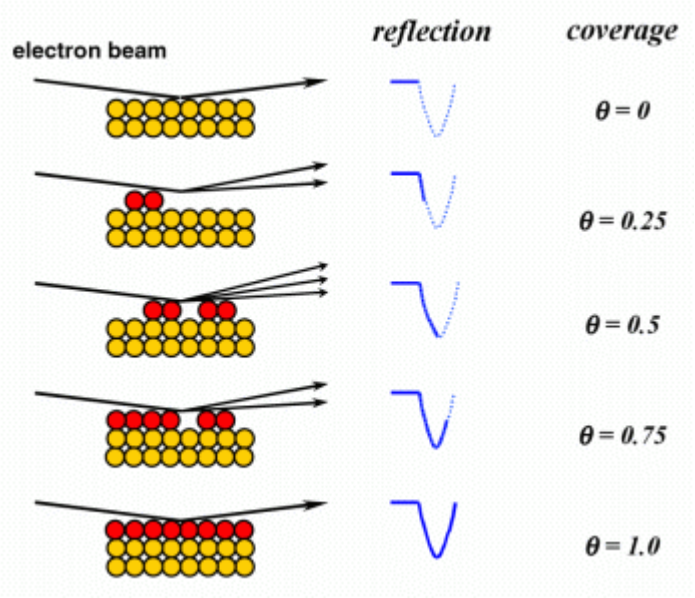

Fig. 2.8 The principle of RHEED vibration.

2.3.2 Vibrating sample magnetometry (VSM)

In this study, magnetic measurements were performed using either a vibrating sample magnetometer (VSM) or a superconducting quantum interference device (SQUID) VSM.

Faraday's law of induction states that a changing magnetic field will produce an electric field. This electric field can be measured to give us information about the changing magnetic field. Many magnetometers including the VSM operates based on this principle.

The VSM a device which a sample placed in the center of the pickup coil an external uniform magnetic field to vibrate at a constant frequency and amplitude. This causes the flux through the pickup coil to vary accordingly. Maxwell-Faraday's law of induction states that the change of magnetic flux induces a voltage. This induced voltage is proportional to the sample's magnetic moment and does not depend on the strength of the applied magnetic field. In a normal VSM, the magnetic moment of the sample is extracted directly from the voltage induced in the pickup coils. The figure 2.9 shows the schematic of a VSM system. In VSM system, a magnetized sample is attached to a rod and vibrated at a constant frequency in a DC magnetic field. The pickup coils are attached to both ends of the magnet that applies a magnetic field. By changing the magnetic flux passing through the coil, the induced electromotive force of alternating current can be obtained, which is a signal proportional to the magnetic moment of the sample. With the Equation 2.1, it's possible to measure the magnetization characteristics of a sample by detecting the electromotive force induced in the detection coil placed near the sample using a lock-in amplifier.

$$V_{\text{coil}} = 2\pi f \cdot CmA \cdot \sin(2\pi f \cdot t) \qquad \text{Eq. 2.1}$$

Here, V_{coil} is the induced electromotive force generated in the coil, f is the frequency, C is the constant, m is the magnetization, A is the amplitude, and t is the time. From this relationship, the magnetization m can be obtained by measuring V_{coil}.

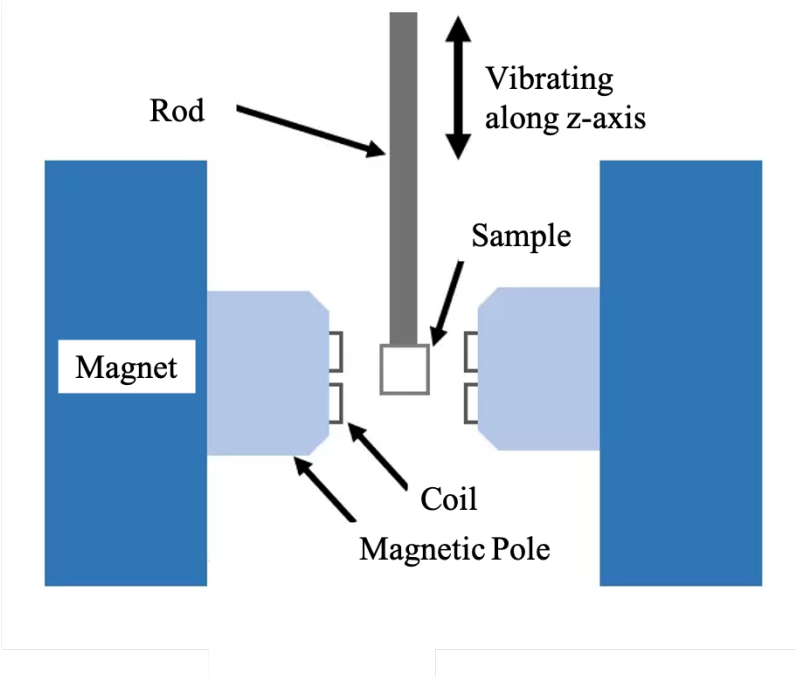

Fig. 2.9 The schematic of VSM system.

In the SQUID-VSM, the pickup coils are connected to a SQUID element that works like a very sensitive current-to-voltage converter and allows measuring indirectly weak magnetic field (signals).

DC-SQUID has two Josephson junctions in the superconducting ring as shown in the figure 2.10. The Josephson junction is a structure having a junction in which a thin normal conductor or insulator is sandwiched between superconductors. A current I exceeding the critical current is passed through this. Then, a superconducting current without a voltage drop and a normal conducting current with a voltage drop flow. The superconducting current flowing from the AC side to the BD side has a phase difference of B-A and D-C, respectively, and is expressed in the form of

$$\mathrm{I} = \mathrm{I}'\sin(\mathrm{B}-\mathrm{A}) \text{ and } \mathrm{I}'\sin(\mathrm{D}-\mathrm{C}) \qquad \text{E.q. 2.2}$$

Therefore, the maximum value of superconducting current is

$$I_{max} = \mathrm{I}'\{\sin(\mathrm{B}-\mathrm{A}) + \sin(\mathrm{D}-\mathrm{C})\}$$
$$= 2\mathrm{I}'\sin\frac{(\mathrm{B}+\mathrm{D})-(\mathrm{A}+\mathrm{C})}{2}\cos\frac{(\mathrm{B}-\mathrm{D})+(\mathrm{A}-\mathrm{C})}{2}$$

E.q. 2.3

Here, the phase difference between B-D and C-A is

$$\mathrm{B}-\mathrm{D} = \frac{2\pi}{\varphi_0}\int_{D\to B} A\,dl$$
$$\mathrm{C}-\mathrm{A} = \frac{2\pi}{\varphi_0}\int_{A\to C} A\,dl$$

which is the product of the vector potential A on the path connecting the B-D and C-A, therefore, the sum is equal to the line integral of the ring. That is, it is proportional to the magnetic flux φ entering the ring.

$$(\mathrm{B}-\mathrm{D})+(\mathrm{A}-\mathrm{C}) = \frac{2\pi}{\varphi_0}\int_{\mathrm{A}\to\mathrm{C}\to\mathrm{D}\to\mathrm{B}} A\,\mathrm{dl}$$
$$= \frac{2\pi\varphi}{\varphi_0}$$

E.q. 2.4

Here, $\varphi_0 = \frac{\mathrm{h}}{2\mathrm{e}}$ is a magnetic flux quantum, h is Planck's constant and e is elementary charge. Therefore, the magnetic flux of the superconducting current enters the ring increases and decreases periodically. For this reason, the normal conduction current obtained by subtracting the superconducting current from the input current also increases or decreases periodically, and a voltage drop occurs periodically. This will read the change in the magnetic flux entering the ring as a voltage signal. The sample is vibrated up and down at a fixed frequency to generate a magnetic flux change at a certain frequency. Then, the induced current flows through the pickup coil, which inputs the magnetic flux to the SQUID element. The lock-in amplifier selectively reads the signal corresponding to the vibration frequency, and thus the magnetization of the sample can be measured.

The sample was cut out from the back surface of the sample to 2 mm × 6 mm with a diamond cutter and packed in a straw for measurement. A magnetization measuring device (MPMS3® manufactured by Quantum Design) was used for the measurement, which the schematic is shown in the figure 2.11. SQUID VSM is the combination of SQUID and VSM. Owing to superconducting magnet is used, the applied magnetic field of SQUID VSM is as larger as ± 70 k0e, the speed of sweep the magnetic field is high, as well as it's good at

controlling temperature during the measurement, comparing to the VSM, it's suitable for measurement of highly sensitive thin films. The measurement was performed with the vibration frequency of the sample being 14 Hz, the measurement temperature being 300 K, and -70 kOe $<\mu_0 H<70$ kOe.

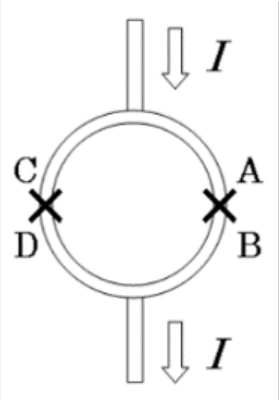

Fig. 2.10 The schematic of Josephson junctions in the superconducting ring.

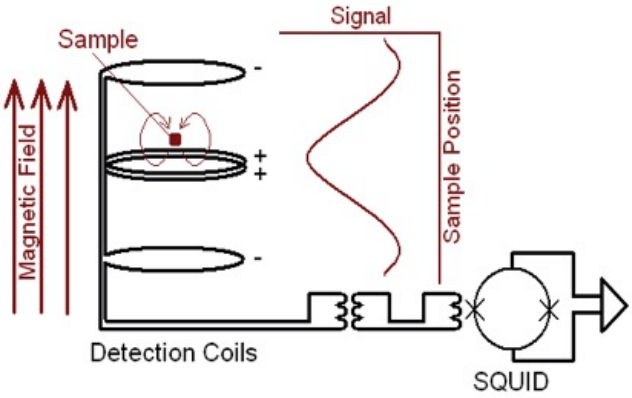

Fig. 2.11 The schematic of SQUID VSM.

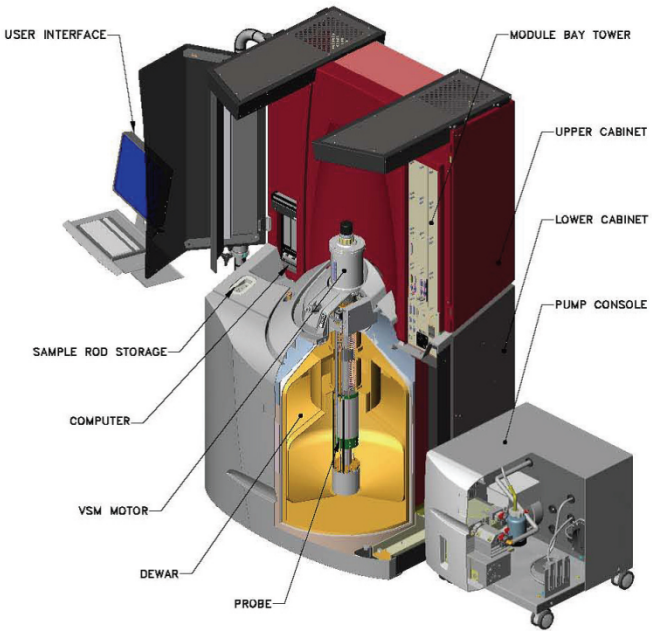

Fig. 2.12 The profile of SQUID VSM [40]

2.3.3 Scanning transmission electron microscope (STEM)

In this study, single crystalline of thin films were confirmed, also thickness of thin films before and after ion irradiation were compared from scanning transmission electron microscope (STEM) images, which were carried by JEOL, JEM-ARM200.

TEM, which is short for transmission electron microscope, it is a type of electron microscope. An electron microscope that transmits an electron beam to an observation sample, observing the spatial distribution of the electron transmittance in the observation sample by measuring the intensity of the transmitted electron beam. In some cases, according to the wave characteristics of electrons, the structure of the sample to be observed is observed in the interference image produced by electron diffraction in the sample. It is widely used in physics, chemistry, engineering, biology, medicine and so on.

STEM is a type of TEM, a microscopy technique where the electron beam probe finely focused by a focusing lens to a spot (with the type spot size 0.05 – 0.2 nm) which is then scanned over the sample in a raster illumination system constructed so that the sample is illuminated at each point with the beam parallel to the optical axis. The schematic diagram of STEM system is shown in the figure 2.11. STEM image is obtained by detecting transmission electrons at each point. Electron diffraction and elemental analysis in minute areas are possible. Spatial resolution is generally determined by the probe diameter of the focused electron beam.

STEM has the characteristic of obtaining a high-angle annular dark field scanning (HAADF) image, which reflects composition information can be obtained. The HAADF image is similar to TEM in that it is obtained images with scattered electron beams, but unlike TEM image of obversion with a specific direction, HAADF scatters around 360° by using a donut-shaped detector. It can capture electrons. Therefore, the effect of diffraction contrast is considerably weakened, and the contrast of the composition is increased in STEM. According to this characteristic, TEM is mainly used in the condition that if the information on the crystallinity of a sample is prioritized, on the other hand, STEM is used to obtain information on the composition of a sample.

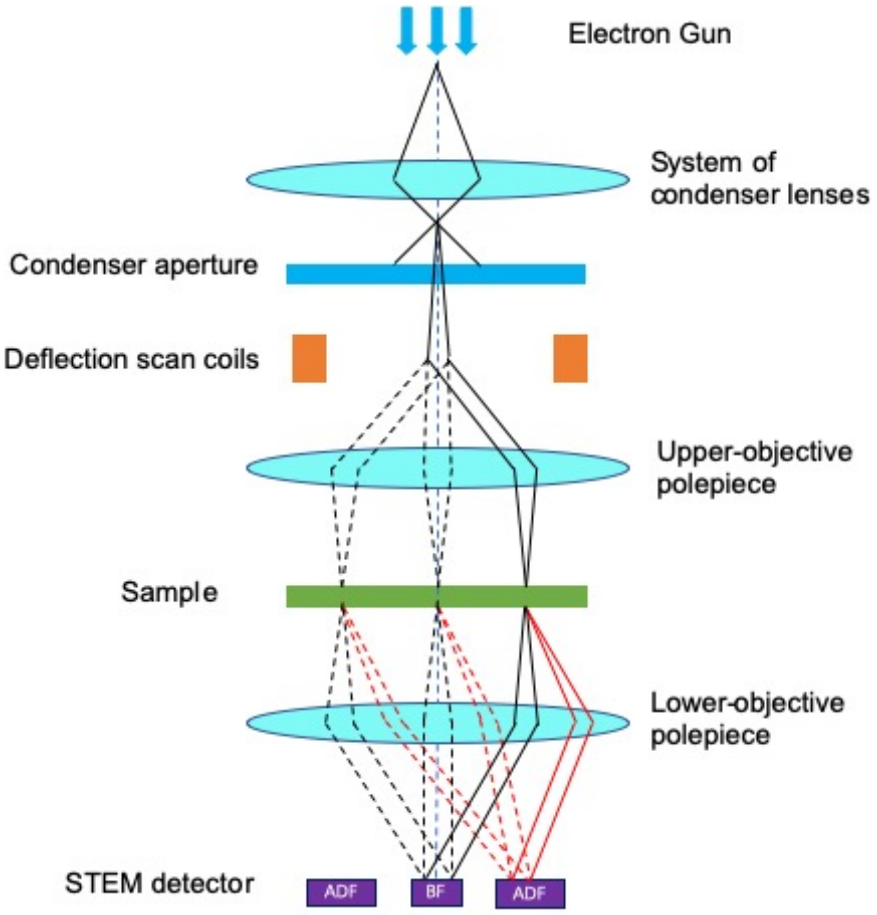

Fig. 2.11 The schematic diagram of STEM system.

2.3.4 X-ray reflectivity (XRR)

X-ray reflectivity (XRR) method is used to measure the film thickness of samples with a biaxial X-ray device (MiniFlex600 manufactured by Rigaku Co., Ltd.). When X-rays are incident on a crystal plane with a flat surface, total internal reflection occurs while the incident angle is smaller than the critical angle θ_c. Here, the critical angle changes depending on the electron density (corresponding to the refractive index) of the substance. When X-rays are incident on a thin film grown on a substrate, due to the difference in electron density between the thin film and the substrate, the reflection on the surface of the thin film interfere with the reflection at the interface composed of the thin film and the substrate, and a vibration pattern is generated in the obtained X-rays profile. At this time, if the interval of the vibration pattern is $\Delta 2\theta$, the film thickness d of the thin film can be obtained by using Bragg's equation (1) shown below.

$$2d \sin\left(\frac{\Delta 2\theta}{2}\right) = \lambda \qquad \text{E.q. 2.5}$$

Here, λ represents the wavelength of X-rays. A sealed Cu tube is used as the radiation source. In the measurement, the diffracted X-rays pass through a Ni filter to remove the K_β rays, a monochromatic Cu-K_α ($\lambda = 1.541838$Å) is used with a monochromator.

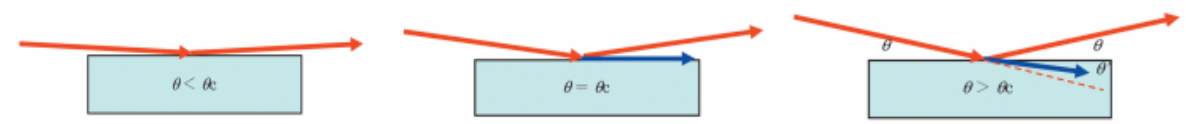

Fig 2.12 Reflection and reflection of X-rays at surface of thin films with the changes of grazing angle.

2.3.5 X-ray diffraction (XRD)

For the analysis of the crystal structure of the sample, X-ray diffraction (XRD) experiments at room temperature (RT) were carried out with a four-axis XRD diffraction station at beamline BL-4C of Photon Factory, High Energy Accelerator Research Organization (KEK). When X-rays are incident on a crystal, strongly scattered in a specific direction will be obtained due to the interference of regularly assembled atoms with scattered X-rays. This is a method to evaluate the lattice spacing and crystallinity of the sample to be measured based on the X-ray intensity and diffraction angle. Depending on the diffraction angle obtain from the diffraction pattern, information on the plane orientation, lattice constant, and lattice plane spacing of the sample can be obtained. Also, the half value width of the peak of the diffraction angle provides information on the crystallinity of the lattice plane. The figure 2.13 shows a schematic diagram of the 4-axis X-ray diffractometer (KEK's precision single crystal X-ray diffractometer) used in this study. It is equipped with four rotation axes, which are the 2θ axis of the scanning detector, and the ω axis, the χ axis and the φ axis correspond to the rotation axis of the sample, respectively. When XRD measurement is performed with a two-axis X-ray diffractometer that scans the ω axis and the 2θ axis, it is possible to obtain information of the lattice spacing only in the direction perpendicular to the lattice plane. In the case of 4-axis XRD measurement that scans all 4 axes, the lattice spacing in any direction can be obtained. In addition, the 4-axis X-ray diffractometer shown in Fig 2.13 is equipped with one slit on the Synchrotron side and two slits on the Detector side which contribute to the determination of X-ray divergence angle, irradiation area and resolution. In addition, in order to attenuate the intensity of X-rays emitted from Synchrotron, Attenuators with a thickness of 0.3 nm to 3.0 nm are available for different purposes.

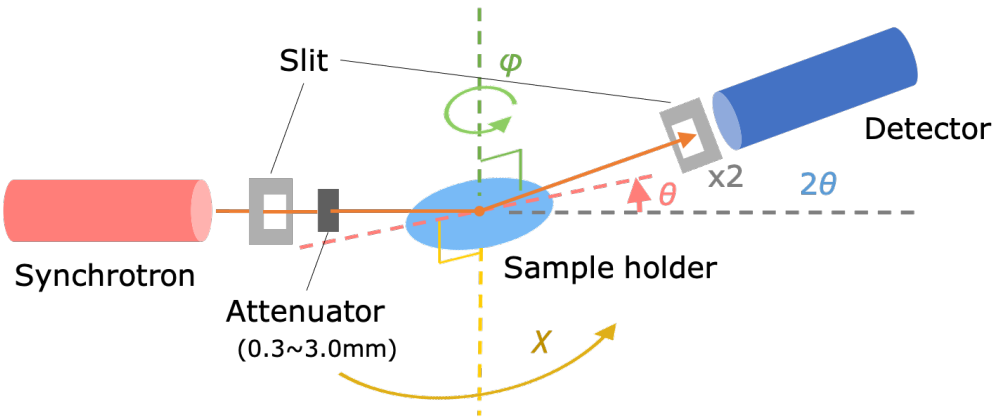

Fig. 2.13 The schematic diagram of 4-axis XRD system.

2.3.6 Rutherford backscattering spectrometry (RBS)

Rutherford backscattering spectrometry (RBS) is an ion scattering technique which widely used for structure and composition of thin film analysis. In RBS analysis, high energy ions are impinged on a sample and the energy distribution while a yield of backscattering ions at a given angle are measured. RBS can do quantitative compositional depth analysis without using reference standards, because the certainty of the backscattering cross section for each element. RBS is possible to measure thin films that are less than 1 μm, however for lower elements in the periodic table, the accuracy of measurement is lower[67].

It is a method to measure the energy and intensity of ions reflected backward from the sample surface by Rutherford backscattering by injecting a light ion beam such as hydrogen or helium of MeV level of energy onto a solid sample. It is possible to investigate the composition, amount, and depth distribution of atoms contained in a solid. Since the data such as the scattering cross section and energy loss (stopping energy) in the sample used for quantification are highly reliable, it is possible to analyze the composition in the depth direction without using a standard sample.

The principle of elemental analysis in a sample by RBS is based on the fact that the energy of Rutherford scattered ions in one direction by an atom depends on the mass of that atom. The relational expression can be derived from the equation 2.2 of binary collision in classical mechanics as shown in the figure 2.13. The k in the formula is called the kinematic factor (k-factor).

$$E_1 = \left(\frac{M_1 \cos\theta + \sqrt{M_0^2 - M_1^2 \sin^2\theta}}{M_1 + M_0} \right) E_0 = kE_0 \qquad \text{E.q. 2.6}$$

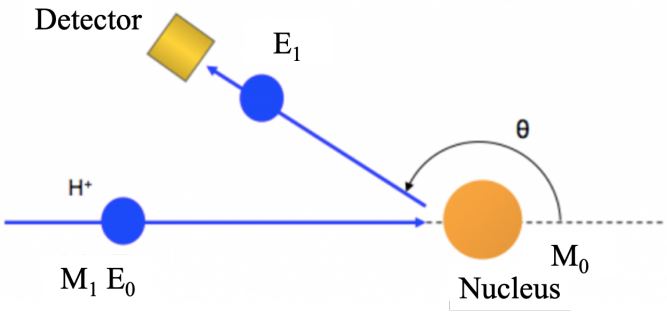

Fig. 2.13 The relational expression can be derived from the equation 2.2 of binary collision in classical mechanics.

In RBS analysis, the energy spectrum of backscattered ions is measured with a semiconductor detector. Since the energy and mass number of the incident ion are known, the mass number of the target atom can be identified from the formula by placing a semiconductor detector at a certain angle and measuring the energy of the backscattered ion. In RBS analysis, when a sample is composed of two elements, how small the mass difference (energy difference) can be distinguished, that is, the mass resolution is important, and the k-factor is an index.

The figure 2.14 shows the target atomic mass dependence of the k-factor with respect to the incident ion species. The scattering angle is 165 degrees, which is typical of RBS analysis. From the figure, the smaller the target atomic mass, the larger the rate of change of the k-factor, and the larger the target atomic mass, the smaller the rate of change of the k-factor. It can be seen that the heavier the atomic mass, the lower the mass resolution tends to be. Helium ions are often used as incident ions in RBS analysis because only forward scattering occurs when the target atom is lighter than the incident ions. The figure 2.15 shows the target atomic mass dependence of the k-factor with respect to a typical scattering angle. The mass of the target atom is about 30 amu, and the rate of change of the k-factor with respect to the mass increases as the scattering angle increases. Under the same conditions of ion type and energy to irradiate in this way, it is easier for the target atom to identify the element if the scattering angle is set to a position close to 180 degrees.

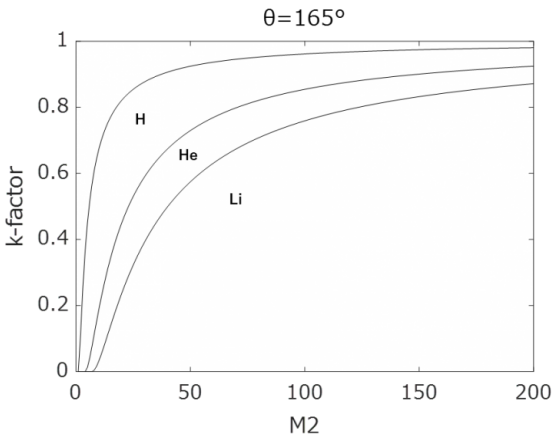

Fig. 2.14 Incident beams dependence of k-factor.

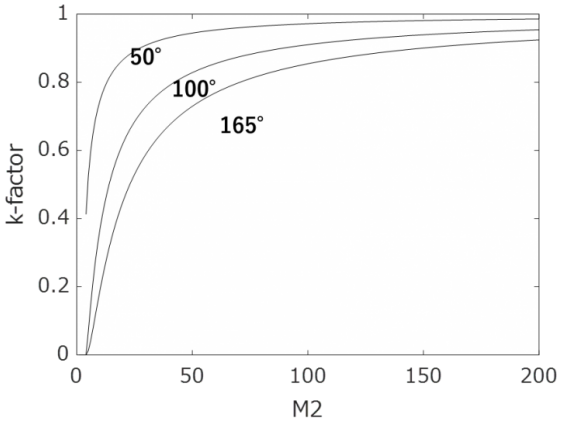

Fig. 2.15 Angle dependence of k-factor.

In this work, RBS measurement was carried out in University of Tsukuba Tandem Acceleration Complex (UTTAC). The figure 2.16 shows the layout of the 6 MV. Pelletron tandem accelerator facility. [UTTAC annual report] This time, RBS measurement is carried out with chlorine of acceleration of 40 MeV.

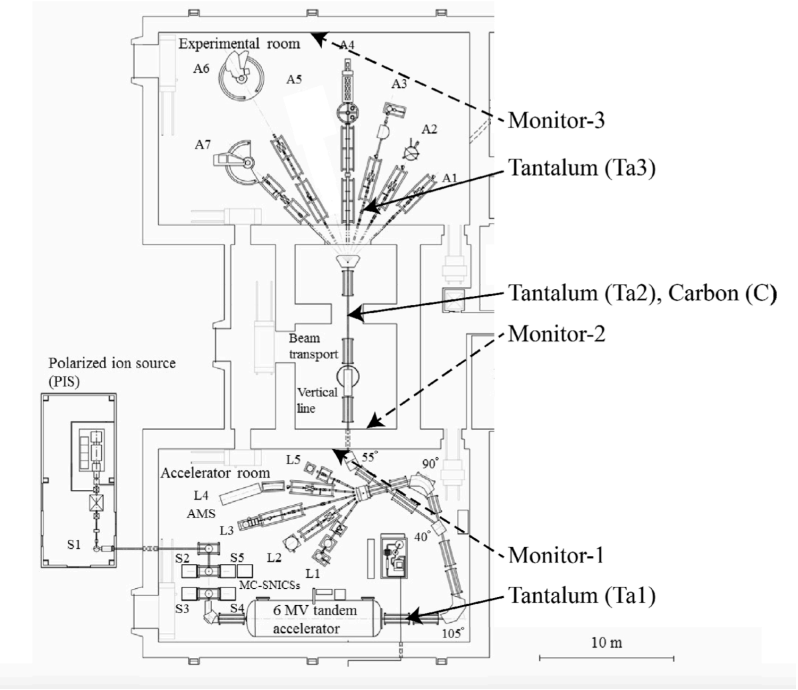

Fig. 2.16 Layout of the 6 MV Pelletron tandem accelerator facility. Solid arrows indicate the positions of beam stoppers: tantalum (Ta1, Ta2 and Ta3) and carbon I. Dashed arrows indicate the positions of three pairs of area monitors for gamma-ray and neutron (Monitor-1, Monitor-2 and Monitor-3).

2.3.7 Mössbauer spectroscopy

Mössbauer spectroscopy is a method for investigating the information of an element in a substance, such as the valence, electronic structure and magnetism. So far, radioisotope sources have been mainly used. The Mössbauer effect is a phenomenon in which nuclei in atoms emit or absorb γ-rays without loss of energy and has been observed for specific nuclei. The process of emission and absorption of γ-rays is always accompanied by changes and splits in energy levels, which are influenced by electronic and magnetic surrounding environments. The information of the local environment (electronic and magnetic) of the atoms in the system can be provided by these changes in energy levels and could be observed using resonance fluorescence.

Mössbauer spectroscopy can be described using three parameters of the principal hyperfine interactions, with these three parameters Mössbauer spectroscopy can be fitted and obtained information of samples[68].

(1) isomer shift (δ), which arises from the electric monopole interaction.

(2) quadrupole splitting (Δ), which is a shift in nuclear energy levels that is induced by electric dipole interaction.

(3) magnetic hyperfine field (B_{hf}), when acts at the nuclei of the resonant atoms induced the magnetic hyperfine interaction.

The shift of the spectral centroid form zero velocity is called the isomer shift (IS). Zero velocity is based on some standard material. Simulated Mössbauer spectrum resulting from the isomer shift is shown in the figure 2.17. For example, α-Fe is used as a standard sample for ^{57}Fe. Quadrupole splitting is the separation of two lines of an ^{57}Fe doublet. The isomer shift is related to the oxidation state of iron, which may provide the

coordination information of iron, while the quadrupole split provides a measure of Fe^{3+} site distortion. Quadrupole splitting for 3/2 to 1/2 transition is shown in the figure 2.18. The magnitude of quadrupole splitting, Δ is revealed. Both isomer shift and quadrupole splitting are customarily given in terms of the source velocity in mm/s. The internal (hyperfine) or external (externally applied) magnetic fields divides the Fe^{3+} Mössbauer spectra into sextets. Magnetic splitting of the nuclear energy levels is indicated in the figure 2.19. The simple schematic Mössbauer spectroscopy measurement is given in the figure 2.20, γ-rays source is set on a vibration device, the sample is set between γ-rays source and counter which is used for measuring the γ-rays or internal conversion electron.

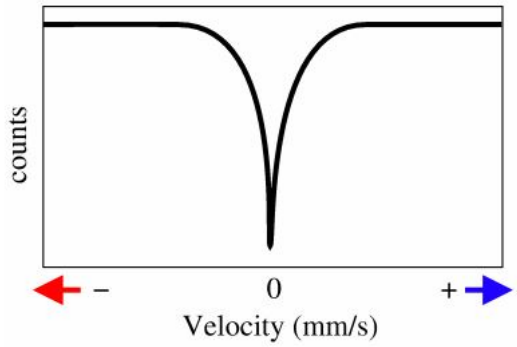

Fig. 2.17 Simple spectrum showing the velocity scale and motion of source relative to the absorber.

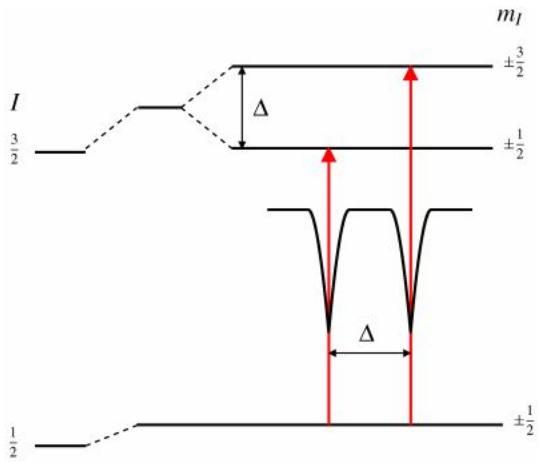

Fig. 2.18 Quadrupole splitting for 3/2 to 1/2 transition. The magnitude of quadrupole splitting, Δ is shown.

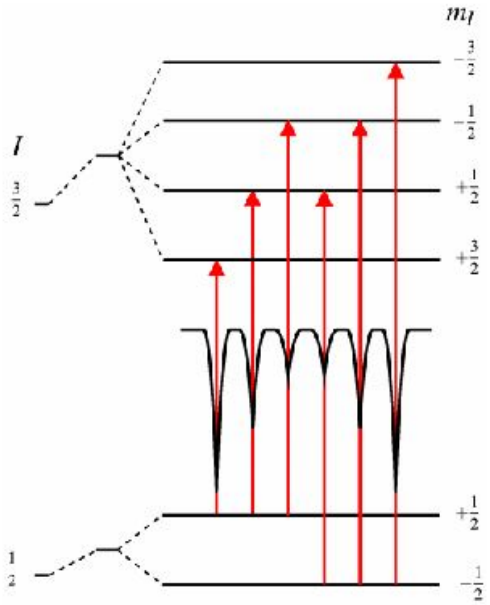

Fig. 2.19 Magnetic splitting of the nuclear energy levels.

As we mentioned above, according to the measurement method, there are two types of measurement, transmission type and electron counting type in other word internal conversion electron Mössbauer spectroscopy (CEMS). In the transmission type measurement, the γ-rays that have passed through the sample are counted to obtain an absorption spectrum that reflects the electronic state of the atoms in the sample. The figure 2.21 shows the typical experimental setups for transmission Mössbauer spectroscopy. Simulated Mössbauer spectra resulting from the hyperfine interactions of transmission type is revealed in the figure 2.23. In addition, nuclei that have absorbed γ-rays also emit internal conversion electrons along with γ-rays when deexcited. By using this electron counting method (internal conversion electron method, CEMS), it is possible to measure samples that γ-rays could not pass through, such as thin films on substrates[69]. The figure 2.22 shows the typical experimental setups for conversion electron Mössbauer spectroscopy. Simulated Mössbauer spectra resulting from the hyperfine interactions of conversion electron type is revealed in the figure 2.24.

In this study, conversion electron Mössbauer spectroscopy (CEMS) is used for measurement for thin film sample. The nuclei absorbed gamma rays, during de-excitation, will emit a conversion electron. With the special counter for measuring the conversion electron, as given in Fig. 2.20, CEMS can be obtained. The counter can collect essentially all the electrons which leave from the surface of the sample. The sample is set inside of the counter. With the measurement to count the conversion electron, it's possible to measure the thin film which the gamma ray can't go through.

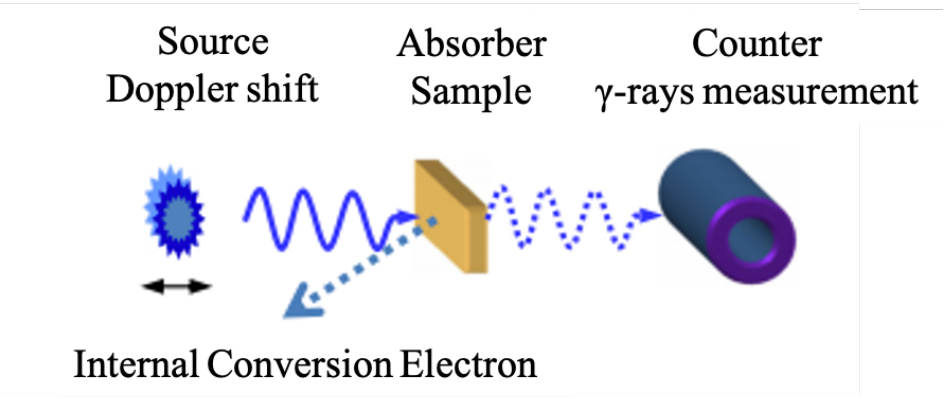

Fig. 2.20 The schematic of Mössbauer spectroscopy measurement.

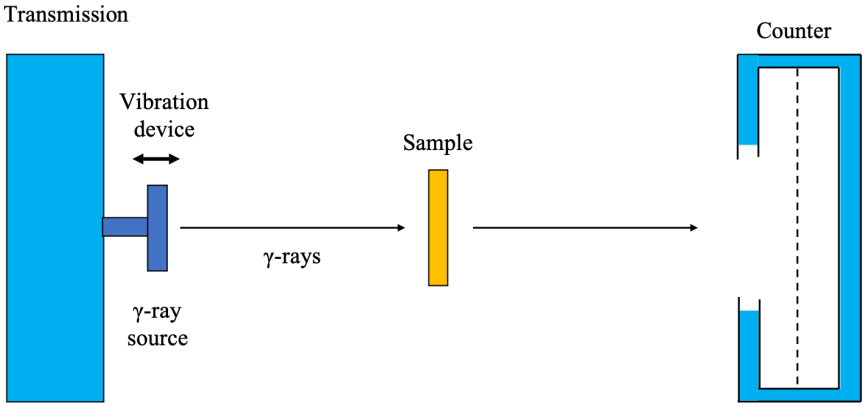

Fig. 2.21 The typical experimental setups for transmission Mössbauer spectroscopy.

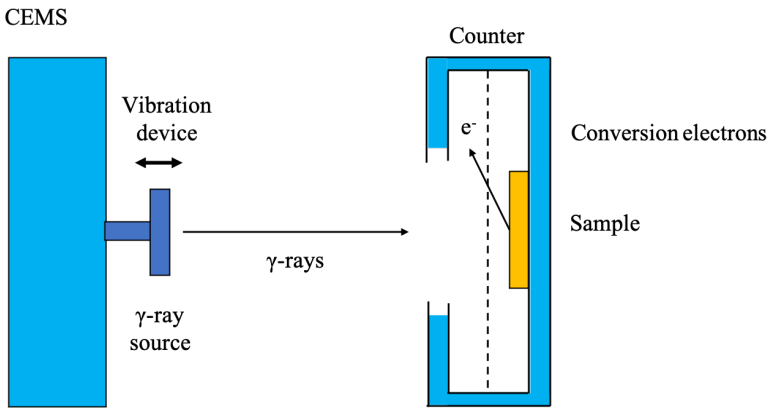

Fig. 2.22 The typical experimental setups for conversion electron Mössbauer spectroscopy.

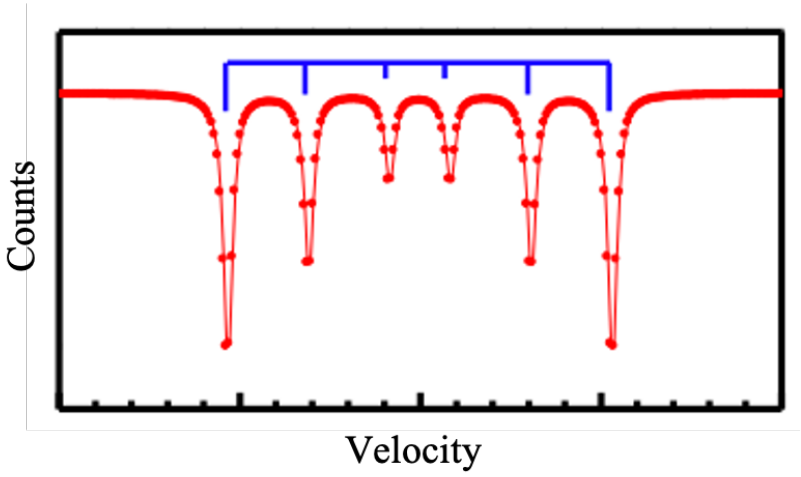

Fig. 2.23 Simulated transmission Mössbauer spectroscopy.

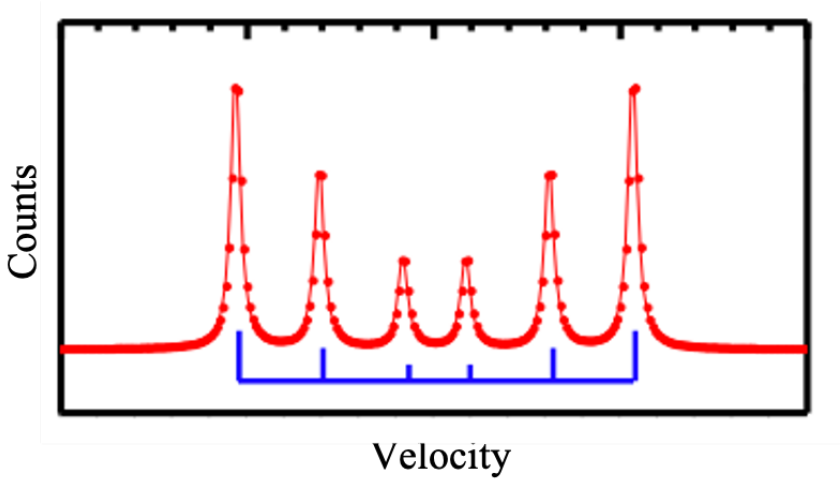

Fig. 2.24 Simulated conversion electron Mössbauer spectroscopy.

Features of ^{57}Fe Mössbauer spectroscopy

- The valence state of iron atoms in compounds and oxides.
- Magnetic state of matter (paramagnetism, ferromagnetism).
- Crystalline environment of matter (quadrupole splitting).
- Measurement of thin film and nanoparticle (powder) samples is possible.

Measurement environment at the University of Tsukuba Tandem Acceleration Complex (UTTAC).

- Sample temperature: Low temperature 2.6K to room temperature (refrigerator, bath type cryostat), room temperature to 220 ℃. The temperature measure of Mössbauer spectroscopy is only can be carried out for powder sample. For CEMS, only room temperature can be carried out.
- Magnetic field: 0-5 T (5-300 K) Superconducting magnet.
- Surface-sensitive measurement by internal conversion electron method.

2.3.8 Stopping and range of ions in matter (SRIM)

The stopping and range of ions in matter (SRIM) simulation calculation was carried out before ion irradiation process. In order to determine the condition of ion irradiation on different component and thickness of thin film, the thickness of carbon layer is also confirmed by SRIM simulation.

SRIM is simulation software for calculating such as the range of ions, damage, etc., when high speed ions pass through the material[70]. In general, SRIM is a method of tracking the trajectory of the incident ion and the target material atom that has been ejected by the collision by sequentially applying the binary collision model to the incident ion and the target material.

The interactions of atoms that moving in a solid at high speed are always considered as 'collisions' between nuclei and 'stopping power' induced by the interaction between electrons. We consider an atom or nucleus as a sphere; the motion of the colliding atoms can be solved in the category of classical mechanics with the binary collision. At this time, the necessary information in advance is as follows.

- Mass of incident atom and target atom.
- Velocity of incident atom (Energy).
- Positional relationship between incident atom and target atom (Impact parameter).
- Interaction between incident atom and target atom.

For the interaction between incident atom and target atom, if the incident atom and the target atom are assumed completely as point-charged, the interaction between each other is a simple Coulomb force. In reality, there are electrons (ions) around the nucleus of each atom. In SRIM, the shield model by Ziegler, *et. al.* is used to shield the Coulomb force between electrons (ions) around the nucleus of each atom. Due to the interaction between the nuclei and a large number of electrons existing in the solid, as well as the collisions between the nuclei, there is energy loss when atoms move at high speed in a solid. This energy loss depends on:

- Electron density of solid (atomic number and atomic density of target material).
- Charge of incident nucleus (atomic number of incident nucleus).
- Velocity of incident atom (energy).

When the incident ions pass through a thin target material, the incident ions change their movement direction and reduce their energy due to the influence of the two types of interactions mentioned above. This energy reduction depends on how many collisions occur with the atoms in the target (impact parameters) and how many collisions occur in the target material (mean free path). It can be expected that the value will settle to a certain average value after repeated trials. The amount of energy that is reduced when an atom moves a unit length is called "stopping power". In particular, the energy loss due to the interaction between atomic nuclei is called nuclear stopping power, and the energy loss due to interaction with electrons is called electronic stopping power.

When an atom in the target material collides with an incident ion, that atom gains kinetic energy. After repeating this process, the energy and kinetic direction of the collided atom due to the collision varies depending on the conditions. If the target is only the incident atom and this collided atom, the collided atom will move away from its original position. However, in many simulations, the collided atom is with other target

material atoms around it. Because they are connected, there should be a force that tries to stay in their original position. SRIM defines the following two types of energies for each target material regarding how atomic ejection occurs.

Displacement Energy: If the energy of the collided atom is less than or equal to Displacement Energy, the atom does not move from its original position. This energy of 10eV to 20eV is considered appropriate. The received energy is dissipated as lattice vibration with adjacent atoms. In SRIM, it is calculated as "energy received by Phonon".

Lattice Binding Energy: If the energy of the collided atom E_2 is larger than the displacement energy, the atom shakes off the bond with the surrounding atom and jumps out from the original position. At this time, the collided atom is the Lattice Binding Energy component. Suppose that the energy of is left in the original position and moves. That is, the collided atom has the kinetic energy obtained by subtracting the Lattice Binding Energy from E_2. On the other hand, the place where the collided atom originated becomes a lattice defect (vacancy), so the Lattice Binding Energy can be regarded as the energy for creating the lattice defect.

In addition to this, the following energies are defined. Surface Binding Energy: Similar to Displacement Energy, but this energy is applied to the target atom near the surface. If the atom near the surface has more energy (and momentum toward the vacuum) than the Surface Binding Energy, the atom desorbs from the target material. It shall be separated (spattered).

The SRIM algorithm can be summarized as follows. Select one incident atom (or other high-energy atom), moving by the mean free path in the material. At that time, the energy dissipation due to the stopping power is calculated. Then simulate as a binary collision. The collision coefficient with the target atom is determined by a random number, and the incident atom after the collision, the moving direction of the target atom, and the energy are determined.

Determine the displacement of the target atom (and the stoppage of the incident atom). If the incident atom and the target atom each have a larger energy than the Displacement Energy, subtract the Lattice Binding Energy, and the "high energy atom" in 1. (Or, if the target atom is near the surface, determine the spatter).

Repeat 1-3 until all atoms have stopped.

The main parameters that are important in the simulation are as follows.

- Incident ion

  Atomic number, Mass, Energy.
- Target material (can be composed of multiple layers)

  Density, Thickness, Constituent atoms, Atomic number, Mass, Composition ratio, Displacement Energy, Lattice Binding Energy, Surface Binding Energy.

Of these, {Displacement, Lattice Biding, Surface Binding} Energy is the only parameter that is difficult to determine uniquely, and in most cases the default value is used.

Features and benefits:

- Calculation of ion injection range.
- Calculation of the number and distribution of damage caused by ejection.

- Calculation of spatter rate.
- Calculation of energy dissipation due to factors other than ejection (phonon scattering, electronic device capability).
- Calculation is possible at a relatively high speed.
- The parameters required for the calculation are simple, concrete and easy to understand.

Here, a briefly explanation of calculations performed by SRIM is carried out, and the parameters required for SRIM calculations.

3. Results and discussion

3.1 RHEED and TEM image

The RHEED image were taken at the time that MgO substrate was transformed into main chamber and immediately after thin film was grown on substrate. RHEED images for MgO substrate and Fe_3O_4 thin film is shown in Figure 3.1. Fig. 3.1(a) reveals the MgO substrate and (b) reveals the fabricated Fe_3O_4 thin film after sputtering. The same as Fe_3O_4, RHEED images of MgO (001) substrate and $CoFe_2O_4$ thin film after sputtering is shown in Figure 3.2. The clear Kikuchi lines and streak patterns in both Fig. 3.1(b) and Fig. 3.2(b) indicate high crystallinity and a very flat surface in the Fe_3O_4 thin film and $CoFe_2O_4$ thin film epitaxially grown on MgO substrate, respectively. The Fe_3O_4 thin film and $CoFe_2O_4$ thin film show typical diffraction patterns from the (0 0 1) plane of the spinel structure.

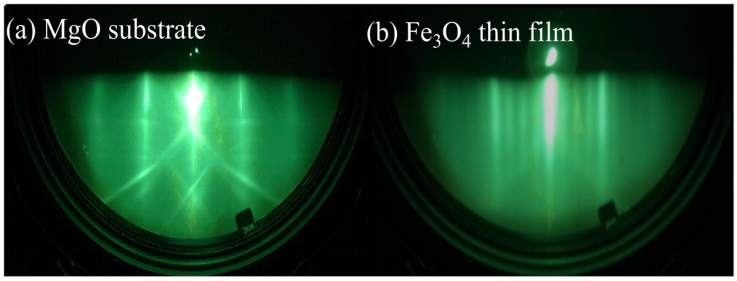

Fig. 3.1 RHEED patterns of samples before sputtering (MgO substrate) and after sputtering (Fe_3O_4 thin film). The streak patterns clearly show the epitaxial growth of Fe_3O_4 thin film.

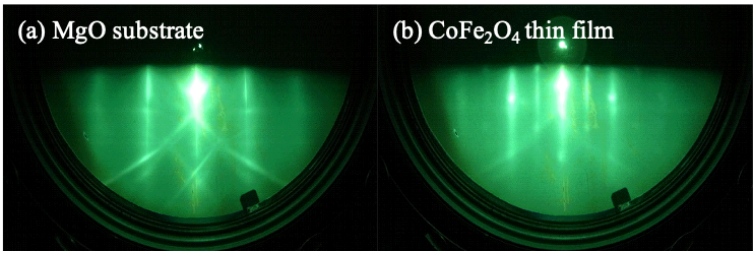

Fig. 3.2 RHEED patterns of samples before sputtering (MgO substrate) and after sputtering ($CoFe_2O_4$ thin film). The streak patterns clearly show the epitaxial growth of $CoFe_2O_4$ thin film.

TEM image of fabricated both Fe_3O_4 and $CoFe_2O_4$ thin films were carried out. The carbon layer was coated for preparing the ion irradiation process, also was confirmed both on Fe_3O_4 and $CoFe_2O_4$ thin film. The both Fe3O4 and CoFe2O4 thin film revel highly single crystalline and flat surface.

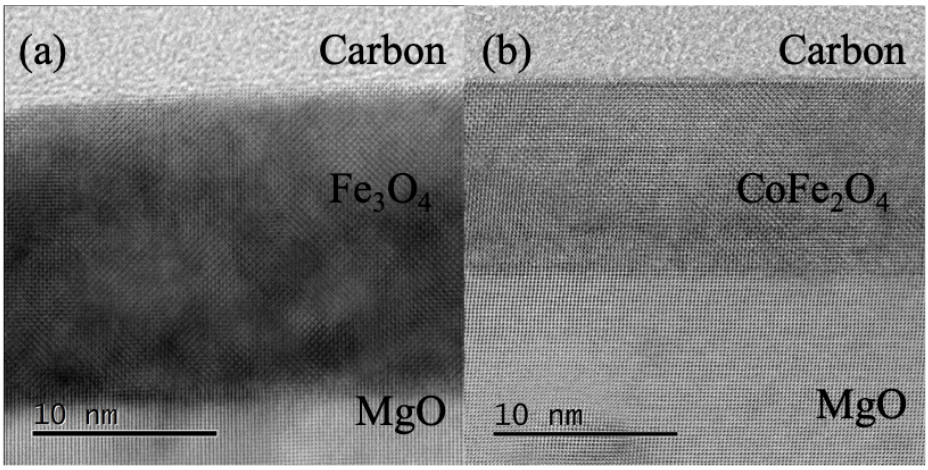

Fig. 3.3 (a) TEM images of Fe_3O_4 thin film and (b) $CoFe_2O_4$ thin film.

The figure 3.4 indicates the representative profile of the measurement of thickness of $CoFe_2O_4$ thin film sample by X-Ray Reflectivity. All the thin films samples will obtain the roughly same profile of the measurement of thickness of $CoFe_2O_4$ thin film sample by X-Ray Reflectivity. According to the profile, the intensity of reflection corresponds to the vibration of 2θ is concluded. Depends on this, the flatness of thin films samples will be confirmed. According to the Eq. 2-1, it's possible to calculate the thickness of the $CoFe_2O_4$ thin films samples.

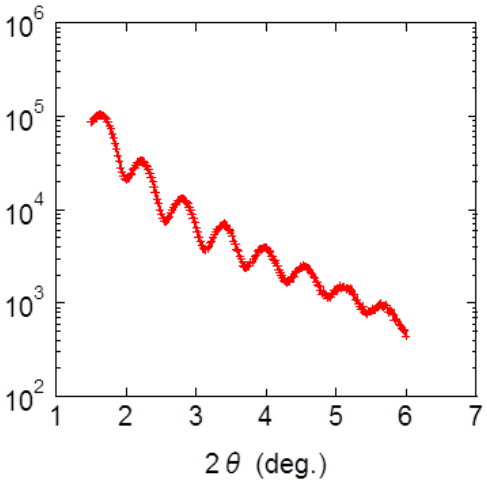

Fig 3.4 Profile of the measurement of thickness

3.2 SRIM simulation

Before ion irradiation, SRIM simulation calculating was carried out to confirm the condition of ion irradiation. Figure 3.5 shows one of the simulation results of $CoFe_2O_4$ thin film with 15 nm carbon coating under the irradiation condition which indicates in table 3.1. The results indicate that most Kr ions affect the $CoFe_2O_4$ thin film then finally stop in MgO substrate.

Table 3.1 The ion irradiation condition of Fig. 3.4 simulation calculating results.

Carbon layer	**15 nm**
Source	Krypton
Accelerate voltage	30 kV
Dosage	1×10^{16} ions/cm^2

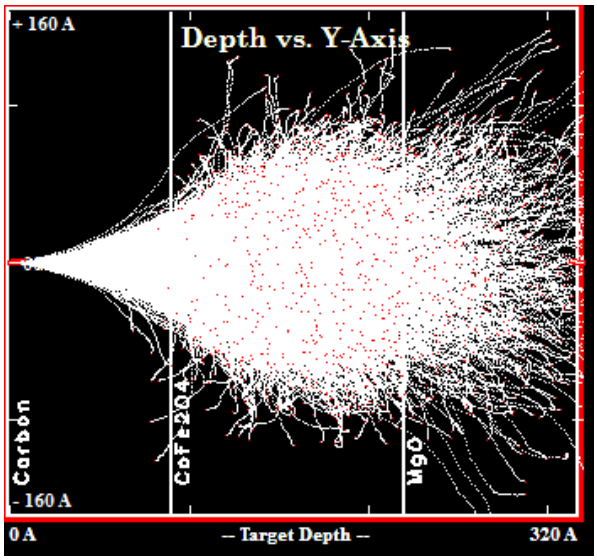

Fig. 3.5 SRIM simulation calculating result for $CoFe_2O_4$ thin film.

3.3 Magnetization measurement

The magnetization of thin films was carried out before and after ion irradiation different dose of Kr ions. The dose of ion irradiation is from 1×10^{15} ions/cm^2 to 1×10^{16} ions/cm^2 for $CoFe_2O_4$ thin film to confirm the relationship between magnetization and dose of Kr ions. Figure 3.6 gives the M-H loops of $CoFe_2O_4$ thin film without ion irradiation and Kr ion-irradiated thin film with 2×10^{15} ions/cm^2, 5×10^{15} ions/cm^2 and 1×10^{16} ions/cm^2, respectively. According to the M-H loops, the saturation magnetization of $CoFe_2O_4$ thin film decrease obviously with the increase of Kr dosage. The saturation magnetization of $CoFe_2O_4$ thin film almost decrease to 0 when dosage of Kr ions reaches 1×10^{16} ions/cm^2.

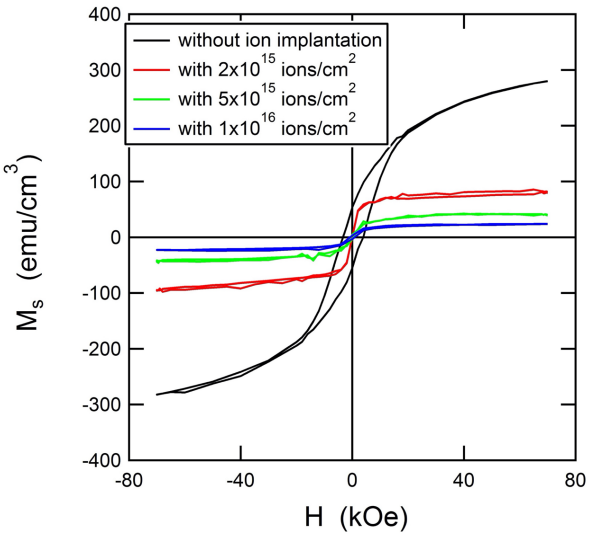

Fig. 3.6 M-H loops of $CoFe_2O_4$ thin film without ion irradiation and Kr ion-irradiated thin film with 2×10^{15} ions/cm^2, 5×10^{15} ions/cm^2 and 1×10^{16} ions/cm^2, respectively.

The similar result is obtained on the 1×10^{16} ions/cm^2 dose ion-irradiated Fe_3O_4 thin film. M-H loops of Fe_3O_4 thin film without ion irradiation and after 1×10^{16} ions/cm^2 dose Kr ion irradiation is shown in Figure 3.7. the saturation magnetization of Fe_3O_4 thin film nearly vanished after 1×10^{16} ions/cm^2 dose Kr ion irradiation. The Nitrogen ions also have been carried out on Fe_3O_4 thin film. The results are given in Figure 3.8. The plot summarizes the N_2 ions and Kr ions irradiation on Fe_3O_4 thin film and Kr ions on $CoFe_2O_4$ thin film. The vertical axis represents the saturation magnetization, and the horizontal axis represents the dosage of N_2 or Kr ions. It reveals that both the saturation magnetization of $CoFe_2O_4$ thin film and Fe_3O_4 thin film decrease during an increased dose of ion irradiation and finally disappeared when at a particular dose of ion irradiation. In addition, Kr ions are considered more effective than N_2 ions, owing to more N_2 ions are needed than Kr ions to make saturation magnetization of Fe_3O_4 thin film vanished.

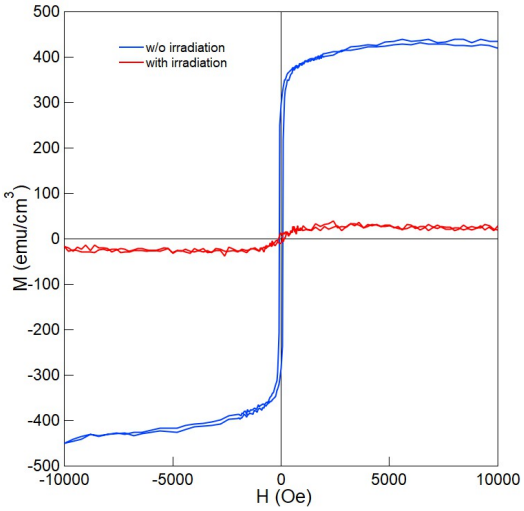

Fig. 3.7 M-H loops of Fe_3O_4 thin film without ion irradiation and Kr ion-irradiated thin film with 1×10^{16} ions/cm^2.

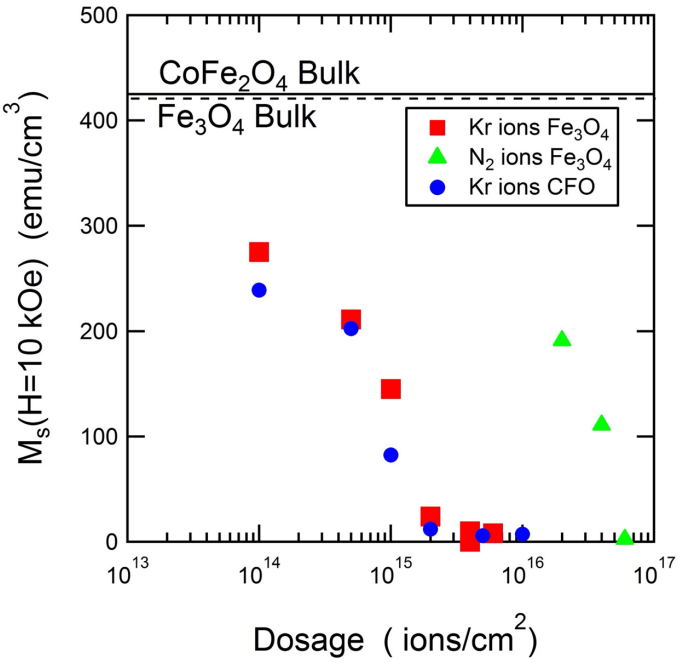

Fig. 3.8 Plot of the saturation magnetization of $CoFe_2O_4$ thin film and Fe_3O_4 thin film with different dose of N_2 ions and Kr ions.

For Mössbauer study, we custom-made a thin, annular tablet with a thickness of 1 mm out of 25% enriched ^{57}Fe and placed it over the erosion region of a natural Fe sputter target. The schematic is shown in Figure 3.9. Using this ^{57}Fe-enriched target system, $CoFe_2O_4$ thin film and Fe_3O_4 thin film contain ^{57}Fe were fabricated.

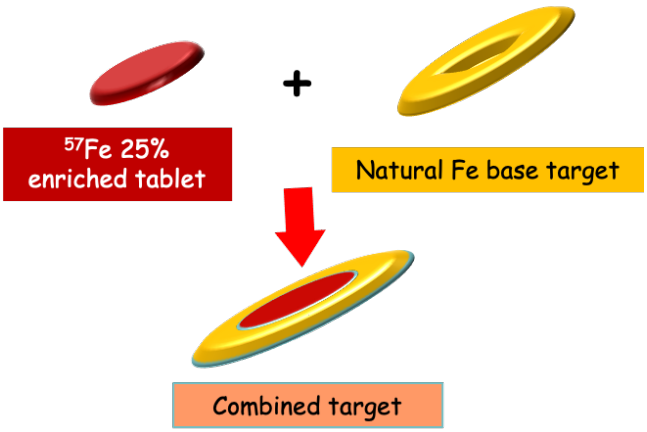

Fig. 3.9 The schematic of special ^{57}Fe target.

In this study, to understand the mechanism of the decrease in magnetization of $CoFe_2O_4$ thin film and Fe_3O_4 thin film, the Mössbauer was performed. Mössbauer spectroscopy of $CoFe_2O_4$ thin film and Fe_3O_4 thin film without ion irradiation and ion-irradiated $CoFe_2O_4$ thin film and Fe_3O_4 thin film were measured with the method of CEMS at room temperature. Table 3.2 indicates the specific corresponding situation.

Table 3.2 Mössbauer spectroscopy for different dose and samples.

Sample	Dose (Kr)
$CoFe_2O_4$	0
$CoFe_2O_4$	1×10^{15} ions/cm^2
$CoFe_2O_4$	1×10^{16} ions/cm^2
Fe_3O_4	0
Fe_3O_4	1×10^{16} ions/cm^2

The Figure 3.10 shows Mössbauer spectroscopy of $CoFe_2O_4$ thin film (a) without ion irradiation, (b) 1×10^{15} ions/cm^2 Kr ion irradiation, and (c) 1×10^{16} ions/cm^2 Kr ion irradiation. The spectra for $CoFe_2O_4$ thin film without ion irradiation are plotted as a reference in Fig. 3.10 (a), which is consistent with previous study [], and were fitted to the combination of magnetic subspectra (sextet) with bulk parameters. The isomer shift (IS) represents Fe^{3+} occupied in tetrahedral site (A site) and octahedral site (B site), respectively. The Mössbauer spectra of $CoFe_2O_4$ thin films with Kr ion irradiation are in Fig. 3.10 (b) and (c), irradiated by Kr ions 1×10^{15} ions/cm^2 and 1×10^{16} ions/cm^2, respectively. The spectra of the low irradiation (1×10^{15} ions/cm^2) sample was fitted to the combination of a weak broad magnetic sextet and nonmagnetic singlet. The area ratio of a ferromagnetic component is estimated to be 34% and coincides with the magnetization of about 40% of as prepared sample. The increasing of irradiated Kr ions resulted in an increase of the paramagnetic component, and after the strong irradiation, the ferromagnetic parts shown in the Mössbauer spectra before ion irradiation almost disappeared. The 1×10^{16}ions/cm^2 Kr ion-irradiated Mössbauer spectra was fitted by two singlets (non-magnetic). The large IS of 0.88 are considered as $Fe^{2.5+}$ (contain Fe^{3+} and Fe^{2+}) which is consist to reference. This result represents the appearance of Fe^{2+}. Table 3.3 shows the parameters of fitting of $CoFe_2O_4$ thin films with/without ion irradiation.

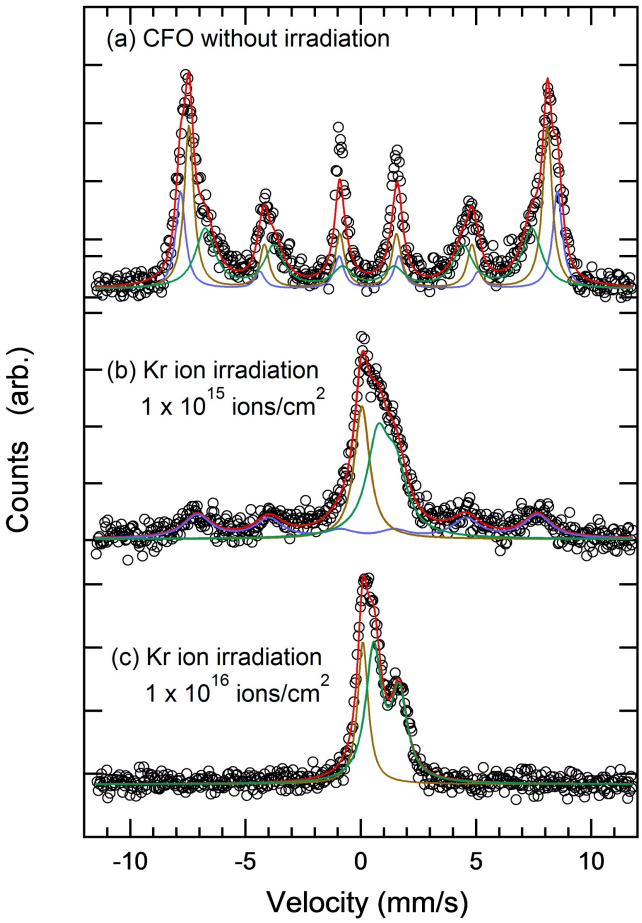

Fig. 3.10 Mössbauer spectroscopy of $CoFe_2O_4$ thin film (a) without ion irradiation, (b) 1×10^{15} ions/cm^2 Kr ion irradiation, and (c) 1×10^{16} ions/cm^2 Kr ion irradiation. Solid lines show results of numerical fitting. Fitting parameters are listed in Table 3.3.

Table 3.3 The fitting parameters of Mössbauer spectra before and after ion irradiation. Isomer shifts (IS) were defined with respect to α-Fe at RT. The parameters of fitting of $CoFe_2O_4$ thin films with/without ion irradiation.

Dose	Site	H (kOe)	IS (mm/s)	Area (%)	A25/A34
Without irradiation	Magnetic1	508	0.35	63	0.58/1
	Magnetic2	444	0.33	38	
1×10^{15}ions/cm^2	Magnetic1	458	0.31	34	2.51/1
	Non-magnetic	-	0.61	66	
1×10^{16}ions/cm^2	Non-magnetic1	-	0.48	57	0
	Non-magnetic2	-	0.88	43	

The decrease in saturation magnetization was also confirmed by Mössbauer spectra not only in $CoFe_2O_4$ thin film but also in Fe_3O_4 thin film. The Mössbauer spectra are shown in Figure 3.11 The spectra for as-grown Fe_3O_4 thin film was fitted with a combination of two hyperfine subspectra, attributed to high spin Fe^{3+} in tetrahedral sites (A site) and $Fe^{2.5+}$ (Fe^{2+} and Fe^{3+}) in octahedral sites (B site), respectively. The hyperfine fields (H_{hf}) are 486 kOe and 452 kOe, almost the same magnitude as those for bulk magnetite, 491 kOe for Fe^{3+} (A site) and 460 kOe for $Fe^{2.5+}$ (B site).[16-19] The fitting parameters for Fe_3O_4 thin films are presented in Table 3.4. On the other hand, the magnetic components were not observed in the spectra for the ion-irradiated film in the lower half part of Fig. 3.11. Spectra was fitted with two nonmagnetic singlets without any hyperfine filed (H_{hf}) distribution, corresponding to paramagnetic components. Before Kr ion irradiation, the Mössbauer spectra of Fe_3O_4 thin film were fitted with IS of 0.15 represents for Fe^{3+} in tetrahedral sites (A site) and IS of 0.51 represents for $Fe^{2.5+}$ (Fe^{2+} and Fe^{3+}) in octahedral sites (B site). After Kr ion irradiation, the Mössbauer spectra were fitted with one singlet with IS of 0.29 which is similar with Fe^{3+}, the other singlet with IS of 1.23 which is similar with Fe^{2+} in reference[71,72,73]. The Mössbauer spectra represent that the magnetization of Fe_3O_4 thin film disappear via ion irradiation. In addition, IS represents both the exist of Fe^{3+} and Fe^{2+}, and considering of area ratio, Fe^{3+} : Fe^{2+} nearly consist with Fe_3O_4 (2:1).

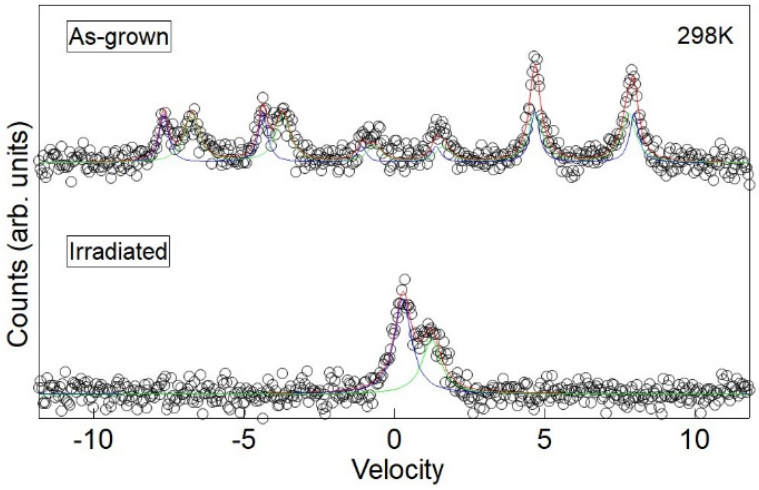

Fig. 3.11 Mössbauer spectra for Fe_3O_4 thin film and 1×10^{16} ions/cm^2 Kr ion-irradiated Fe_3O_4 thin film. Solid lines show results of numerical fitting. Fitting parameters are listed in Table 3.4.

Table. 3.4 The fitting parameters of Mössbauer spectra before and after ion irradiation. Isomer shifts (IS) were defined with respect to α-Fe at RT. Quadrupole splitting (QS) for the Fe_3O_4 films were negligibly small.[16-19]

	Subspectra	H_{hf} (kOe)	IS (mm/s)	QS (mm/s)	area
As grown	M1	486	0.15	0.002	40.0%
	M2	452	0.51	0.04	60.0%
Irradiated	Singlet	-	0.29	-	61.5%
	Singlet2	-	1.23	-	38.5%

The Mössbauer spectra for non-magnetic Fe_3O_4 thin films with $4 \times 10^{15} \mathrm{ions/cm^2}$ and $CoFe_2O_4$ with $1 \times 10^{16} \mathrm{ions/cm^2}$ Kr ions irradiation were plotted in Figure 3.12. The spectra were resembled and fitted to the combination of a singlet and a doublet, corresponding to Fe^{3+} on A sites and B sites. It was supposed that the crystal structures of irradiated films do not change much and keep the local symmetry. Additionally, it is supposed that nano-crystallites aligned along with the original crystal axes[47]. In the case, the principal axes and gamma-ray has an angle of theta, peak intensity of doublet is expressed,

$$2 + 3\sin^2\theta : 3(1 + \cos^2\theta) \qquad \text{E.q. 3.1}$$

Providing that the principal axes align along <111> like crystalline Fe_3O_4[74], the angle theta is 54.7 deg for all <111> axes. In this case, the ratio is obtained to be 1/1. The fitting was performed based on the hypothesis and summarized in table 3.5. It is noted that the parameters of IS and D are almost the same. The area ratios of doublet of singlet about 3/7 and 5.7/4.3, respectively. These results can be explained by the number of Fe atoms on the B site, while the IS′s have larger amplitude compared with the reported values of Fe^{3+} [68]. The detailed discussion can be done after performing further experiments changing the angles between EFG and gamma-ray. It is also suggested that the ion irradiation influences on PMA for as-prepared films, which is supported by the value of A25/A34 (area ratio of 2nd and 5th peaks to 3rd and 4th peaks) to be 0.58/1; in the case of random orientation, it should be 3/1. After the irradiation of 1×10^{15} ions/cm^2, the ratio changed to 2.51/1, (see Table 3.3) suggesting that the PMA almost disappeared. The remnant magnetization for B series decreased with increase of dosage of Kr ions. It is speculated that the Co ferrite thin film first lost PMA and decrease magnetization with increasing of dosage of Kr ions. We also found the influence of ion irradiation on PMA. Figure 3.13 shows some parameters related to PMA such as A25/A34, coercive force (H_c), and M_r / M_s together with the normalized magnetization of Co ferrite (x=0.75, $Co_xFe_{3-x}O_4$)) against the Kr ion dosage. We confirmed that after the ion implantation the H_c of Co ferrite thin film first decrease. It is suggested that the magnetization of Co ferrite thin film first from perpendicular became to the in-plane. With the increasing of dosage of Kr ions, the magnetization of Co ferrite thin films decreased.

Table. 3.5 The fitting parameters of Fe_3O_4 with $4 \times 10^{15} ions/cm^2$ Kr ion irradiation and $CoFe_2O_4$ with 1×10^{16} $ions/cm^2$ Kr ion irradiation.

Sample	Subspectra	IS (mm/s)	QS (mm/s)	Area(%)
Fe_3O_4	Singlet	0.513	-	27
	Doublet	0.876	1.246	73
$CoFe_2O_4$	Singlet	0.478	-	57
	Doublet	0.876	1.614	43

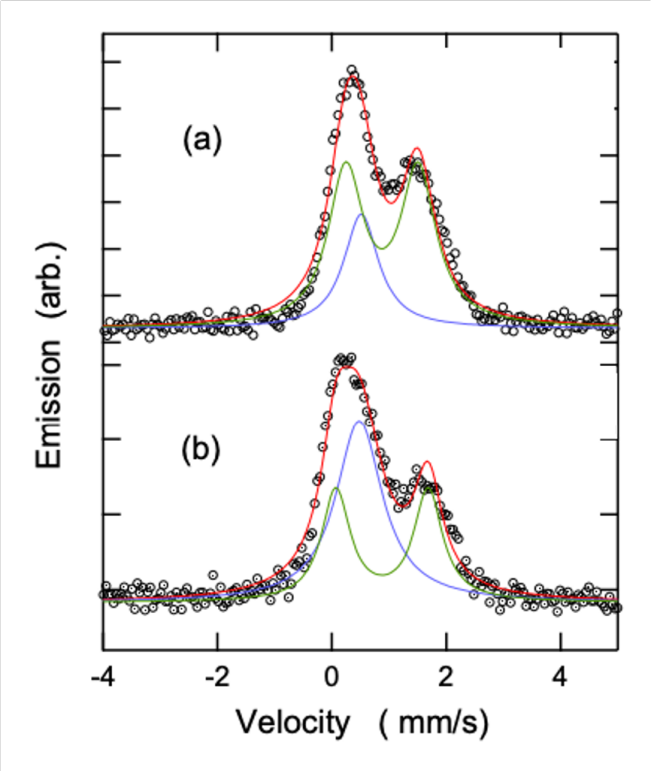

Fig. 3.12 The Mössbauer spectra for (a) Fe_3O_4 thin film with $4 \times 10^{15} ions/cm^2$ ion irradiation, (b) $CoFe_2O_4$ thin film with $1 \times 10^{16} ions/cm^2$ ion irradiation.

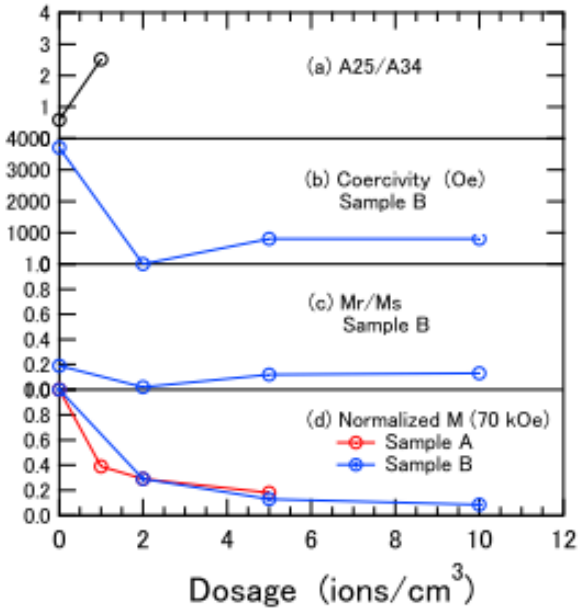

Fig. 3.13 The influence of Kr ion irradiation on magnetic properties, (a) A25/A34, (b) Coercivity, (c) M_r / M_s, and (d) magnetization at 70 kOe normalized with that of the sample before irradiation.

3.4 Structure analysis

The decreasing of magnetization of $CoFe_2O_4$ thin film and Fe_3O_4 thin film after ion irradiation has been investigated. The following parts give a set of structural measurement to explain the structural change via ion irradiation.

3.4.1 Electron diffraction pattern

To understand the structural change after ion irradiation, the electron diffraction pattern of selected area (thin film) has been carried out. The Figure 3.14 (a) shows the HRTEM image of $CoFe_2O_4$ thin film and (b) the select area of electron diffraction patterns of $CoFe_2O_4$ thin film. The Figure 3.15 (a) shows the HRTEM image of 1×10^{16} ions/cm^2 Kr ion-irradiated $CoFe_2O_4$ thin film and (b) the select area of electron diffraction patterns of ion-irradiated $CoFe_2O_4$ thin film. The electron diffraction patterns of $CoFe_2O_4$ thin film shows a typical spinel structure, and the electron diffraction patterns of 1×10^{16} ions/cm^2 Kr ion-irradiated $CoFe_2O_4$ thin film shows a rocksalt structure.

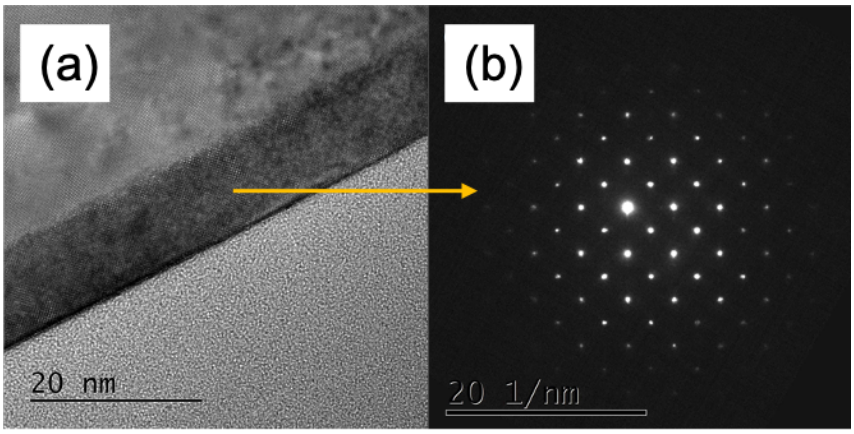

Fig. 3.14 The HRTEM image of $CoFe_2O_4$ thin film and the electron diffraction patterns of the selected area of $CoFe_2O_4$ thin film.

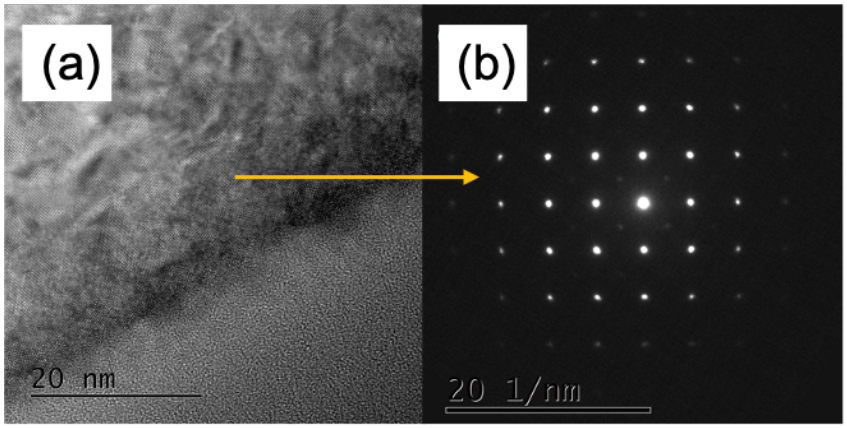

Fig. 3.15 The HRTEM image of ion-irradiated $CoFe_2O_4$ thin film and the electron diffraction patterns of the selected area of ion-irradiated $CoFe_2O_4$ thin film.

Similar results are obtained in Fe_3O_4 thin film. The Figure 3.16 (a) shows the HRTEM image of Fe_3O_4 thin film and (b) the select area of electron diffraction patterns of Fe_3O_4 thin film. The Figure 3.17 (a) shows the HRTEM image of 1×10^{16} ions/cm^2 Kr ion-irradiated Fe_3O_4 thin film and (b) the select area of electron diffraction patterns. The electron diffraction pattern of Fe_3O_4 thin film shows a typical spinel structure, and the electron diffraction pattern of 1×10^{16} ions/cm^2 Kr ion-irradiated Fe_3O_4 thin film shows a rocksalt structure.

Both electron diffraction patterns of $CoFe_2O_4$ thin film and Fe_3O_4 thin film before and after ion irradiation indicate that after Kr ion irradiation, topotactic structural transformation from spinel to rocksalt. Lattice constant of ion-irradiated thin film change to half of that $CoFe_2O_4$ thin film and Fe_3O_4 thin film, and crystal orientation has no change after Kr ion irradiation.

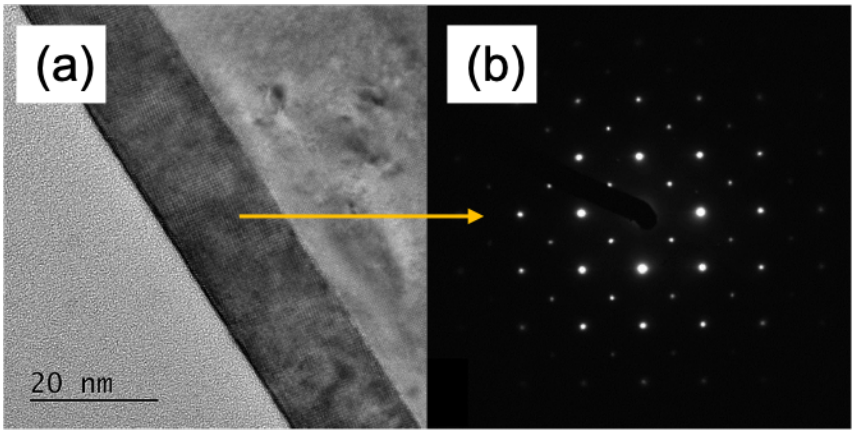

Fig. 3.16 The HRTEM image of Fe_3O_4 thin film and the electron diffraction patterns of the selected area of Fe_3O_4 thin film.

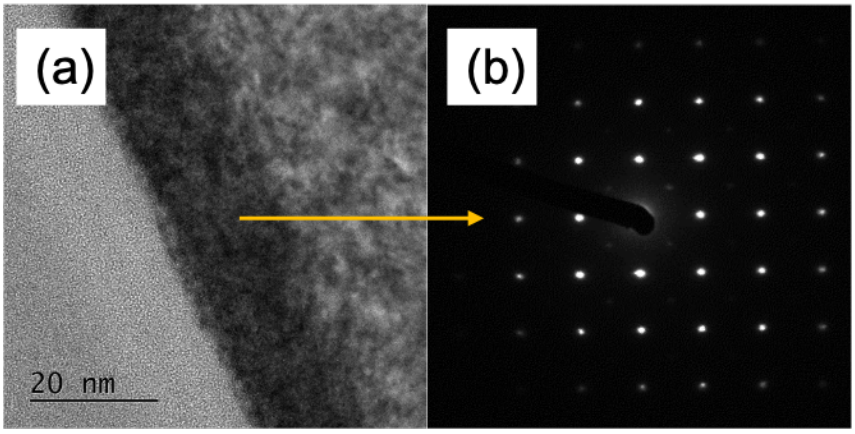

Fig. 3.17 The HRTEM image of ion-irradiated Fe_3O_4 thin film and the electron diffraction patterns of the selected area of ion-irradiated Fe_3O_4 thin film.

3.4.2 Reciprocal-lattice space map measurement

The reciprocal-lattice maps were carried out for $CoFe_2O_4$ thin film and $CoFe_2O_4$ thin film after ion irradiation. The figure 3.18 (a) and (b) show the $(h\ 1\ \ell)$ reciprocal-lattice maps of as-grown 11 nm thick $CoFe_2O_4$ thin film on MgO (0 0 1) and 1×10^{16} ions/cm^2 Kr ion-irradiated thin film, respectively. Hereafter, the reciprocal-lattice unit of MgO is used as the unit length for the reciprocal-lattice maps as well as for the Miller indices, unless explicitly stated otherwise. In Fig. 3.17(a), the Bragg reflection of $(2\ 2\ 2)$ from $CoFe_2O_4$ thin film and Laue fringes arising along the $[1\ 1\ \ell^*]$ line prove that the film coherently grew on MgO (0 0 1) with high crystallinity. Shift of the reflection from (2 2 2) to (2 2 2.05) indicates that the unit cells of the $CoFe_2O_4$ are tetragonally distorted because of lattice mismatch. On the other hand, non-existent Laue fringes in Fig. 3.17 (b) of the ion-irradiated thin film indicates that the $CoFe_2O_4$ thin film was destroyed after ion irradiation. Instead, a broad peak appears around (0.99 1 0.99), which is close to that for MgO (1 1 1).

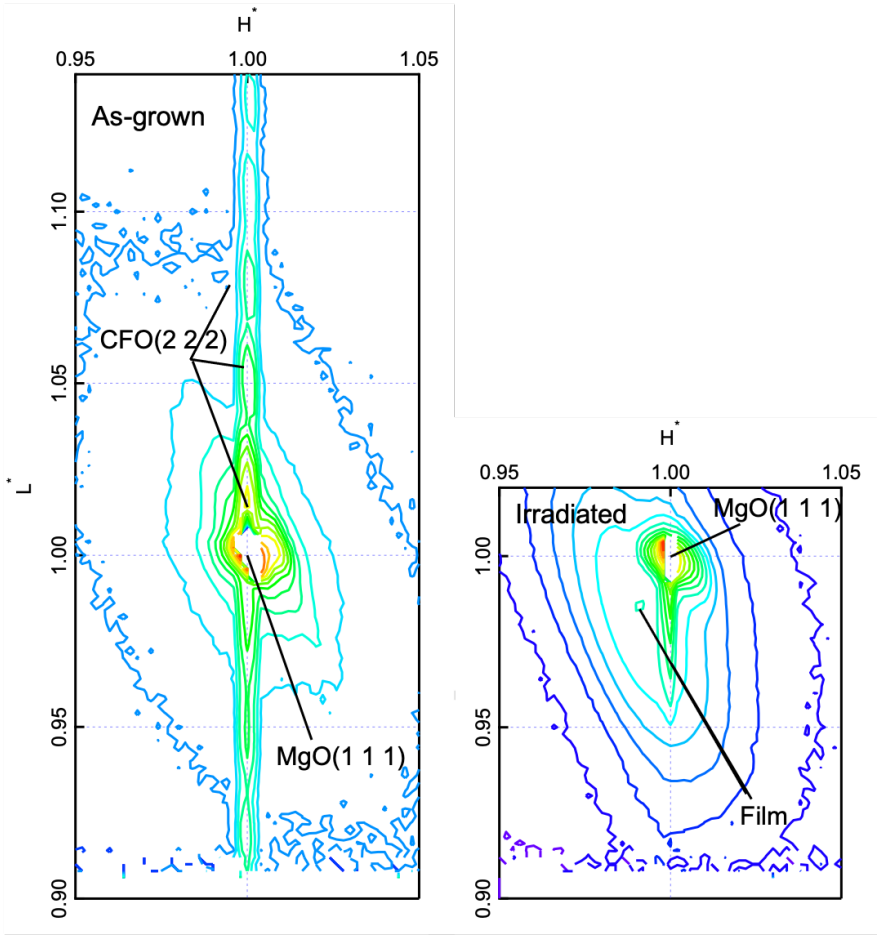

Fig. 3.18 (a) Reciprocal-lattice map on $(H\ 1\ L)^*$ of an as-grown Fe_3O_4 thin film without irradiation and (b) that of the thin film after ion irradiation, where the reciprocal lattice unit of MgO was used as the unit length. The Bragg reflection was expected to appear from the Fe_3O_4 (2 2 2). Bragg reflection from the Fe_3O_4 thin film disappears; instead, the (1 1 1) plane appears in the ion-irradiated thin film.

The reciprocal-lattice maps were carried out for Fe_3O_4 thin film and Fe_3O_4 thin film after ion irradiation. The figure 3.19 (a) and (b) show the $(h\ 1\ \ell)$ reciprocal-lattice map of as-grown 16 nm thick Fe_3O_4 thin film on MgO (0 0 1) and 5×10^{15} ions/cm^2 Kr ion-irradiated thin film, respectively. The same to reciprocal-lattice maps of $CoFe_2O_4$ thin film, the reciprocal-lattice unit of MgO is used as the unit length for the reciprocal-lattice maps as well as for the Miller indices. In Fig. 3.19 (a), the Bragg reflection of Fe_3O_4 (2 2 2) and Laue fringes arising along the $[1\ 1\ \ell^*]$ line means that the film grew on MgO (0 0 1) with high coherency. The main reflection of Fe_3O_4 (2 2 2) is found at around $(1\ 1\ 1.03)^*$ indicating that the unit cells of the Fe_3O_4 are tetragonally distorted demonstrating that the film is coherently grown with the in-plane lattice parameter of MgO. On the other hand, non-existent Laue fringes in Fig. 3.19 (b) of the ion-irradiated thin film indicates that the Fe_3O_4 thin film was destroyed after ion irradiation. Instead, a broad peak appears around $(0.99\ 1\ 0.99)^*$, which is close to that for MgO (1 1 1). The thin film changes from fully strained in as-grown states to relaxed after ion irradiation.

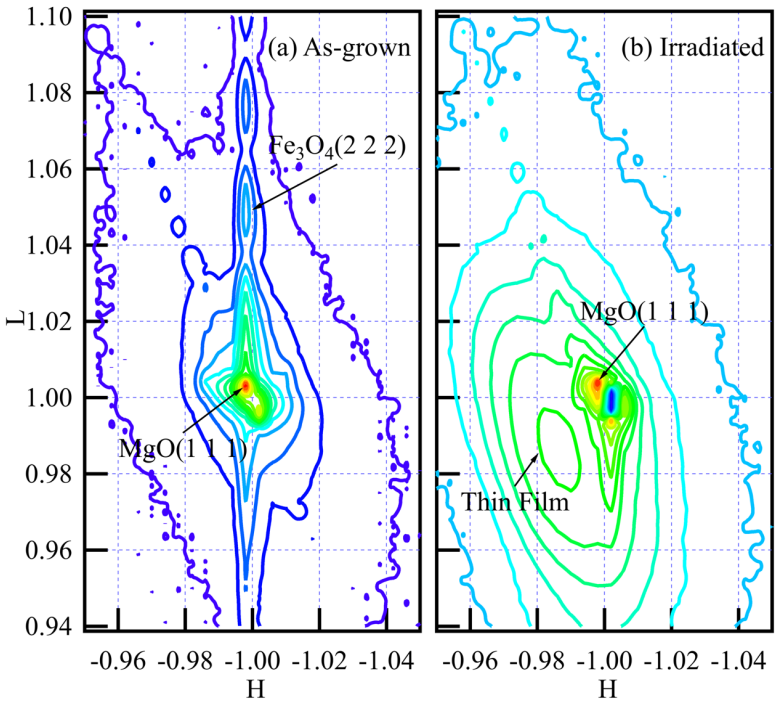

Fig. 3.19 (a) Reciprocal-lattice map on $(H\ 1\ L)^*$ of an as-grown Fe_3O_4 thin film without irradiation and (b) that of the thin film after ion irradiation, where the reciprocal lattice unit of MgO was used as the unit length. The Bragg reflection was expected to appear from the Fe_3O_4 (2 2 2). Bragg reflection from the Fe_3O_4 thin film disappears; instead, the (1 1 1) plane appears in the ion-irradiated thin film.

3.4.3 Rocking curve measurement

Both the as-grown $CoFe_2O_4$ thin film and Fe_3O_4 thin film showed a set of specific reflections that are consistent with those of a cubic spinel ($Fd\bar{3}m$). As an example, rocking curves for Fe_3O_4 (1 1 1) and Fe_3O_4 (1 1 3) of the thin film are shown in Figures 3.20 (a) and (b), respectively. Note that there is no Bragg peak at the vicinity of MgO for either Fe_3O_4 (1 1 1) or Fe_3O_4 (1 1 3). That means the peaks which observed around (1 1 1) or (1 1 3) should belong spinel structure of Fe_3O_4 thin film. Before ion irradiation, the peak of Fe_3O_4 (1 1 1) and Fe_3O_4 (1 1 3) were observed as the spinel structure. After ion irradiation, Fe_3O_4 (1 1 1) and Fe_3O_4 (1 1 3) of the spinel structure completely disappear. This result indicates that the spinel structure was destroyed after ion irradiation and transformed to another structure. The lattice constant changed to approximately half that of the Fe_3O_4 thin film. For $CoFe_2O_4$ thin film, the rocking curve for $CoFe_2O_4$ (1 1 1) and $CoFe_2O_4$ (1 1 3) before and after ion irradiation also has been measured. The rocking curve of reflection (1 1 1) and (1 1 3) for spinel structure of $CoFe_2O_4$ thin film is shown in the figure 3.21 and the figure 3.22. Both the reflection (1 1 1) and (1 1 3) of spinel structure disappeared after ion irradiation. The results indicate spinel structure was destroyed via Kr ion irradiation both in Fe_3O_4 thin film and $CoFe_2O_4$ thin film.

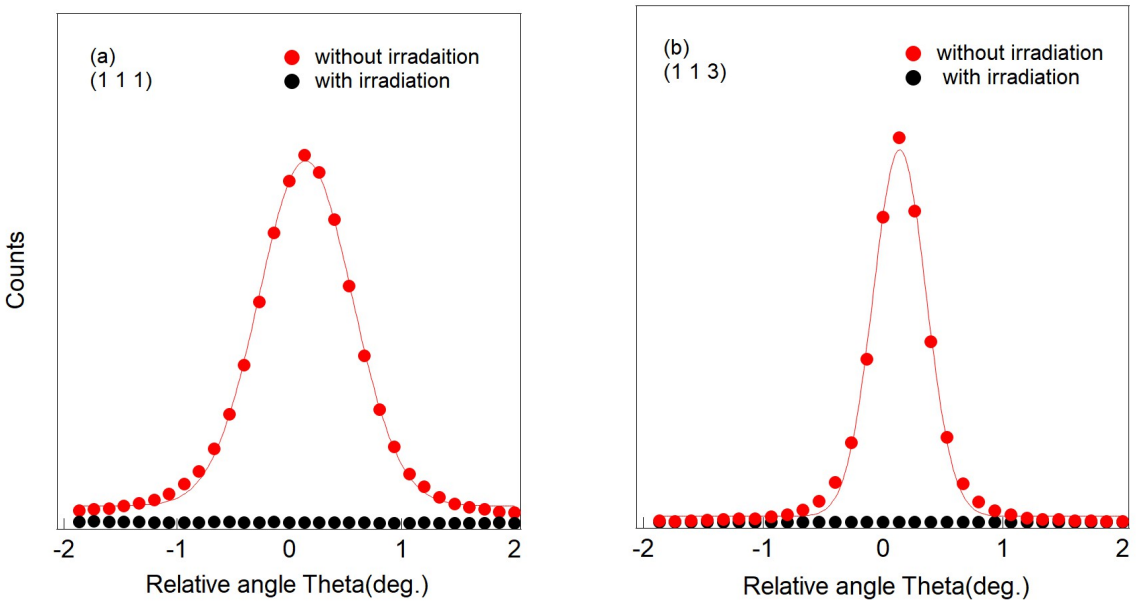

Fig. 3.20 Rocking curves of (a) Fe_3O_4 (1 1 1) and (b) Fe_3O_4 (1 1 3) of the as-grown and ion-irradiated films. Red circles represent theta-scans for the as-grown Fe_3O_4 thin film and black circles represent that for the ion-irradiated film.

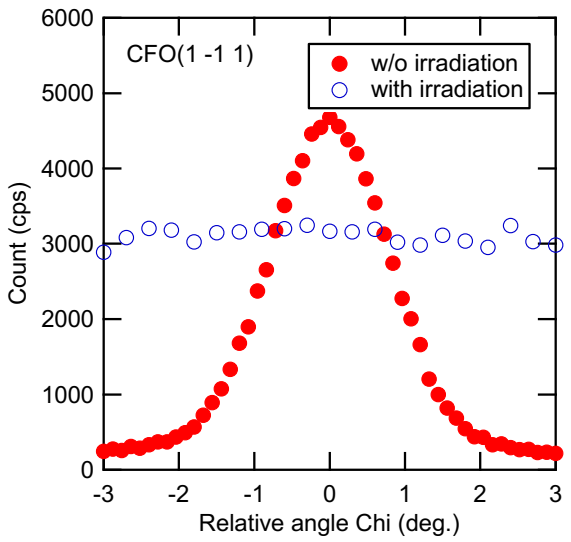

Fig. 3.21 Rocking curves of $CoFe_2O_4$ (1 1 1).

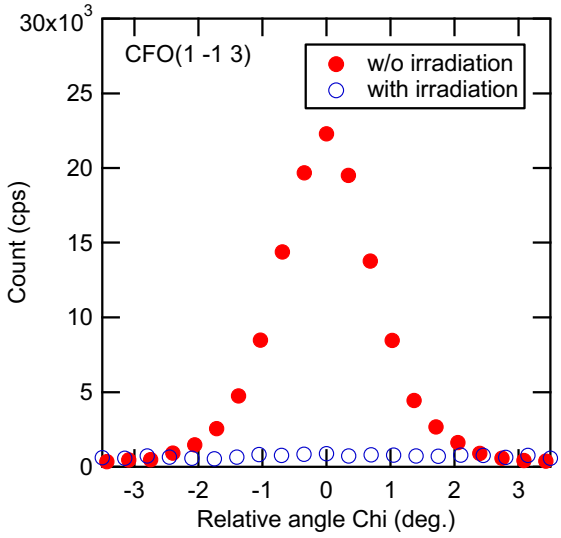

Fig. 3.22 Rocking curves of $CoFe_2O_4$ (1 1 3).

3.4.4 STEM and RBS measurement

Comparing the STEM image, we find an interesting conclusion that the thickness of ion-irradiated thin film remained as the as-grown one. The figure 3.23 shows annular dark-field scanning transmission electron microscopy (ADF-STEM) morphologies of the (a) as-grown and (b) ion-irradiated $CoFe_2O_4$ thin films. In the STEM images of Fig 3.23 (a) and (b), the horizontal direction corresponds to MgO [0 0 1] parallel to the growth direction and the vertical direction corresponds to both MgO [1 0 0]. The thickness of the as-grown thin film is shown in Fig. 3.23 (a). Comparing with Fig. 3.23 (b), the ion-irradiated thin film is seen to retain thickness of 11 nm. It is obvious that the ion irradiation has no effect on the thickness of $CoFe_2O_4$ film.

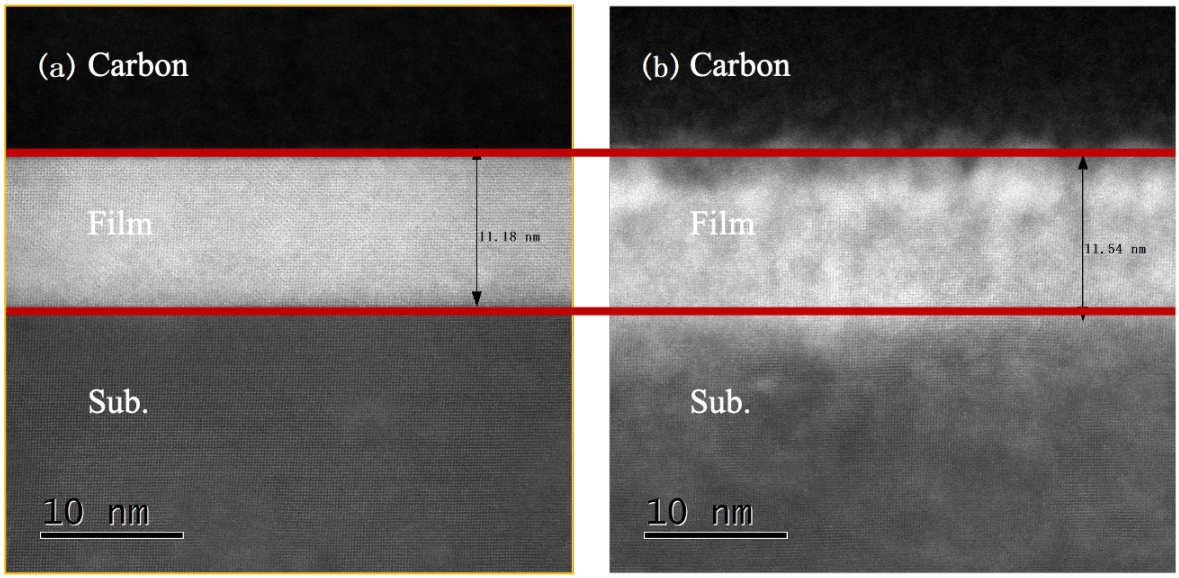

Fig 3.23 annular dark-field scanning transmission electron microscopy (ADF-STEM) morphologies of the (a) as-grown and (b) ion-irradiated $CoFe_2O_4$ thin films.

The thickness of ion-irradiated Fe_3O_4 thin film has no change to Fe_3O_4 thin film was also confirmed through the STEM images of Fe_3O_4 thin film before and after ion irradiation. The figure 3.24 shows annular dark-field scanning transmission electron microscopy (ADF-STEM) morphologies of the (a) as-grown and (b) ion-irradiated Fe_3O_4 thin films. The crystal orientation is corresponding to MgO substrate, which is same to STEM images of $CoFe_2O_4$ thin film, in the STEM images of Fig 3.24 (a) and (b), the horizontal direction corresponds to MgO [0 0 1] parallel to the growth direction and the vertical direction corresponds to both MgO [1 0 0]. Comparing to the thickness of the as-grown thin film which is shown in Fig. 3.24 (a), the ion-irradiated thin film is seen to retain thickness of 16 nm. The results indicate that Kr ion irradiation has no effect on the thickness of both Fe_3O_4 film and $CoFe_2O_4$ film.

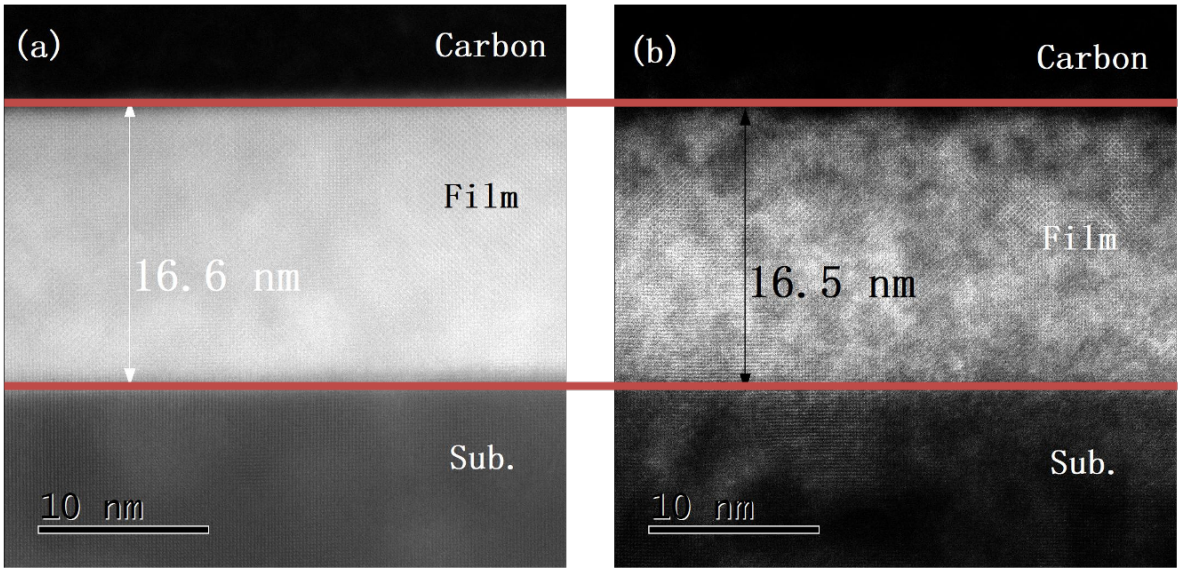

Fig. 3.24 annular dark-field scanning transmission electron microscopy (ADF-STEM) morphologies of the (a) as-grown and (b) ion-irradiated Fe_3O_4 thin films.

For the further understanding of structural change of spinel structure, Fe_3O_4 thin film is forced on, because only Fe and O are contained in Fe_3O_4 thin film, and easy to understand the mechanism of structural change of ferrite oxide with spinel structure via ion irradiation.

The RBS spectra for Fe_3O_4 thin film and ion-irradiated thin film are shown in the figure 3.25. Both the total amount and the distribution of Fe in the iron-oxide film are not changed by the ion irradiation process. By taking account the above two experimental facts, i.e., the unchanged film thickness and unchanged Fe distribution, we can conclude that the composition ratio between Fe and O in the irradiated thin film remains as 3:4.

Here, we assume that the situation which the composition ratio between Fe and O in the ion-irradiated thin film has changed after ion irradiation, that means O distribution must be changed as the experimental fact of RBS has confirmed that the Fe distribution has no change after ion irradiation.

There are two possibilities, O distribution increases, on the other hand, decreases. Owing to the ionic volume of oxygen is much larger than that of iron, the total film thickness must be much easier influenced by the change of O distribution. If oxygen go into thin film, the total film thickness should increase significantly. On the contrary, if oxygen atoms are knocked off by the irradiation, the total film thickness must be obviously reduced. Both possibilities are opposite to the TEM results that the total film thickness remains before and after ion irradiation. The total film thickness remaining the same means that local reorder of atomic positions occurs as a result of the ion irradiation. This indicates that the observed rocksalt-like structure originates from cation-site defects, i.e., topotactic transformation from spinel structure to rocksalt-like structure with Fe cation-site defects and Fe and O remain as Fe_3O_4 in ion-irradiated thin film.

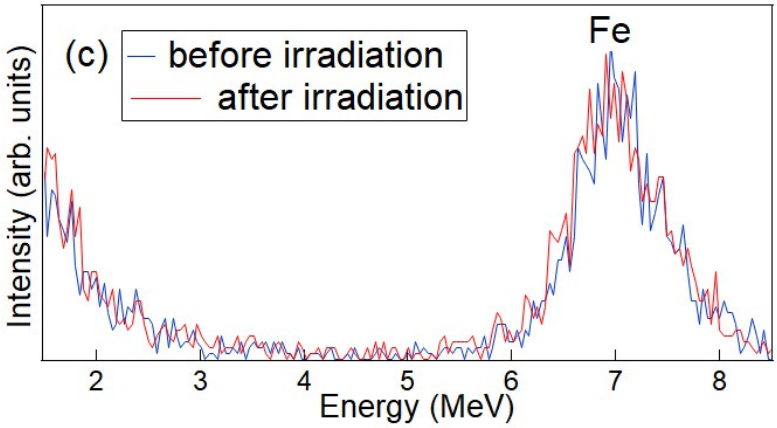

Fig. 3.25 The RBS spectrum of Fe_3O_4 thin film before and after ion irradiation.

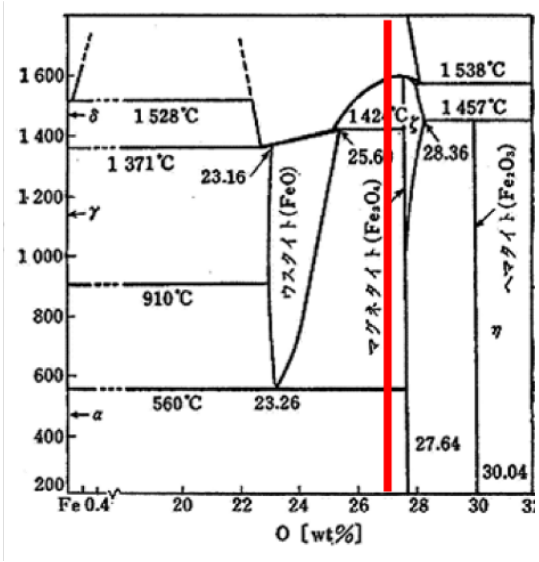

Fig. 3.26 The phase diagram of Fe-O[75].

For understanding crystal structure of ion-irradiated thin film, O onion remain original position of face-center cubic structure is supposed to consider the structural change after ion irradiation, as the ionic volume of oxygen is much larger than that of iron. On the other hand, Fe cations occupy either or both in tetrahedral site and octahedral site. As we all know, Fe_3O_4 is spinel structure with space group $Fd\bar{3}m$ (No.227), i.e., Fe cations occupy in $8a$ which form tetrahedral site with O onions, at the same time, Fe cations occupy in $16d$ which form octahedral site with O onions. Considering of ion-irradiated thin film, we assume that ion-irradiated thin film remains space group $Fd\bar{3}m$ (No.227), thus Fe cations reoccupy in $8a$, $8b$ (tetrahedral site) and $16c$, $16d$ (octahedral site), randomly, then we suppose that x_{8a}, x_{8b}, x_{16c}, x_{16d} represent the occupation of Fe ions in $8a$, $8b$, $16c$ and $16d$, respectively.

Therefore

$$x_{8a} + x_{8b} + x_{16c} + x_{16d} = 24,$$

which is consistent with Fe cations in Fe_3O_4, as we found no sign of local composition change by ion irradiation. In order to understand the distribution of Fe cations in ion-irradiated thin film, Structure factor calculations were carried out of several reflection, which is revealed in Table 3.5.

According to Structure factor for reflection $(1\,1\,1)$ and $(1\,1\,3)$, which both are reflections from spinel structure,

For Structure factor of reflection $(1\,1\,1)$ of spinel structure, $S_{(1\,1\,1)_{\mathrm{SP}}}$,

$$S_{8a(1\,1\,1)_{\mathrm{SP}}} = f_{\mathrm{Fe}} \cdot (-4\sqrt{2}),\ S_{8b(1\,1\,1)_{\mathrm{SP}}} = f_{\mathrm{Fe}} \cdot 4\sqrt{2},$$

$$S_{16c(1\,1\,1)_{\mathrm{SP}}} = f_{\mathrm{Fe}} \cdot (-8),\ S_{16d(1\,1\,1)_{\mathrm{SP}}} = f_{\mathrm{Fe}} \cdot 8,$$

$$S_{\mathrm{O}(1\,1\,1)_{\mathrm{SP}}} = 0,$$

$$S_{(1\,1\,1)_{\mathrm{SP}}} = S_{8a(1\,1\,1)_{\mathrm{SP}}} \cdot x_{8a} + S_{8b(1\,1\,1)_{\mathrm{SP}}} \cdot x_{8b} + S_{16c(1\,1\,1)_{\mathrm{SP}}} \cdot x_{16c} + S_{16d(1\,1\,1)_{\mathrm{SP}}} \cdot x_{16d} + S_{\mathrm{O}(1\,1\,1)_{\mathrm{SP}}},$$

$$= f_{\mathrm{Fe}} \cdot \left(-4\sqrt{2}\right) \cdot x_{8a} + f_{\mathrm{Fe}} \cdot 4\sqrt{2} \cdot x_{8b} + f_{\mathrm{Fe}} \cdot (-8) \cdot x_{16c} + f_{\mathrm{Fe}} \cdot 8 \cdot x_{16d}$$

Here, f_{Fe} represents scattering factor.

For Structure factor of reflection $(1\ 1\ 3)$ of spinel structure, $S_{(1\ 1\ 3)_{\mathrm{SP}}}$,

$$S_{8a(1\ 1\ 3)_{\mathrm{SP}}} = f_{\mathrm{Fe}} \cdot (-4\sqrt{2}),\ S_{8b(1\ 1\ 3)_{\mathrm{SP}}} = f_{\mathrm{Fe}} \cdot 4\sqrt{2},$$

$$S_{16c(1\ 1\ 3)_{\mathrm{SP}}} = f_{\mathrm{Fe}} \cdot 8,\ S_{16d(1\ 1\ 3)_{\mathrm{SP}}} = f_{\mathrm{Fe}} \cdot (-8),$$

$$S_{\mathrm{O}(1\ 1\ 3)_{\mathrm{SP}}} = 0,$$

$$S_{(1\ 1\ 3)_{\mathrm{SP}}} = S_{8a(1\ 1\ 3)_{\mathrm{SP}}} \cdot x_{8a} + S_{8b(1\ 1\ 3)_{\mathrm{SP}}} \cdot x_{8b} + S_{16c(1\ 1\ 3)_{\mathrm{SP}}} \cdot x_{16c} + S_{16d(1\ 1\ 3)_{\mathrm{SP}}} \cdot x_{16d} + S_{\mathrm{O}(1\ 1\ 3)_{\mathrm{SP}}},$$

$$= f_{\mathrm{Fe}} \cdot \left(-4\sqrt{2}\right) \cdot x_{8a} + f_{\mathrm{Fe}} \cdot 4\sqrt{2} \cdot x_{8b} + f_{\mathrm{Fe}} \cdot 8 \cdot x_{16c} + f_{\mathrm{Fe}} \cdot (-8) \cdot x_{16d}$$

From the Structure factor for reflection $(1\ 1\ 1)$ of spinel structure, $S_{(1\ 1\ 1)_{\mathrm{SP}}}$, and Structure factor for reflection $(1\ 1\ 3)$ of spinel structure, $S_{(1\ 1\ 3)_{\mathrm{SP}}}$, we found that as long as

$$x_{8a} = x_{8b} \text{ and } x_{16c} = x_{16d},$$

we would get,

$$S_{(1\ 1\ 1)_{\mathrm{SP}}} = 0 \text{ and } S_{(1\ 1\ 3)_{\mathrm{SP}}} = 0,$$

which is consistent with experiment results, given in Fig. 3.19 (a) and (b).

That means after ion irradiation, Fe cations reoccupy in tetrahedral site, $8a$, $8b$, equally, as well as octahedral site $16c$, $16d$, equally, which is consistent with another cubic space group of $Pn\bar{3}$m (No.224).

We found that there are two possibilities which satisfy $S_{(1\ 1\ 1)_{\mathrm{SP}}} = 0$ and $S_{(1\ 1\ 3)_{\mathrm{SP}}} = 0$.

1. $x_{8a} = x_{8b} = 0$ and $x_{16c} = x_{16d}$,

In this situation, Fe cations occupy in $8a$ sites totally move to $16c$ sites or $16d$ sites after ion irradiation, and Fe cations occupy in $16c$ sites and $16d$ sites equally. The structure transforms to rocksalt structure with cation-site vacancies. The structure schematic of rocksalt structure with cation-site vacancies is shown in the Figure 3.27.

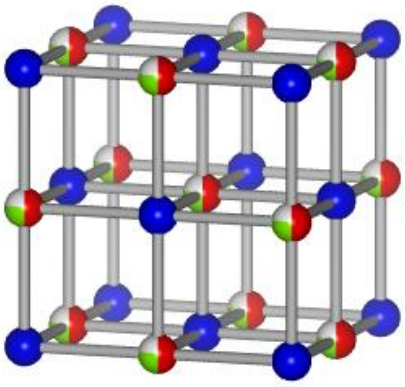

Fig. 3.27 The structure schematic of rocksalt structure with cation-site vacancies

2. $x_{8a} = x_{8b} \neq 0$ and $x_{16c} = x_{16d}$,

In this situation, Fe cations occupy in $8a$ sites partly move to $16c$ sites or $16d$ sites after ion irradiation, some Fe cations move to $8b$ sites also some Fe cations remain in $8a$ sites. Occupation in $8a$ sites is equal to that in in $8b$ sites. The structure transforms to rocksalt-like structure with Fe occupy in $8a$ sites and $8b$

sites. The structure schematic of rocksalt-like structure with Fe occupy in $8a$ sites and $8b$ sites is shown in the Figure 3.27.

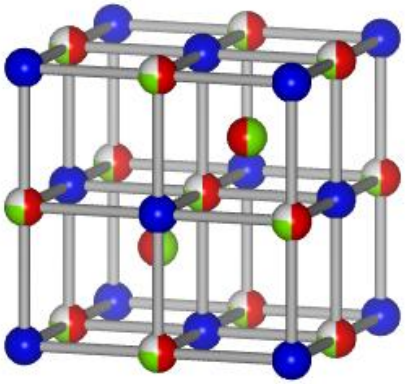

Fig. 3.28 The structure schematic of rocksalt-like structure with Fe occupy in $8a$ sites and $8b$ sites

For further understanding the coordination condition of Fe cations in tetrahedral site ($8a$, $8b$), a reflection which can distinguish whether there are Fe cations occupy in tetrahedral site ($8a$, $8b$) or not.

According to calculation result of Structure factor of reflection $(0\ 2\ 2)$, $S_{(0\ 2\ 2)_{\mathrm{SP}}}$,

$$S_{8a(0\ 2\ 2)_{\mathrm{SP}}} = f_{\mathrm{Fe}} \cdot (-8),\ S_{8b(0\ 2\ 2)_{\mathrm{SP}}} = f_{\mathrm{Fe}} \cdot (-8),$$

$$S_{16c(0\ 2\ 2)_{\mathrm{SP}}} = f_{\mathrm{Fe}} \cdot 0 = 0,\ S_{16d(0\ 2\ 2)_{\mathrm{SP}}} = f_{\mathrm{Fe}} \cdot 0 = 0,$$

$$S_{\mathrm{O}(0\ 2\ 2)_{\mathrm{SP}}} = 0,$$

$$S_{(0\ 2\ 2)_{\mathrm{SP}}} = S_{8a(1\ 1\ 3)_{\mathrm{SP}}} \cdot x_{8a} + S_{8b(1\ 1\ 3)_{\mathrm{SP}}} \cdot x_{8b} + S_{16c(1\ 1\ 3)_{\mathrm{SP}}} \cdot x_{16c} + S_{16d(1\ 1\ 3)_{\mathrm{SP}}} \cdot x_{16d} + S_{\mathrm{O}(1\ 1\ 3)_{\mathrm{SP}}},$$

$$= f_{\mathrm{Fe}} \cdot (-8) \cdot x_{8a} + f_{\mathrm{Fe}} \cdot (-8) \cdot x_{8b}$$

we found that $S(0\ 2\ 2)_{\mathrm{SP}}$ is only contingent on whether Fe cations occupy in tetrahedral site ($8a$, $8b$) and has no relations with whether Fe cations occupy in octahedral site ($16c$, $16d$). which is revealed in table. 3.5 . Reflection of $(0\ 2\ 2)$ of spinel structure also has been carried out, which is shown in the figure 3.29.

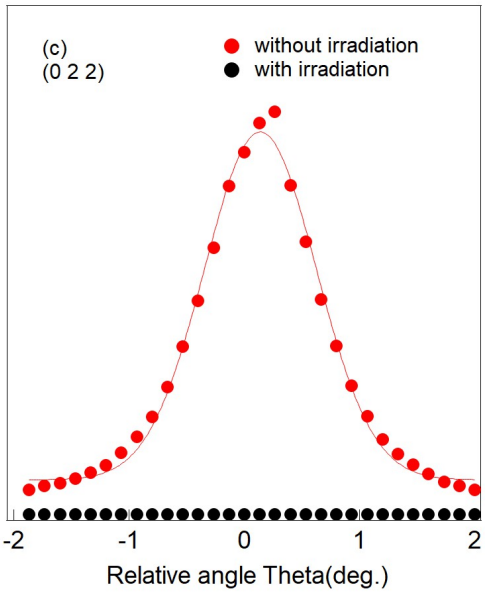

Fig. 3.29 Rocking curves of Fe_3O_4 $(0\ 2\ 2)$ of the as-grown and ion-irradiated films. Red circles represent theta-scans for the as-grown Fe_3O_4 thin film and black circles represent that for the ion-irradiated film.

Combining to measure of reflection of $(0\ 2\ 2)$ of spinel structure, i.e., reflection $(0\ 2\ 2)_{SP}$ disappear after ion irradiation, that means $S_{(0\ 2\ 2)_{SP}} = 0$. As a result, $x_{8a} = x_{8b} = 0$, Fe cations only occupy in octahedral site ($16c$, $16d$), without any occupation in tetrahedral site ($8a$ and $8b$). As Fe cations do not occupy in tetrahedral site in ion-irradiated thin film, further higher symmetry space group $Fm\bar{3}m$ (No.224) is considered to satisfy ion-irradiated film. For ion-irradiated thin film with $Fm\bar{3}m$, if there are Fe cations occupy in tetrahedral site, $(0\ 1\ 1)_{RS}$ or $(0\ 2\ 2)_{SP}$ should be observed. However, this is on the contrary to experiment result. As a result, after ion irradiation, Fe cations in $8a$ site of spinel structure totally move to octahedral site, equal coordination in $16c$ and $16d$ site, which formed rocksalt structure of space group $Fm\bar{3}m$ with cation site vacancy. In other words, Fe_3O_4 thin film transform to wüstite (Fe_xO), after ion irradiation. Because after ion irradiation, composition of Fe maintains as Fe_3O_4 thin film, thus x=0.75, i.e. $Fe_{0.75}O$. According to the phase diagram of Fe-O, shown in the figure 3.26, for the wüstite (Fe_xO), the wight percentage of oxygen is from 23.16% to 25.60%, i.e. wüstite (Fe_xO) x=0.83~0.95. That means our ion-irradiated thin film $Fe_{0.75}O$ with more Fe cations vacancies than normal wüstite as a metastable phase.

Table. 3.5 Calculation for Structure factor $S_{(h\,k\,l)}$ of Fe_3O_4.

Wyckoff Position of $\boldsymbol{Fd\bar{3}m(227)}$	**(1 1 1)**	**(1 1 3)**	**(0 2 2)**
8a	$(-4\sqrt{2})\cdot f_{Fe}$	$(-4\sqrt{2})\cdot f_{Fe}$	-8· f_{Fe}
8b	$(4\sqrt{2})\cdot f_{Fe}$	$(4\sqrt{2})\cdot f_{Fe}$	-8· f_{Fe}
16c	-8· f_{Fe}	8· f_{Fe}	0· f_{Fe}
16d	8· f_{Fe}	-8· f_{Fe}	0· f_{Fe}
32e	0· f_O	0· f_O	0· f_O
$\boldsymbol{S_{(h\,k\,l)}}$	0	0	0
Exp. observed after irradiation	No reflection	No reflection	No reflection

4. Conclusion

This study covered a comprehensive study process that effect of ion irradiation on spinel ferrite oxide thin film, including the fabrication, experimental characterization, magnetism analysis and structural analysis. These bring us new insights and for future work to help us better understand the material both in spinel ferrite oxide and ion irradiation aspect.

The typical spinel ferrite $CoFe_2O_4$ and Fe_3O_4 were investigated for epitaxial grown thin film on MgO (0 0 1) substrate. The magnetization of $CoFe_2O_4$ and Fe_3O_4 thin films can be controlled by different dese of ion irradiation, the saturation magnetization of both of $CoFe_2O_4$ and Fe_3O_4 thin films decrease with the increasing of dose of ion irradiation, finally decrease to 0 when dose of ion reaches a certain level. This result is confirmed by hysteresis loops of various dose ion-irradiated thin films. The magnetism of $CoFe_2O_4$ and Fe_3O_4 thin films are from ferro-magnetic change to para-magnetic after ion irradiation, the component of para-magnetic parts was proportional to the increase of ion dose, which is revealed by Mössbauer study.

In the ion-irradiated $CoFe_2O_4$ and Fe_3O_4 thin films, specific diffraction spots for spinel structure from XRD study were not observed. That means the spinel structure is destroyed via ion irradiation and transform to rocksalt type ($Fm\bar{3}m$). Lattice constant of ion-irradiated $CoFe_2O_4$ and Fe_3O_4 thin films change to half of that $CoFe_2O_4$ and Fe_3O_4 thin films, respectively. For further structure study for ion-irradiated thin film. The Fe_3O_4 thin film was paid attention to as only Fe and O contained. In the ion-irradiated Fe_3O_4 thin film, Fe : O remained 3 :4, also keep epitaxial relationship of Fe_3O_4 thin film. Fe_3O_4 thin film transform to wüstite (Fe_xO), after ion irradiation, x=0.75, i.e., $Fe_{0.75}O$, which form a metastable phase. According to the phase diagram of Fe-O[75], for wüstite (Fe_xO), x is from 0.83~0.95, which means in this study, $Fe_{0.75}O$ with a rocksalt structure is a new phase for wüstite. Ion irradiation as an effective method for controlling the saturation magnetization of spinel ferrite oxide, the change of saturation magnetization is due to the structural change after ion irradiation. In other words, ion irradiation can thus be a powerful tool for controlling the structure of the film without sacrificing the epitaxial nature of $CoFe_2o_4$ and Fe_3O_4, and then have influenced on other properties of the material.

Ion irradiation gives us an effective method to modify the structure of the material, thereby can control the propertied of materials. Understanding the effect of ion irradiation and then predicting ion irradiation effect even damage in materials is crucial in future work in the study of materials.

In this study, we focused on the final structural change of spinel ferrite oxide via ion irradiation. When ion dose reaches a certain level, structure of spinel ferrite oxide totally changes to rocksalt. However, the structural change at a middle level has not been carried out. For better understanding the ion irradiation effect on spinel ferrite, the intermediate status of ion-irradiated thin film is considered.

Besides, in the measurement of electron diffraction pattern, weak diffraction from spinel structure was observed, which is inconsistent with the XRD results. We performed SAED measurement in a short time followed by STEM observations, which resulted in continuous electron irradiation. The electron beam irradiation causes the structural transformation from the metastable rocksalt structure into a

thermodynamically stable spinel structure due to local heating by the electron beam[76]. This gives us a new suspect that if annealing process can do effect to the ion-irradiated thin film. The annealing process after ion irradiation could revert the rocksalt structure to spinel structure of ion-irradiated thin film or change to another metastable phase.

Appendix

A. According to the SRIM, the simulation of ion irradiation

A.1 SRIM

SRIM is a kind of simulation software for the process of the ion implantation, which was developed by International Business Machines Corporation (IBM). With this software, for example the information about the stopping energy of electron, the stopping energy of nuclear and loss of the energy can be obtained during the process of ion implantation. The figure A.1 shows the interface of the SRIM.

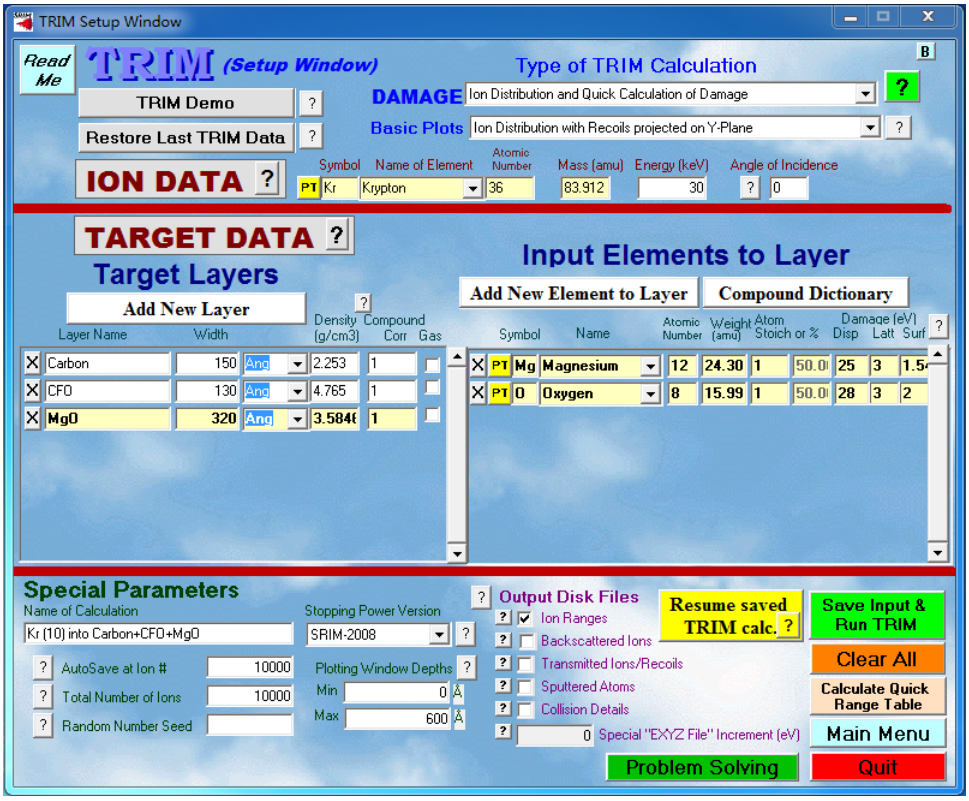

Fig A.1 Interface of the SRIM.

A.2 the condition of simulation of ion implantation

The condition of the simulation of ion implantation was used as the same condition for reality. The table A.1 provides the condition of simulation. The parameters for different condition can change though the interface of the software. The source of ion is Krypton, the accelerate voltage of Kr ions is from10kV to 30kV, and the number of ions for simulation is set at 10000 ions.

Table A.1 Condition of SRIM simulation

	thickness	density
Carbon protect	8-15 nm	2.253 g/cm^3
$CoFe_2O_4$	13 nm	4.765 g/cm^3
MgO	—	3.584 g/cm^3

A.3 Range of Kr ions

The range of Kr ions from the simulation is indicated in figure A.2 (a) to A.2 (i). According to the ranges of ions, the effect of Kr ion implantation is cleared understanded.

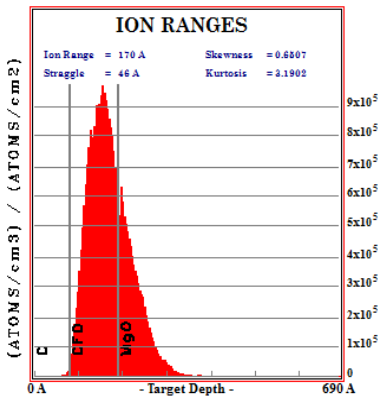

(a) Carbon 8nm

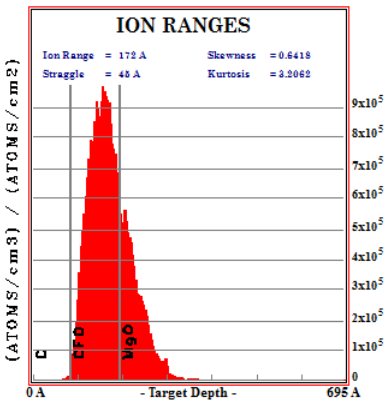

(b) Carbon 8.5nm

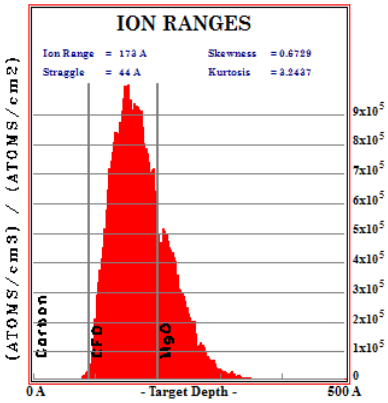

(c) Carbon 9nm

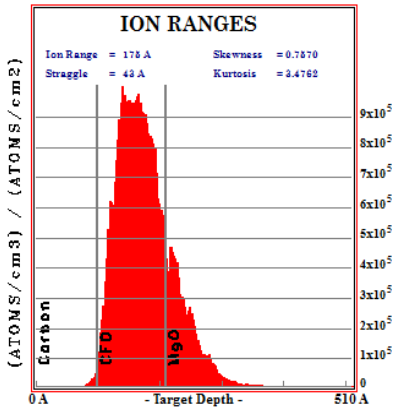

(d) Carbon 10nm

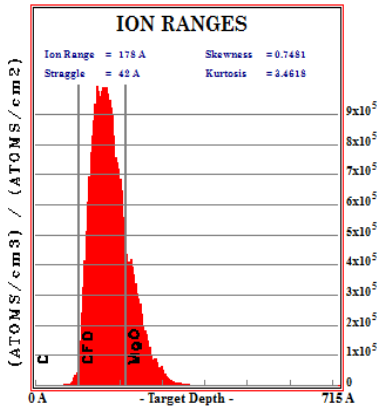

(e) Carbon 10.5nm

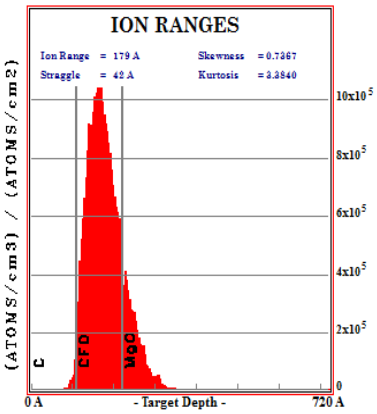

(f) Carbon 11nm

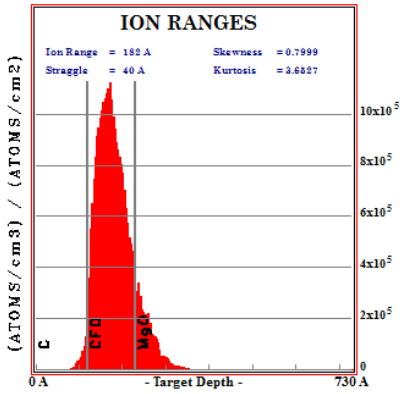

(g) Carbon 12nm

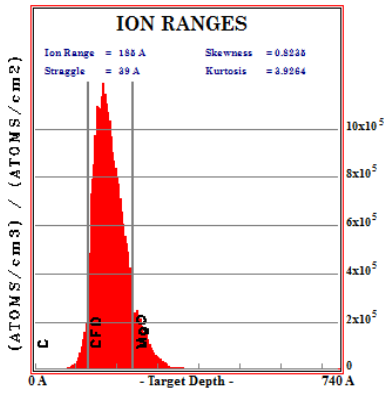

(h) Carbon 13nm

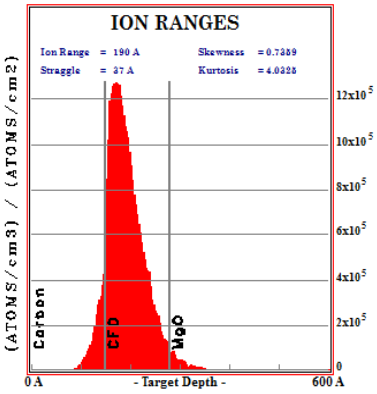

(i) Carbon 15nm

Fig A.2 Ranges of ion

A.4 XY longitudinal of simulation

The XY longitudinal figure shows the moving tracks and the stopping positions of the Kr ions, shown in the figure A.3 (a) to A.3 (b). The white parts in the figure are made up by moving tracks of Kr ions, the red points in the figure are the stopping positions.

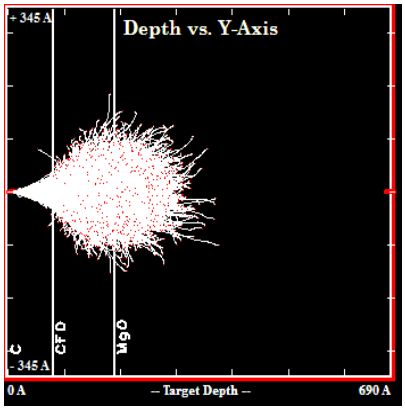

(a) Carbon 8nm

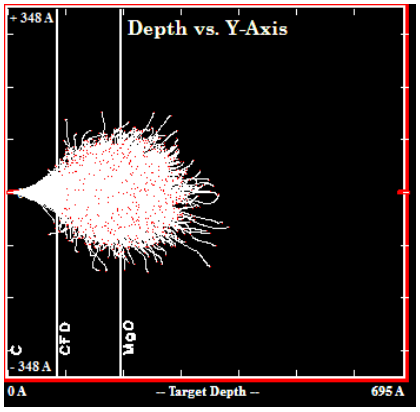

(b) Carbon 8.5nm

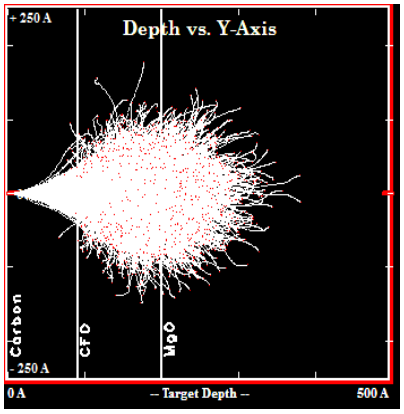

(c) Carbon 9nm

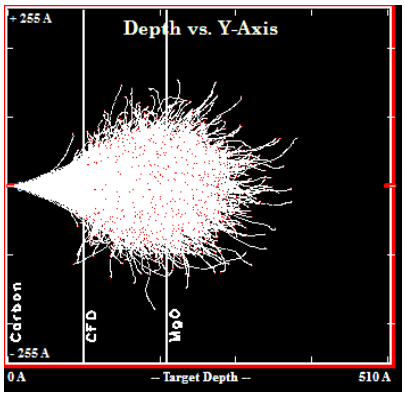

(d) Carbon 10nm

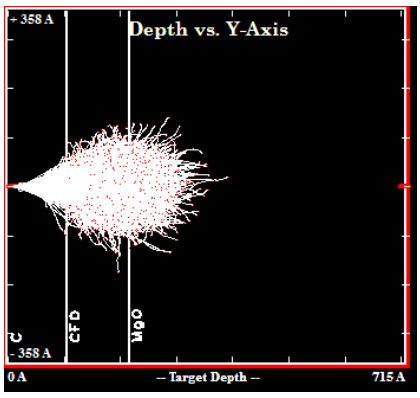

(e) Carbon 10.5nm

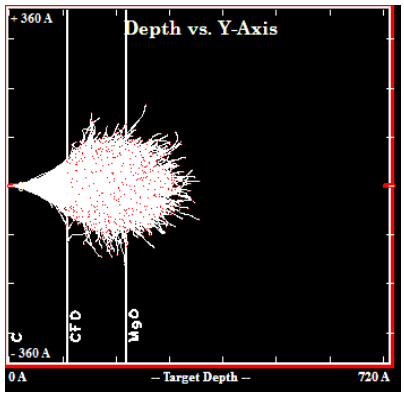

(f) Carbon 11nm

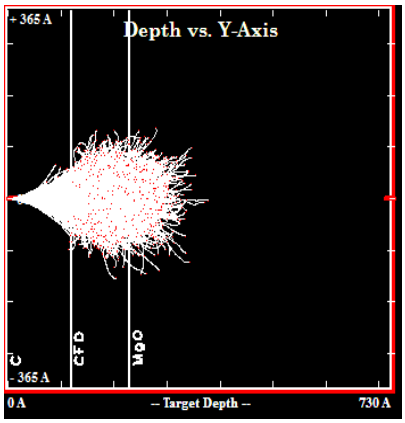

(g) Carbon 12nm

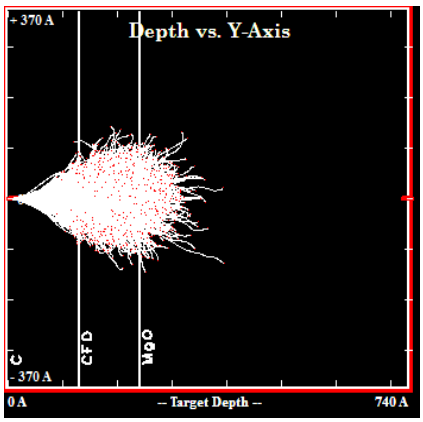

(h) Carbon 13nm

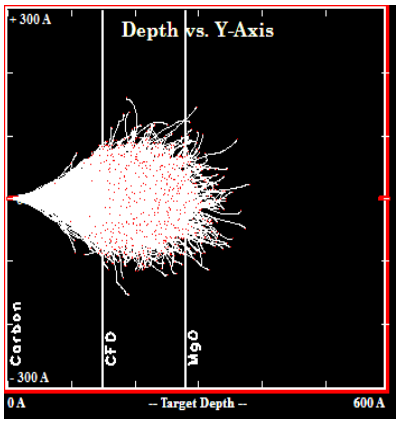

(i) Carbon 15nm

Fig A.3 XY longitudinal

B. Fast Fourier Transform (FFT) of TEM images

We found that the FFT image seems to be spinel-like and also that the SAED pattern contains spinel-like spots (022). On the other hand, the XRD results shown in the chapter 3 can be rationally attributed to the conclusion that the irradiated film is wüstite. We believe the discrepancy comes from the heating effect due to the high energy electron beam.

We carried out the FFT analysis performed by STEM image after ion irradiation and confirmed that the spinel-like pattern appeared in the FFT pattern for the ion-irradiated film, which is shown in the figure B. 1 We agree with that the XRD results and FFT analysis of the TEM images are clearly contradictory. As shown in the figure B. 2, the intensity ratio of (022) to (004) was approximately the same for the two samples meaning that the irradiated film is spinel-like instead of a rocksalt one. This agrees with what the FFT analysis of TEM images pointed out.

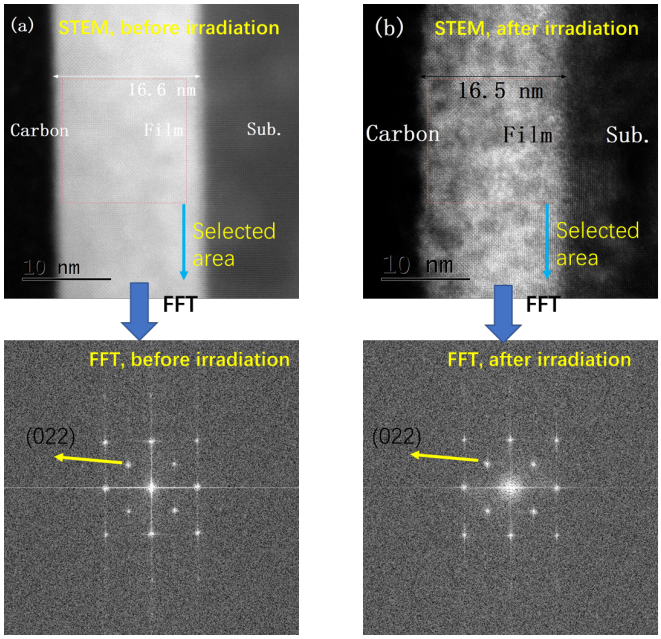

Fig. B.1 FFT analyses of STEM images.

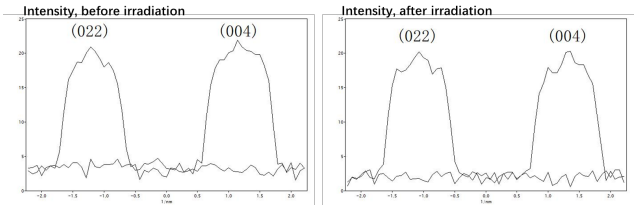

Fig. B.1 Comparison between (022) and (004) intensities after FFT analysis of both as-grown and irradiated films.

However, the SAED images and the intensity ratios shown in the figure B. 3 seem to be different from the above FFT analysis, more or less rocksalt (though very weak 022 reflections can be seen). We note that the SAED was always performed prior to STEM image capturing.

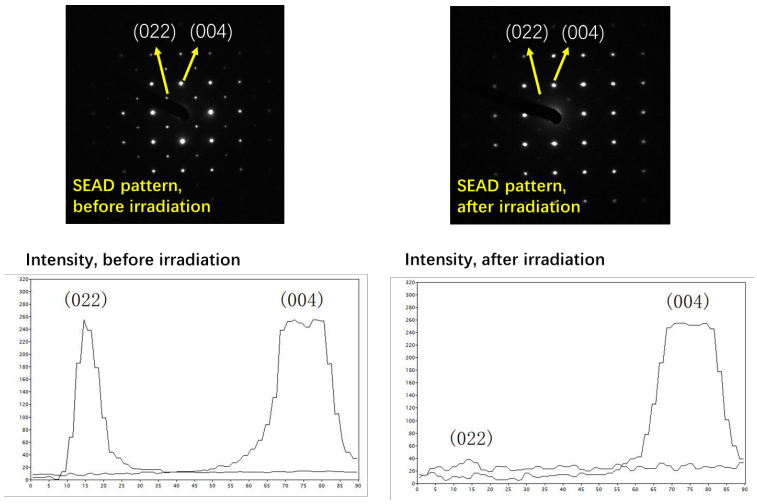

Fig. B.2 SAED images and the intensity ratio of (022) to (004).

The experimental fact that both XRD and SAED indicate a rocksalt structure and the FFT image indicates a spinel structure means the ion-irradiated sample with rocksalt structure had changed back to a spinel structure during STEM image capturing. The spinel structure is an equilibrium state, but the rocksalt structure is metastable. Similar structural transformations by high-energy e-beam during TEM experiments have been reported[77,78,79,80,81] and we believe the same phenomena occurred in our sample and the main conclusion of our manuscript is thus valid. In order to characterize the crystal structure of a “metastable” sample, TEM analysis in conjunction with electron beam diffraction techniques may not be appropriate.

C. EDS measurement

EDS map measurement for Fe_3O_4 thin film of different elements before and after ion irradiation was carried out. The figure of EDS map for each element is given below. Comparing the EDS map of Fe before and after ion irradiation, we found that there is no obvious diffusion of Fe after ion irradiation or significantly shrinking of the range of Fe. That means Fe remained in thin film after ion irradiation, as well as the thickness of ion-irradiated thin film has no change.

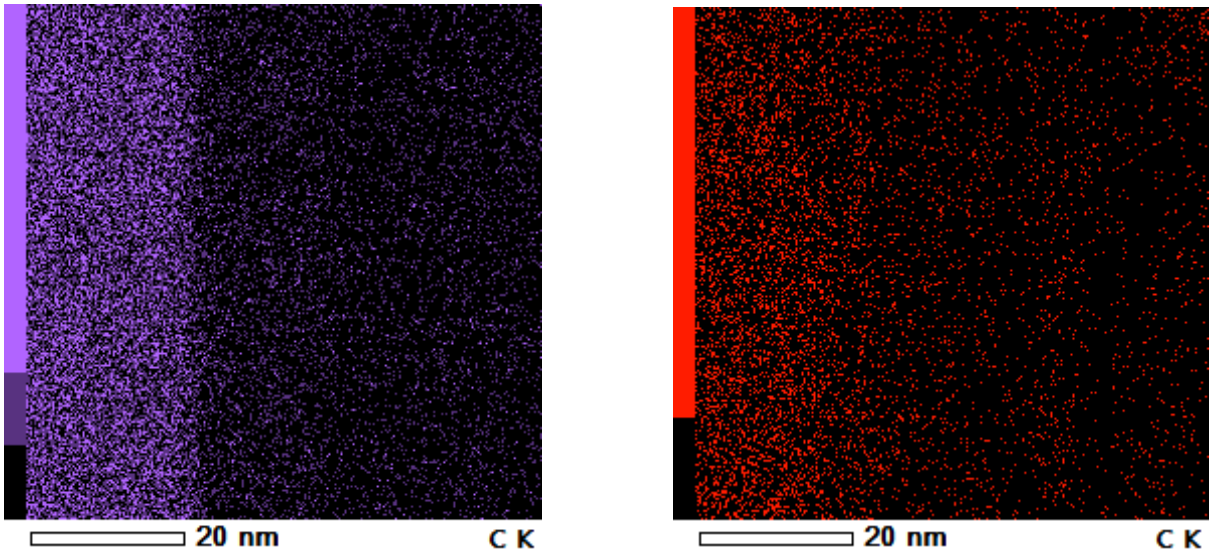

Fig. C.1 EDS map of C before (left) and after (right) ion irradiation.

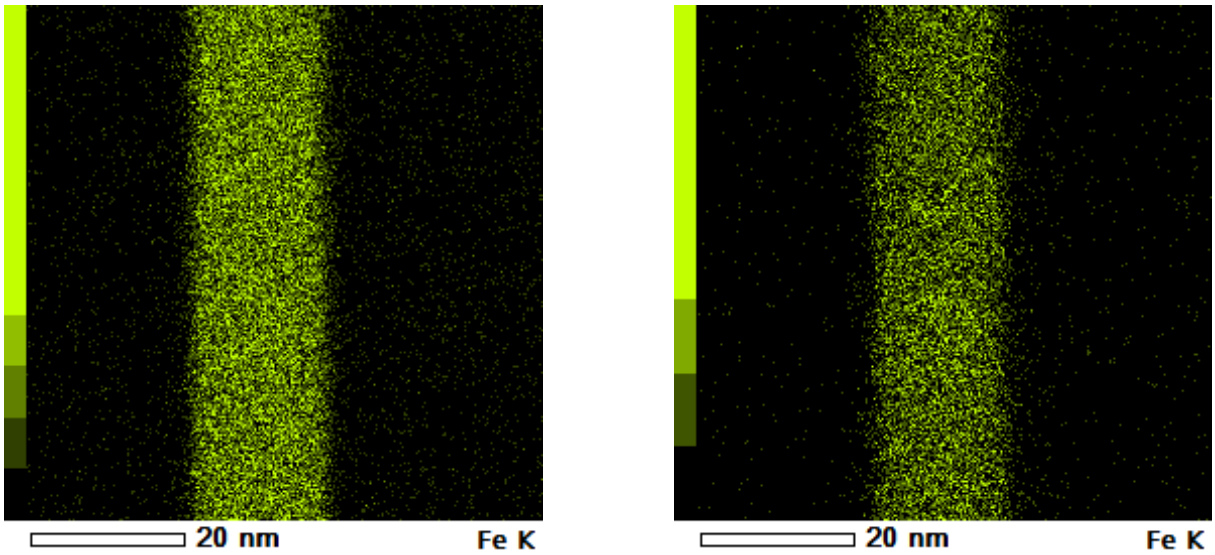

Fig. C.2 EDS map of Fe before (left) and after (right) ion irradiation.

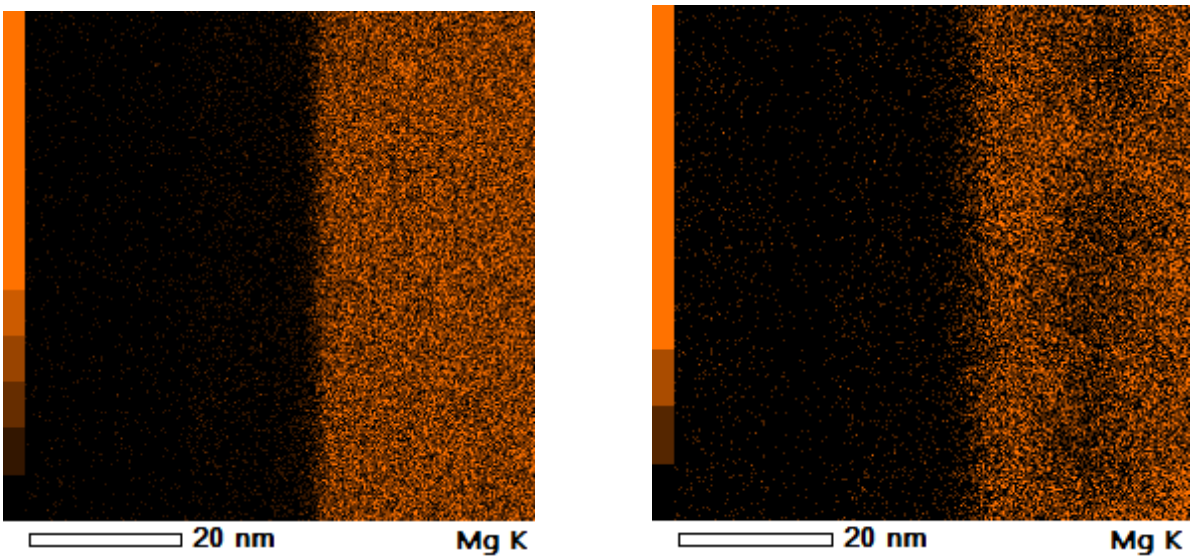

Fig. C.3 EDS map of Mg before (left) and after (right) ion irradiation.

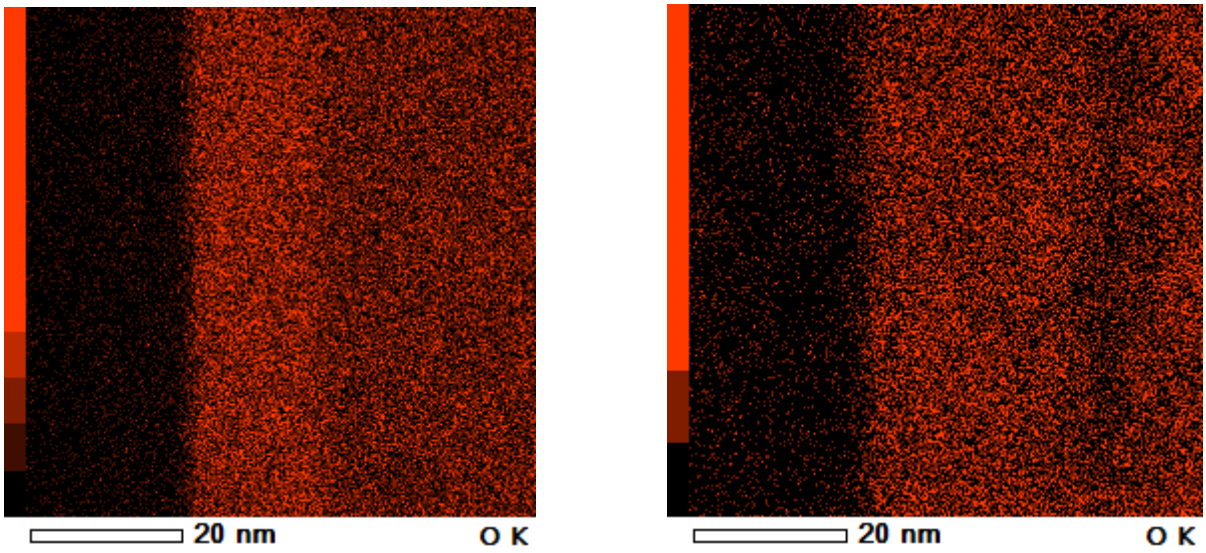

Fig. C.4 EDS map of O before (left) and after (right) ion irradiation.

D. Structure factor calculation

Considering the structure of ion-irradiated thin film, we describe rocksalt-like structure of Wyckoff position of group $Fd\bar{3}m$ as Fe_3O_4. For Fe_3O_4 in one unit cell, 8 cation Fe occupy in $8a$, 16 cation Fe occupy in $16d$ site and 32 onion O occupy in $32e$ site. Fe cations occupy in $8a$ form tetrahedral site with O onion and Fe cation occupy in 16d form octahedral site with O onion. Due to ion irradiation, 24 Fe cations in Fe_3O_4 rearrange in $8a$, $8b$, $16c$ and $16d$, totally 48 sites, randomly. To understand the distribution of Fe cations in ion-irradiated thin film, structure factor $S_{(h\,k\,l)}$ calculation of several diffraction $(h\,k\,l)$ were carried out.

For FCC structure,

$$S_{(h\,k\,l)} = \sum_{atoms} f_{atoms} e^{2\pi i(hx+ky+lz)} \left(1 + \exp\left[2\pi i\left(\frac{1}{2}k + \frac{1}{2}l\right)\right] + \exp\left[2\pi i\left(\frac{1}{2}h + \frac{1}{2}l\right)\right] + \exp\left[2\pi i\left(\frac{1}{2}h + \frac{1}{2}k\right)\right]\right)$$

Considering of 24 Fe cations rearrange in all 48 sites of $8a$, $8b$, $16c$ and $16d$ in ion-irradiated thin film, x_{8a}, x_{8b}, x_{16c}, x_{16d} were used to represent the occupation of Fe ions in $8a$, $8b$, $16c$ and $16d$, respectively. As a result, structure factor is written as the sum of all sites with their own occupation,

$$S_{(h\,k\,l)} = S_{8a(h\,k\,l)} \cdot x_{8a} + S_{8b(h\,k\,l)} \cdot x_{8b} + S_{16c(h\,k\,l)} \cdot x_{16c} + S_{16d(h\,k\,l)} \cdot x_{16d} + S_{O(h\,k\,l)}$$

Here, $S_{O(h\,k\,l)}$ represents the structure factor of O onions.

For $8a$ site, with Wyckoff coordinates $\left(\frac{1}{8}\,\frac{1}{8}\,\frac{1}{8}\right)$, $\left(\frac{7}{8}\,\frac{3}{8}\,\frac{3}{8}\right)$,

$$S_{8a(h\,k\,l)} = \sum_{Fe} f_{Fe} e^{2\pi i(hx+ky+lz)} \left(1 + \exp[\pi i(k+l)] + \exp[\pi i(h+l)] + \exp[\pi i(h+k)]\right)$$

$$= f_{Fe}\left(\exp 2\pi i\left(\frac{1}{8}h + \frac{1}{8}k + \frac{1}{8}l\right) + \exp 2\pi i\left(\frac{7}{8}h + \frac{3}{8}k + \frac{3}{8}l\right)\right)\left(1 + \exp[\pi i(k+l)] + \exp[\pi i(h+l)] + \exp[\pi i(h+k)]\right)$$

Here, f_{Fe} is scattering factor.

The same with $8a$ site,

$$S_{8b(h\,k\,l)} = f_{Fe}\left(\exp 2\pi i\left(\frac{3}{8}h + \frac{3}{8}k + \frac{3}{8}l\right) + \exp 2\pi i\left(\frac{1}{8}h + \frac{5}{8}k + \frac{1}{8}l\right)\right)\left(1 + \exp[\pi i(k+l)] + \exp[\pi i(h+l)] + \exp[\pi i(h+k)]\right)$$

$$S_{16c(h\,k\,l)} = f_{Fe}\left(\exp 2\pi i \times 0 + \exp 2\pi i\left(\frac{3}{4}h + \frac{1}{4}k + \frac{1}{2}l\right) + \exp 2\pi i\left(\frac{1}{4}h + \frac{1}{2}k + \frac{3}{4}l\right) + \exp 2\pi i\left(\frac{1}{2}h + \frac{3}{4}k + \frac{1}{4}l\right)\right)\left(1 + \exp[\pi i(k+l)] + \exp[\pi i(h+l)] + \exp[\pi i(h+k)]\right)$$

$$S_{16d(h\,k\,l)} = f_{Fe}\left(\exp 2\pi i\left(\frac{1}{2}h + \frac{1}{2}k + \frac{1}{2}l\right) + \exp 2\pi i\left(\frac{1}{4}h + \frac{3}{4}k\right) + \exp 2\pi i\left(\frac{3}{4}h + \frac{1}{4}l\right) + \exp 2\pi i\left(\frac{1}{4}k + \frac{3}{4}l\right)\right)\left(1 + \exp[\pi i(k+l)] + \exp[\pi i(h+l)] + \exp[\pi i(h+k)]\right)$$

For reflection $(1\ 1\ 1)$ of spinel structure,

$$S_{8a(1\,1\,1)} = f_{Fe} \cdot (-4\sqrt{2}),\ S_{8b(1\,1\,1)} = f_{Fe} \cdot 4\sqrt{2},$$

$$S_{16c(1\,1\,1)} = f_{Fe} \cdot (-8),\ S_{16d(1\,1\,1)} = f_{Fe} \cdot 8,$$

$$S_{O(1\,1\,1)} = 0,$$

$$S_{(1\,1\,1)} = S_{8a(1\,1\,1)} \cdot x_{8a} + S_{8b(1\,1\,1)} \cdot x_{8b} + S_{16c(1\,1\,1)} \cdot x_{16c} + S_{16d(1\,1\,1)} \cdot x_{16d} + S_{O(1\,1\,1)},$$

$$= f_{Fe} \cdot \left(-4\sqrt{2}\right) \cdot x_{8a} + f_{Fe} \cdot 4\sqrt{2} \cdot x_{8b} + f_{Fe} \cdot (-8) \cdot x_{16\mathrm{c}} + f_{Fe} \cdot 8 \cdot x_{16\mathrm{d}}$$

Combing experiment result of reflection $(1\ 1\ 1)$ of spinel structure after ion irradiation, reflection $(1\ 1\ 1)$ of spinel disappeared. As a result, $S_{(1\,1\,1)}$ should be 0. Due to calculation, the occupation of Fe ions satisfies $x_{8a} = x_{8b}$ and $x_{16c} = x_{16d}$. As well as, when $x_{8a} = x_{8b}$ and $x_{16c} = x_{16d}$, $S(1\ 1\ 3) = 0$, which is also consistent to experiment result of reflection $(1\ 1\ 3)$ of spinel structure. The structure factor calculation of reflection is shown in Table 1. That means in the ion-irradiated thin films, equal Fe ions occupy in $8a$ and $8b$, at the same time, equal Fe ions occupy in $16c$ and $16d$. Fe occupy in $8a$ and $8b$ or not must be considered.

When $x_{8a} = x_{8b} = 0,\ x_{16c} = x_{16d}$,

Fe cations in $8a$ site of spinel structure move to $16c$ or $16d$ site totally, and Fe cation occupy in $16c$ and $16d$ equally, which formed rocksalt structure with cation site vacancy. This situation consists with B.P. Uberuga's result[42].

When $x_{8a} = x_{8b} \neq 0,\ x_{16c} = x_{16d}$,

Fe cations in $8a$ site of spinel structure move to $16c$ or $16d$ site partly, the others move to $8b$ site. Fe cations in $8a$ site is equal to $8b$ site, as well as $16c$ and $16d$ site, which formed rocksalt-like structure.

For understanding the coordination condition of Fe cations in tetrahedral site ($8a$ and $8b$) and octahedral site ($16c$ and $16d$) site, reflection of $(0\ 2\ 2)$ of Fe_3O_4 of the spinel structure also has been carried out after ion irradiation, which is shown in Fig. 3(c). After ion irradiation, the disappearing of reflection of $(0\ 2\ 2)$ of Fe_3O_4 were observed. In Table 1, the calculation of structure factor of reflection of $(0\ 2\ 2)$ of Fe_3O_4, $S(0\ 2\ 2)$ is revealed. According to calculation result, $S(0\ 2\ 2)$ is only contingent on whether Fe cations occupy in $8a$ and $8b$ site and has no relations with whether Fe cations occupy in $16c$ and $16d$ site. If Fe cations occupy in tetrahedral site ($8a$ and $8b$), $S(0\ 2\ 2) \neq 0$, which means reflection of $(0\ 2\ 2)$ of Fe_3O_4 should be observed in ion-irradiated thin film. On the contrary, if Fe cations don't occupy in tetrahedral site ($16c$ and $16d$), $S(0\ 2\ 2) = 0$, which means reflection of $(0\ 2\ 2)$ of Fe_3O_4 should not be observed in ion-irradiated thin film. Combining to the experiment result of reflection of $(0\ 2\ 2)$ of Fe_3O_4 after ion irradiation, which reflection of $(0\ 2\ 2)$ of Fe_3O_4 disappeared in ion-irradiated thin film. Fe cations don't occupy in tetrahedral site ($8a$ and $8b$) is confirmed.

Considering of higher symmetry space group $Pn\bar{3}m$, tetrahedral site

For $Pn\bar{3}m$

$$S'_{(h\,k\,l)} = \sum_{atoms} f_{atoms} e^{2\pi i(hx+ky+lz)} \left(1 + \exp\left[2\pi i\left(\frac{1}{2}k + \frac{1}{2}l\right)\right] + \exp\left[2\pi i\left(\frac{1}{2}h + \frac{1}{2}l\right)\right] + \exp\left[2\pi i\left(\frac{1}{2}h + \frac{1}{2}k\right)\right]\right)$$

For $2a$ site, Wyckoff position $\left(\frac{1}{4}\ \frac{1}{4}\ \frac{1}{4}\right)$, $\left(\frac{3}{4}\ \frac{3}{4}\ \frac{3}{4}\right)$

$$S'_{2a(h\,k\,l)} = \sum_{Fe} f_{Fe} e^{2\pi i(hx+ky+lz)} \left(1 + \exp[\pi i(k+l)] + \exp[\pi i(h+l)] + \exp[\pi i(h+k)]\right)$$

$$= f_{Fe}\left(\exp 2\pi i\left(\frac{1}{4}h + \frac{1}{4}k + \frac{1}{4}l\right) + \exp 2\pi i\left(\frac{3}{4}h + \frac{3}{4}k + \frac{3}{4}l\right)\right)(1 + \exp[\pi i(k+l)] + \exp[\pi i(h+l)] + \exp[\pi i(h+k)])$$

For $4b$ site, Wyckoff position $(0\ 0\ 0)$, $\left(\frac{1}{2}\ \frac{1}{2}\ 0\right)$, $\left(\frac{1}{2}\ 0\ \frac{1}{2}\right)$, $\left(0\ \frac{1}{2}\ \frac{1}{2}\right)$

$$S'_{4b(h\,k\,l)} = \sum_{Fe} f_{Fe} e^{2\pi i(hx+ky+lz)} \left(1 + \exp[\pi i(k+l)] + \exp[\pi i(h+l)] + \exp[\pi i(h+k)]\right)$$

$$= f_{Fe}\left(\exp 2\pi i \cdot 0 + \exp 2\pi i\left(\frac{1}{2}h + \frac{1}{2}k\right) + \exp 2\pi i\left(\frac{1}{2}h + \frac{1}{2}l\right) + \exp 2\pi i\left(\frac{1}{2}k + \frac{1}{2}l\right)\right)(1 + \exp[\pi i(k+l)] + \exp[\pi i(h+l)] + \exp[\pi i(h+k)])$$

For $4c$ site, Wyckoff position $\left(\frac{1}{2}\ \frac{1}{2}\ \frac{1}{2}\right)$, $\left(0\ 0\ \frac{1}{2}\right)$, $\left(0\ \frac{1}{2}\ 0\right)$, $\left(\frac{1}{2}\ 0\ 0\right)$

$$S'_{4c(h\,k\,l)} = \sum_{O} f_{O} e^{2\pi i(hx+ky+lz)} \left(1 + \exp[\pi i(k+l)] + \exp[\pi i(h+l)] + \exp[\pi i(h+k)]\right)$$

$$= f_{O}\left(\exp 2\pi i\left(\frac{1}{2}h + \frac{1}{2}k + \frac{1}{2}l\right) + \exp 2\pi i \cdot \frac{1}{2}l + \exp 2\pi i \cdot \frac{1}{2}k + \exp 2\pi i \cdot \frac{1}{2}h\right)(1 + \exp[\pi i(k+l)] + \exp[\pi i(h+l)] + \exp[\pi i(h+k)])$$

For reflection, $(0\ 1\ 1)_{RC}$

$$S'_{2a(0\ 1\ 1)_{RC}} = f_{Fe}\left(\exp 2\pi i \cdot \frac{1}{2} + \exp 2\pi i\right)(1 + \exp 2\pi i + \exp \pi i + \exp \pi i) = 0$$

$$S'_{4b(0\ 1\ 1)_{RC}} = f_{Fe}\left(\exp 2\pi i \cdot 0 + \exp 2\pi i \cdot \frac{1}{2} + \exp 2\pi i \cdot \frac{1}{2} + \exp 2\pi i \cdot 1\right)(1 + \exp 2\pi i + \exp \pi i + \exp \pi i) = 0$$

$$S'_{4c(0\ 1\ 1)_{RC}} = f_{O}\left(\exp 2\pi i \cdot 1 + \exp 2\pi i \cdot \frac{1}{2} + \exp 2\pi i \cdot \frac{1}{2} + \exp 2\pi i \cdot 0\right)(1 + \exp 2\pi i + \exp \pi i + \exp \pi i) = 0$$

$$S'_{(0\ 1\ 1)_{RC}} = S'_{2a(0\ 1\ 1)_{RC}} + S'_{4b(0\ 1\ 1)_{RC}} + S'_{4c(0\ 1\ 1)_{RC}} = 0$$

As a result, reflection $(0\ 1\ 1)_{RC}$ of $Pn\bar{3}m$ should not be observed.

Reference

[1] D. Sellmyer and R. Nebraska, *Advanced Magnetic Nanostructures*, Spring, New York, (2006).

[2] S. H. Charap *et al*., *Thermal Stability of Recorded Information at High Density*, IEEE Trans. Magn., 33,978 (1997).

[3] D. J. Sellmyer, M. Zheng, and R. Skomski, *Magnetism of Fe, Co and Ni nanowires in self-assembled arrays*, J. Phys.: Condens. Matter, **13**,433 (2001).

[4] D. J. Sellmyer, M. Yu, R. A. Thomas, Y. Liu, and R. D. Kirby, *Nanoscale design of films for extremely high density magnetic recording*, Phys. Low-Dim. Struct. 1-2, 155 (1998).

[5] K. Naito, H. Hieda, M. Sakurai, Y. Kamata, and K. Asakawa, *2.5-inch disk patterned media prepared by an artificially assisted self-assembling method*, IEEE. Trans. Magn. 38 (5), 1949 (2002).

[6] Y. Kubota, L. Folks, and E. E. Marinero, *Intergrain magnetic coupling and microstructure in CoPtCr, CoPtCrTa, and CoPtCrB alloys*, J. Appl. Phys., **84**, 6202 (1998).

[7] S. Saito, N. Itagaki, F. Hoshi, and M. Takahashi, *Improvement of magnetocrystalline anisotropy of columnar structure for epitaxially grown CoCr-based perpendicular media*, J. Appl. Phys. **93**, 8182, (2003).

[8] R. F. C. Farrow, D. Weller, R. F. Marks, M. F. Toney, S. Hom, G. R. Harp and A. Cebollada., *Growth temperature dependence of long-range alloy order and magnetic properties of epitaxial Fe_xPt_{1-x} (x~0.5) films*. Appl. Phys. Lett., vol. 69, pages 1166-1168, (1996).

[9] Y. Kota and A. Sakuma, *Magnetocrystalline anisotropy in FePt with $L1_0$ ordering and tetragonal distortion*, J. Appl. Phys., **111**, 07A310 (2012).

[10] K.R. Coffey, M.A. Parker and J.K. Howard, *High anisotropy $L1_0$ thin films for longitudinal recording*, IEEE Trans. Magn., **31**, 2737 (1995).

[11] T. Suzuki, N. Honda and K. Ouchi, *Preparation and Magnetic Properties of Sputter-Deposited Fe-Pt Thin Films with Perpendicular Anisotropy*, J. Magn. Soci. Jpn., **21**, 177 (1997).

[12] 太田恵造, 磁気工学の基礎I, 共立出版 (1973).

[13] T. Niizeki *et al.*, *Extraordinarily large perpendicular magnetic anisotropy in epitaxially strained cobalt-ferrite $Co_xFe_{3-x}O_4$ (001) (x = 0.75, 1.0) thin films*, *Appl. Phys. Lett.*, **103**, 162407, pp. 1–5, (2013).

[14] B. Terris, *Fabrication challenges for patterned recording media*, J. Magn. Magn. Mater. **321**, 512–517 (2009).

[15] A. Kikitsu, T. Maeda, H. Hieda, R. Yamamoto, N. Kihara, and Y. Kamata, *5 Tdots/in^2 bit patterned media fabricated by a directed self-assembly mask*, J. Magn. Magn. Mater. **321**, 526–530 (2009).

[16] Y. Inaba, *New high density recording technology: energy assisted recording media*, Mater. Sci. (2010).

[17] H. Saga, H. Nemoto, H. Sukeda, and M. Takahashi, *New Recording Method Combining Thermo-Magnetic Writing and Flux Detection*, Jpn. J. Appl. Phys., **38**, 1839 (1999).

[18] T. Matsumoto, K. Nakamura, T. Nishida, H. Hieda, A. Kikitsu, K. Naito and T. Koda, *Thermally assisted magnetic recording on a bit-patterned medium by using a near-field optical head with a beaked metallic plate*, Appl. Phys. Lett. **93**, 031108 (2008).

[19] M. H. Kryder, E. C. Gage, T. W. McDaniel, W. A. Challener, R. E. Rottmaye, G. P. Ju, Y. Hsia and M. F. Erden, *Heat Assisted Magentic Recording*, Proc. IEEE., **96**, 1810 (2008).

[20] HITACHI, DISKCON JAPAN 2010 report, (2010).

[21] Z. Gao, AVS North America Plasma Application, **4** (2013).

[22] J. C. Mallinson, *A new theory of recording media noise*, IEEE Trans. Magn., **27**, 3519 (1991).

[23] D. Weller and A. Moser, *Thermal effect limits in ultrahigh-density magnetic recording*. IEEE Trans. Mag., vol. 35, pages 4423-4439, (1999).

[24] K. Sato, A. Ajan, N. Aoyama, T. Tanaka, Y. Miyaguchi, K. Tsumagari, T. Morita, T. Nishihashi, A. Tanaka and T. Uzumaki, *Magnetization suppression in Co/Pd and CoCrPt by nitrogen ion implantation for bit patterned media fabrication*, J. Appl. Phys. **107**, 123910 (2010).

[25] T. Kato, S. Iwata, Y. Yamauchi and S.Tsunashima, *Planar patterned media fabricated by ion irradiation into CrPt3 ordered alloy films*, J. Appl. Phys. **105**, 07C117 (2009).

[26] D. Oshima, T. Kato, S. Iwata and S. Tsunashima, *Control of Magnetic Properties of MnGa films by Kr^+ Ion Irradiation for Application to Bit Patterned Media*, IEEE TransMAG, **49**, 3608 (2013).

[27] 鎌田芳幸, 東芝レビュー, Vol. 65 No.10 (2010).

[28] C. T. Rettner, S. Anders, J. E. E. Baglin, T. Thomson and B. D. Terris, *Characterization of the magnetic modification of Co/Pt multilayer films by He^+, Ar^+ and Ga^+ ion irradiation*, Appl. Phys. Lett. **80**, 2 (2002).

[29] D. Ranelosona, *Bending instability of electrically charged liquid jets of polymer solutions in electrospinning*, J. Appl. Phys. **87**. 4531 (2000).

[30] G. L. Causer, H. L. Zhu, J. Davis, M.Ionescu, G. J. Mankey, L. Wang and F. Klose, *The microstructural evolution of chemical disorder and ferromagnetism in He^+ irradiated $FePt_3$ films*, Appl. Surf. Sci. **459**, 30 (2018).

[31] G. S. Was, *Fundamentals of Radiation Materials Science, Metals and Alloys*, Spriner, (2007).

[32] J. Fassbendera, J. Grenzer, O. Roshchupkina, Y. Choi, J. S. Jiang and D.Bader, *The effect of ion irradiation and annealing on exchange spring magnets*, J. Appl. Phys. **105**, 023902 (2009).

[33] J. Sun, Z. Wang, Y. Wang, Y. Zhu, L. Pang, T. Shen and F. Li, S*tructural and magnetic properties studies on swift heavy ion (SHI) irradiated Fe_3O_4 thin films*, Nucl. Instrum. Methods. Phys. Res. B **286**, 277 (2012).

[34] C. Wang, H. Zhang, K. Deepak, C. Chen, A. Fouchet, J. Duan, D. Hilliard, U. Kentsch, D. Chen, M. Zeng, X. Gao, Y. Zeng, Y. Zeng, M. Helm, W. Prellier and S. Zhou, *Tuning the metal-insulator transition in*

epitaxial $SrVO_3$ films by uniaxial strain, Phys. Phys. Rev. Mater. **3**, 115001 (2019).

[35] C. Wang, C. Chang, A. Herklotz, C. Chen, F. Ganss, U. Kentsh, D. Chen, X. Gao, Y. Zeng, O. Hellwig, M. Helm, S. Gemming, Y. Chu and S. Zhou, *Topological Hall Effect in Single Thick SrRuO3 Layers Induced by Defect Engineering*, Adv. Electron. Mater. **6**, 2000184 (2020).

[36] E. Ferreiro-Vila, D. Bugallo, C. Magén, F. Rivadulla and J. Teresa, *Topotactic transformation in $SrFeO_{3-\delta}$ triggered by low-dose Ga^+ focused ion irradiation*, Appl. Phys. Lett. **116**, 163103 (2020).

[37] S. J. Zinkle and G. S. Was, *Materials challenges in nuclear energy*, *Acta Matter.* **61,** 735-758 (2013).

[38] J. Fassbendera and J. McCord, *Magnetic patterning by means of ion irradiation and implantation*, J. Magn. Magn. Mater. **320**, 579 (2008).

[39] D. McGrouther and J. N. Chapman, *Nanopatterning of a thin ferromagnetic CoFe film by focused-ion-beam irradiation*, Appl. Phys. Lett. **87**, 022507 (2005).

[40] V. Parekh, D. Smith, Chunsheng E, J. Rantschler, S. Khizroev and D. Litvinov, *He^+ ion irradiation study of continuous and patterned multilayers*, J. Appl. Phys. **101**, 083904 (2007).

[41] D. Oshima, M. Tanimoto, T. Kato, Y. Fujiwara, T. Nakamura, Y. Kotani, S. Tsunashima and S. Iwata, *Modifications of Structure and Magnetic Properties of $L1_0$ MnAl and MnGa Films by Kr^+ Ion Irradiation*, IEEE. Trans. Magn. **50**, 12 (2014).

[42] B.P. Uberuga, M. Tang, C. Jiang, J. A. Valdez, R. Smith, Y.Q. Wang and K. Sickafus, *Opposite correlations between cation disordering and amorphization resistance in spinels versus pyrochlores*, Nat. Commun. **6**, 8750 (2015).

[43] N. Martin, J. McCord, A. Gerber, T. Strache, T. Gemming, I. Monch, N. Farag, R. Schafer, J. Fassbender, E. Quandt, and L. Schultz, *Local stress engineering of magnetic anisotropy in soft magnetic thin films*, Appl. Phys. Lett. **94**, 062506 (2009).

[44] J. Fassbendera and J. McCord, *Control of saturation magnetization, anisotropy, and damping due to Ni implantation in thin $Ni_{89}Fe_{19}$ layers*, Appl. Phys. Lett. **88**, 252501 (2006).

[45] J. Suk, I. Jeon, T. Kim, J. Song and J. Lee, *Study of the magnetoresistance of magnetic film modified by using ion beams*, J. Appl. Phys. **109**, 07C730 (2011).

[46] J. McCord, T. Gemming, L. Schultz, J. Fassbender, M. Liedke, M. Frommberger, and E. Quandt, *Magnetic anisotropy and domain patterning of amorphous films by He-ion irradiation*, Appl. Phys. Lett. **86**, 162502 (2005).

[47] E. Kita, Z. K. Suzuki, Y. Liu, Y. Utsumi, J. Morishita, D. Oshima, T. Kato, T. Niizeki, K. Mibu and H. Yanagihara, *Magnetization control for bit pattern formation of spinel ferromagnetic oxides by Kr ion implantation*, J. Appl. Phys. **115**, 17B907 (2014).

[48] T. Hinoue, K. Ito, Y. Hirayama and Y. Hosoe, *Magnetic properties and recording performances of patterned media fabricated by nitrogen ion implantation*, J. Appl. Phys. **109**, 07B907 (2011).

[49] S. Kim, S. Lee, J. Ko, J. Son, M. Kim, S. Kan and J. Hong, *Nanoscale patterning of complex magnetic*

nanostructures by reduction with low-energy protons, Nat. Nanotechnol. **7**, 567 (2012).

[50] E. Kita, Z. K. Ono, N. Yamaguchi, T. Nishihashi, M. Iura, J. Morishita, Y. Utsumi, K. Mibu, T. Niizeki, K. Z. Niizeki and H. Yanagihara, *Control of magnetization in spinel-type Fe_3O_4 thin films by N_2 ion implantation*, J. Appl. Phys. **115**, 17B907 (2014).

[51] T. B. Massalski, H. Okamoto, P. R. Subramanian and L. Kacprzak, *BINARY. ALLOY PHASE DIAGRAMS* (ASM international, USA, 1990), vol. 2, pp. 1825.

[52] 近角聡信 *et al.,* 磁性体ハンドブック 朝倉書店 (1975).

[53] 太田恵造, 磁気工学の基礎II 共立出版 (1973).

[54] S. A. Chambers, R.F.C. Farrow, S. Maat, M. F. Toney, L. Folks, J. G. Catalano, T. P. Trainor and G. E. Brown Jr., *Molecular beam epitaxial growth and properties of $CoFe_2O_4$ on MgO(0 0* 1), J. Magn. Magn. Mater. **246**, 124 (2002).

[55] A. V. Ramos, M. J. Guittet and J. B. Moussy, *Influence of a metallic or oxide top layer in epitaxial magnetic bilayers containing CoFe2O4(111) tunnel barriers*, Phys. Rev. B **75**, 224421 (2007).

[56] A. V. Ramos, M. J. Guittet, J. B. Moussy, M. G. Soyer, C. Gatel, P. B. Guillemaud, B. W. Fonrose and E. Snoeck, *Room temperature spin filtering in epitaxial cobalt-ferrite tunnel barriers*, Appl. Phys. Lett. **91**, 122107 (2007).

[57] M. Ning, J. Li, C. K. Ong and S. J. Wang, *High perpendicular coercive field of (100) – oriented $CoFe_2O_4$ thin films on Si (100) with MgO buffer layer*, J. Appl. Phys. **103**, 013911 (2008).

[58] A. K. Axelsson, M. Valant, L. Fenner, A. S. Wills and N. M. Alford, *Chemistry of post-annealing of epitaxial $CoFe_2O_4$ thin films Science Direct*, Thin Solid Films. **517**, 3742 (2009).

[59] 金原粲, スパッタリング現象, 東京大学出版会, (1984).

[60] Bao-he Li *et al.,* 高磁晶各向异性磁记录薄膜材料 冶金工业出版社 (2012).

[61] M. Ohring, *The materials science of thin films. Boston: Academic Press* (1992).

[62] D. L. Smith, *Thin film deposition*, New York: McGraw-Hill Inc. (1995).

[63] H. Yanagihara, M. Myoka, D. Isaka, T. Niizeki, K. Mibu and E. Kita, *Selective growth of Fe_3O_4 and γ-Fe_2O_3 films with reactive magnetron sputtering*, J. Phys. D: Appl. Phys. **46**, 175004 (2013).

[64] M. Naito, T. Yamshita, M. Tanjyo, M. Konishi, Y. Okute and N. Hamamoto, Journal of NISSIN ELECTRIC, **62**, 1 (2017).

[65] E.N. Kaufmann, *Characterization of Materials*, John Wiley & Sons, Inc. (2012).

[66] A, Ichimiya, and P. I. Cohen, *Reflection high-energy electron diffraction*, Cambridge University Press. Cambridge, UK. (2004).

[67] S. Thomas, R. Thomas, A. K. Zachariah and R. K. Mishra, *Thermal and Rheological Measurement Technique for Nanomaterials Characterization*, Elsevier Inc. (2017).

[68] N.N. Greenwood, T.C.Gibb, *Mössbauer Spectroscopy*, Chapman and Hall Ltd. London (1971).

[69] F. Salvat, J. Parellada, *Theory of conversion electron Mössbauer spectroscopy (CEMS)*, Nuclear Instruments and Methods in Physics Research Section B, **1**, 70-84, (1984).

[70] F. Ziegler, J. P. Biersack and M. D. Ziegler, *SRIM - The Stopping and Range of Ions in Matter*, Nucl. Instrum. Methods. Phys. Res. Sect. B: **268**, 11 (2010).

[71] B. J. Evans and S.S. Hafner, *^{57}Fe Hyperfine Fields in Magnetite (Fe_3O_4)*, J.Appl.Phys. **40**, 1411 (1969).

[72] J.H. Condon and R.E. Walstedt, *Direct Evidence for Magnetic Domains in Silver*, J. Appl. Phys. **40**, 3 (1969).

[73] N.Spiridis, B.Handke, T.Ślęzak, J.Barbasz, M.Zając, J.Haber and J.Korecki, *Surface Structure of Epitaxial Magnetite Fe_3O_4(001) Films - In situ STM and CEMS Studies*, J. Phys. Chem. B, **108**, 14356-14361 (2004).

[74] S. Nakamura, L. Li, M. Tanaka, S. Todo, and K. Siratori, *Crystal-Site-Selective Spectrum of Fe_3O_4 Obtained by Mössbauer Diffraction*, J. Phys. Soc. Jpn. **66**, 472–477 (1997).

[75] T. B. Massalski, H. Okamoto, P. R. Subramanian and L. Kacprzak, *BINARY. ALLOY PHASE DIAGRAMS* (ASM international, USA, 1990), vol. 2, pp. 1740.

[76] X. L. Qu and Q. S. Deng, *Damage and recovery induced by a high energy e-beam in a silicon nanofilm*, RCS. Adv., **7**, 37032 (2017).

[77] D. D. Thornburg and C. M. Wayman, Phys. Stat. Soli. (a) **15**. 449 (1973).

[78] L. Reimer and H. Kohl, *Transmission Electron Microscopy - Physics of Image Formation*, 5th Edition, (Springer, New York, 2008), vol. 11, pp. 459.

[79] F. Niekiel, S. M. Kraschewski, J. Muller, B. Burt and E. Spiecker, *Local temperature measurement in TEM by parallel beam electron diffraction*, Ultramicroscopy, **176**, 161 (2017).

[80] W. F. Wei, W. X. Chen and D. G. Ivey, *Rock Salt−Spinel Structural Transformation in Anodically Electrodeposited Mn−Co−O Nanocrystals*, Chem. Mater. **20**, 5 (2008).

[81] P.Parajuli, B. J. Kwon, B. Key, J. Cabana, B. Ingram and R. Kile, *Electron-beam-induced Spinel to Defect Rocksalt Phase Transition in $MgCrMnO_4$*, Microscopy and Microanalysis, **26**, 788 (2020).